














































Transit Timing Variations for AU Microscopii b & c

JUSTIN M. WITTRÖCK ¹ STEFAN DREIZLER ² MICHAEL A. REEFE ¹ BRETT M. MORRIS ³
PETER P. PLAVCHAN ¹ PATRICK J. LOWRANCE ⁴ BRICE-OLIVIER DEMORY ³
JAMES G. INGALLS ⁴ EMILY A. GILBERT ^{5, 6, 7, 8, 9} THOMAS BARCLAY ^{6, 8} BRYSON L. CALE ¹
KAREN A. COLLINS ¹⁰ KEVIN I. COLLINS ¹ IAN J. M. CROSSFIELD ¹¹ DIANA DRAGOMIR ¹²
JASON D. EASTMAN ¹⁰ MOHAMMED EL MUFTI ¹ DAX FELIZ ¹³ JONATHAN GAGNÉ ^{14, 15}
ERIC GAIDOS ¹⁶ PETER GAO ¹⁷ CLAIRE S. GENESER ¹⁸ LESLIE HEBB ¹⁹
CHRISTOPHER E. HENZE ²⁰ KEITH D. HORNE ²¹ JON M. JENKINS ²⁰ ERIC L. N. JENSEN ²²
STEPHEN R. KANE ²³ LAUREL KAYE ²⁴ EDER MARTIOLI ^{25, 26} TERESA A. MONSIE ⁸
ENRIC PALLÉ ^{27, 28} ELISA V. QUINTANA ⁸ DON J. RADFORD ²⁹
VERONICA ROCCATAGLIATA ^{30, 31, 32} JOSHUA E. SCHLIEDER ⁸ RICHARD P. SCHWARZ ³³
AVI SHPORER ³⁴ KEIVAN G. STASSUN ¹³ CHRISTOPHER STOCKDALE ³⁵
THIAM-GUAN TAN ^{36, 37} ANGELLE M. TANNER ¹⁸ ANDREW VANDERBURG ³⁴
LAURA D. VEGA ^{38, 8, 39} AND SONGHU WANG ⁴⁰

¹*Department of Physics & Astronomy, George Mason University, 4400 University Drive MS 3F3, Fairfax, VA 22030, USA*

²*Institut für Astrophysik, Georg-August-Universität, Friedrich-Hund-Platz 1, 37077 Göttingen, Germany*

³*Center for Space and Habitability, University of Bern, Gesellschaftsstrasse 6, 3012 Bern, Switzerland*

⁴*IPAC-Spitzer, California Institute of Technology, MC 314-6, 1200 E. California Blvd., Pasadena, California 91125, USA*

⁵*Department of Astronomy & Astrophysics, University of Chicago, 5640 S. Ellis Ave, Chicago, IL 60637, USA*

⁶*University of Maryland, Baltimore County, 1000 Hilltop Circle, Baltimore, MD 21250, USA*

⁷*The Adler Planetarium, 1300 South Lakeshore Drive, Chicago, IL 60605, USA*

⁸*NASA Goddard Space Flight Center, 8800 Greenbelt Road, Greenbelt, MD 20771, USA*

⁹*GSFC Sellers Exoplanet Environments Collaboration*

¹⁰*Center for Astrophysics | Harvard & Smithsonian, 60 Garden Street, Cambridge, MA 02138, USA*

¹¹*Department of Physics & Astronomy, University of Kansas, 1251 Wescoe Hall Dr, Lawrence, KS 66045, USA*

¹²*Department of Physics & Astronomy, University of New Mexico, Albuquerque, NM, USA*

¹³*Department of Physics & Astronomy, Vanderbilt University, 6301 Stevenson Center Ln., Nashville, TN 37235, USA*

¹⁴*Planétarium Rio Tinto Alcan, Espace pour la vie, 4801 av. Pierre-De Coubertin, Montréal, QC H1V 3V4, Canada*

¹⁵*Institute for Research on Exoplanets, Université de Montréal, Département de Physique, C.P. 6128 Succ. Centre-ville, Montréal, QC H3C 3J7, Canada*

¹⁶*University of Hawai'i at Mānoa, 1680 East-West Road, Honolulu, HI 96822, USA*

¹⁷*Earth and Planets Laboratory, Carnegie Institution for Science, 5241 Broad Branch Rd NW, Washington, DC 20015, USA*

¹⁸*Mississippi State University, 75 B. S. Hood Road, Mississippi State, MS 39762, USA*

¹⁹*Physics Department, Hobart and William Smith Colleges, Geneva, NY 14456, USA*

²⁰*NASA Ames Research Center, MS 244-30, Moffett Field, CA 94035, USA*

²¹*SUPA Physics and Astronomy, University of St. Andrews, Fife, KY16 9SS Scotland, UK*

²²*Department of Physics & Astronomy, Swarthmore College, Swarthmore PA 19081, USA*

²³*University of California, Riverside, 900 University Ave., Riverside, CA 92521, USA*

- ²⁴*Sub-department of Astrophysics, Department of Physics, University of Oxford, Denys Wilkinson Building, Keble Road, Oxford, OX1 3RH, UK*
- ²⁵*Sorbonne Université, CNRS, UMR 7095, Institut d’Astrophysique de Paris, 98 bis bd Arago, 75014 Paris, France*
- ²⁶*Laboratório Nacional de Astrofísica, Rua Estados Unidos 154, Itajubá, MG 37504-364, Brazil*
- ²⁷*Instituto de Astrofísica de Canarias, Vía Láctea s/n, E-38205 La Laguna, Tenerife, Spain*
- ²⁸*Departamento de Astrofísica, Universidad de La Laguna, E-38206 La Laguna, Tenerife, Spain*
- ²⁹*Brierfield Observatory, Bowral, New South Wales, Australia*
- ³⁰*Dipartimento di Fisica “Enrico Fermi”, Università di Pisa, Largo Pontecorvo 3, 56127 Pisa, Italy*
- ³¹*INFN, Sezione di Pisa, Largo Bruno Pontecorvo 3, 56127 Pisa, Italy*
- ³²*INAF-Osservatorio Astrofisico di Arcetri, Largo E. Fermi 5, 50125 Firenze, Italy*
- ³³*Patashnick Voorheesville Observatory, Voorheesville, NY 12186, USA*
- ³⁴*Department of Physics and Kavli Institute for Astrophysics and Space Research, Massachusetts Institute of Technology, Cambridge, MA 02139, USA*
- ³⁵*Hazelwood Observatory, Hazelwood South, Victoria, Australia*
- ³⁶*Perth Exoplanet Survey Telescope, Perth, Western Australia, Australia*
- ³⁷*Curtin Institute of Radio Astronomy, Curtin University, Bentley, Western Australia 6102*
- ³⁸*Department of Astronomy, University of Maryland, College Park, MD 20742, USA*
- ³⁹*Center for Research and Exploration in Space Science & Technology, NASA/GSFC, Greenbelt, MD 20771, USA*
- ⁴⁰*Department of Astronomy, Indiana University, Bloomington, IN 47405, USA*

ABSTRACT

We explore the transit timing variations (TTVs) of the young (22 Myr) nearby AU Mic planetary system. For AU Mic b, we introduce three *Spitzer* (4.5 μm) transits, five *TESS* transits, 11 *LCO* transits, one *PEST* transit, one *Brierfield* transit, and two transit timing measurements from Rossiter-McLaughlin observations; for AU Mic c, we introduce three *TESS* transits. We present two independent TTV analyses. First, we use **EXOFASTv2** to jointly model the *Spitzer* and ground-based transits and to obtain the midpoint transit times. We then construct an O–C diagram and model the TTVs with **Exo-Striker**. Second, we reproduce our results with an independent photodynamical analysis. We recover a TTV mass for AU Mic c of $10.8^{+2.3}_{-2.2} M_{\oplus}$. We compare the TTV-derived constraints to a recent radial-velocity (RV) mass determination. We also observe excess TTVs that do not appear to be consistent with the dynamical interactions of b and c alone, and do not appear to be due to spots or flares. Thus, we present a hypothetical non-transiting “middle-d” candidate exoplanet that is consistent with the observed TTVs, the candidate RV signal, and would establish the AU Mic system as a compact resonant multi-planet chain in a 4:6:9 period commensurability. These results demonstrate that the AU Mic planetary system is dynamically interacting producing detectable TTVs, and the implied orbital dynamics may inform the formation mechanisms for this young system. We recommend future RV and TTV observations of AU Mic b and c to further constrain the masses and to confirm the existence of possible additional planet(s).

1. INTRODUCTION

Exoplanetary sciences have been expanding over the past few decades, with its fields increasingly diversifying thanks in large part to several successful and diligent missions, includ-

ing *Kepler* (Borucki et al. 2010), *K2* (Howell et al. 2014), and the *Transiting Exoplanet Survey Satellite* (*TESS*, Ricker et al. 2015). *TESS* has detected 4 548 transiting candidates (TOIs) as of 2021 October 7 and 159 confirmed plan-

ets as of 2021 October 4¹. Many discoveries have challenged our theories of planet formation, such as hot Jupiters – e.g., 51 Pegasi b (Mayor & Queloz 1995), HD 209458 b (Henry et al. 2000), TOI-628 b (Rodriguez et al. 2021) – planets in highly eccentric orbit – e.g., 16 Cygni B b (Cochran et al. 1997), BD+63 1405 b (Dalal et al. 2021), HD 26161 b (Rosenthal et al. 2021) – and compact systems – e.g., HD 108236 (Daylan et al. 2021; Bonfanti et al. 2021), TOI-178 (Leleu et al. 2021), TRAPPIST-1 (Gillon et al. 2016, 2017a). One way to investigate how these systems form and evolve can be done by probing young stellar systems, when their characteristics and orbital dynamics are still undergoing progression. Several young exoplanet systems have recently been discovered by the *TESS* and *K2* missions – e.g., DS Tucanae A (Newton et al. 2019), K2-25 (Mann et al. 2016), K2-33 (David et al. 2016), V1298 Tauri (David et al. 2019) – and other exoplanet detection methods including direct imaging and radial velocities (RVs) – e.g., HD 47366 (Sato et al. 2016), HR 8799 (Marois et al. 2008, 2010), PDS 70 (Keppler et al. 2018; Haffert et al. 2019), β Pictoris (Lagrange et al. 2009, 2019). Further probing of certain systems such as PDS 70 revealed a potentially moon-forming circumplanetary disk around PDS 70 c (Benisty et al. 2021). This new and growing population of transiting young exoplanets has recently enabled a new frontier in the study of planet formation and evolution. Among the nearby young exoplanet systems, the nearest one is AU Microscopii (Tables 1 & 2).

AU Microscopii (TOI-2221, TIC 441420236, HD 197481, GJ 803) is a young (22 ± 3 Myr, Mamajek & Bell 2014), nearby (9.7 pc, Bailer-

Table 1. Stellar properties for host star AU Mic.

Property	Unit	Quantity	Ref
Spectral Type	...	M1Ve	...
m_V	...	8.81 ± 0.10	...
m_{TESS}	...	6.755 ± 0.032	...
α_{J2000}	h:m:s	20:45:09.53	1
δ_{J2000}	deg:am:as	-31:20:27.24	1
μ_α	mas/yr	281.424 ± 0.075	1
μ_δ	mas/yr	-359.895 ± 0.054	1
Distance	pc	9.7221 ± 0.0046	2
Parallax	mas	102.8295 ± 0.0486	1
M_\star	M_\odot	0.50 ± 0.03	3
R_\star	R_\odot	0.75 ± 0.03	4
T_{eff}	K	3700 ± 100	5
L_\star	L_\odot	0.09	5
Age	Myr	22 ± 3	6
P_{rot}	days	4.863 ± 0.010	3
$v \sin i$	km/s	8.7 ± 0.2	7

References—(1) Gaia Collaboration (2018); (2) Bailer-Jones et al. (2018); (3) Plavchan et al. (2020); (4) White et al. (2019); (5) Plavchan et al. (2009); (6) Mamajek & Bell (2014); (7) Lannier et al. (2017)

Jones et al. 2018) BY Draconis variable star with spectral type M1Ve and relative brightness $m_V=8.81$ mag. It is known to be fairly active, with numerous flares having been observed and studied at various wavelengths (Butler et al. 1981; Kundu et al. 1987; Cully et al. 1993; Tsikoudi & Kellett 2000; Gilbert et al. 2021). Kalas et al. (2004) observed the presence of a large dust disk having a radius between 50 and 210 au from the young star, having first been detected as a mid-infrared flux excess with *IRAS* (Fajardo-Acosta et al. 2000; Zuckerman 2001; Song et al. 2002; Liu et al. 2004; Plavchan et al. 2005). Later, Plavchan et al. (2020) discovered a Neptune-sized transiting planet AU Mic b interior to a spatially-resolved debris disc and with orbital period of 8.46 days. Recently, Gilbert et al. (2021) and Martioli et al. (2021) confirmed the existence of another planet AU Mic c with orbital period of 18.86 days, which put the planets near a 4:9 orbital commensurability. The aforementioned traits of AU Mic

¹ <https://exoplanetarchive.ipac.caltech.edu>

Table 2. Planetary properties for AU Mic system.

Property	Description	Unit	AU Mic b	AU Mic c	Ref
P_{orb}	Orbital Period	days	$8.4630004^{+0.0000058}_{-0.0000060}$	$18.858982^{+0.000053}_{-0.000050}$	1
a	Semi-Major Axis	au	0.0645 ± 0.0013	0.1101 ± 0.0022	2
e	Eccentricity	...	$0.12^{+0.16}_{-0.08}$	$0.13^{+0.16}_{-0.09}$	1
i	Inclination	deg	89.5 ± 0.3	$89.0^{+0.5}_{-0.4}$	2
ω	Argument of Periastron	deg	$-0.3^{+2.4}_{-2.3}$	$-0.3^{+2.5}_{-2.2}$	1
M_{p}	Planetary Mass	M_{J}	0.054 ± 0.015	$0.007 < M_{\text{c}} < 0.079$	2
		M_{\oplus}	17 ± 5	$2 < M_{\text{c}} < 25$	
R_{p}	Planetary Radius	R_{J}	$0.374^{+0.021}_{-0.020}$	$0.249^{+0.028}_{-0.027}$	1
		R_{\oplus}	$4.19^{+0.24}_{-0.22}$	$2.79^{+0.31}_{-0.30}$	
ρ_{p}	Planetary Density	g/cm^3	1.4 ± 0.4	$0.4 < \rho_{\text{c}} < 4.1$	2
K	RV Semi-Amplitude	m/s	$8.5^{+2.3}_{-2.2}$	$0.8 < K_{\text{c}} < 9.5$	2
$T_{\text{C}} - 2458000$	Time of Conjunction	BJD	330.39051 ± 0.00015	342.2223 ± 0.0005	2
t_{duration}	Transit Duration	hours	3.50 ± 0.08	4.5 ± 0.8	2
R_{p}/R_{\star}	0.0512 ± 0.0020	$0.0340^{+0.0034}_{-0.0033}$	1
a/R_{\star}	19.1 ± 0.3	29 ± 3	2
b	Impact Parameter	...	$0.16^{+0.13}_{-0.11}$	$0.30^{+0.21}_{-0.20}$	1

References—(1) Gilbert et al. (2021); (2) Martioli et al. (2021)

and its planets make this system a unique, viable laboratory for studying the stellar activity of a young M dwarf, the planetary formation, the evolution of exoplanet radii as a function of age, orbital architectures of young giant planet systems, atmospheric characteristics of young exoplanets, and the interplay between planets and disks.

One method that serves as a useful tool for probing the exoplanetary systems is Transit Timing Variations (TTVs). Compared to other detection methods, TTVs can detect terrestrial-mass planets with greater ease (Holman & Murray 2005). The planets that are in orbital resonance with each other can amplify the TTV signals (Agol et al. 2005), so TTVs can be used to search for and measure the masses of other planets within a given stellar system (e.g., including noteworthy systems presented in Mazeh et al. 2013; Becker et al. 2015; Gillon et al. 2017a; Grimm et al. 2018). Many systems have been characterized with TTVs, such as HIP 41378 (Bryant et al. 2021), K2-146 (Lam et al. 2020), TOI-216 (Dawson et al. 2021), TOI-1266 (Demory et al. 2020), TrES-3 (Mannaday

et al. 2020), and many Kepler systems (Lithwick et al. 2012; Mazeh et al. 2013; Hadden & Lithwick 2014). Martioli et al. (2021) searched for the TTVs of AU Mic transits from *TESS* light curves but did not identify any significant TTVs. Szabó et al. (2021) did a TTV joint model with *TESS* and *CHEOPS* data; they found AU Mic b’s ~ 3.9 -minute variation across 33 days and attributed AU Mic c as the potential source of this perturbation. Gilbert et al. (2021) performed an independent analysis of AU Mic transits from *TESS* light curves and were able to detect the TTVs on the order of ~ 80 seconds.

For this paper, we examine the TTVs of AU Mic planets by incorporating additional ground and space observations to our analysis. We present the TTVs of AU Mic b and c to recover constraints on the mass for AU Mic c and which indicates the presence of TTV excess that cannot be accounted by both planets b and c alone. In §2, we list the light curve data we include for TTV analysis and elaborate on some of the processes that were involved in data reduction. §3 covers the two critical developments:

joint-modeling both the ground-based photometric and *Spitzer* light curves and extracting the midpoint transit times from these sets using the `EXOFASTv2` package (Eastman et al. 2019), and constructing the O–C diagram using the extracted midpoint times from the observations. Then, as explained in §4, we model the extracted TTVs using the `Exo-Striker` package (Trifonov 2019). Next, we attempt to reproduce our results with an independent and direct photodynamical analysis as described in §5. Lastly, we discuss the results in §6 and close this paper in §7.

2. DATA FROM OBSERVATIONS

We obtained 23 AU Mic b transits and 3 AU Mic c transits from three years worth of observations with multiple telescopes and have included them in the analysis (Table 3). In addition to space-based observations, with original transit observations from *TESS* and follow-ups from *Spitzer*, we have utilized several ground-based facilities in conducting follow-ups of AU Mic, including *Brierfield*, *LCO SAAO*, *LCO SSO*, & *PEST* for photometric observations and *CFHT* equipped with *SPIRou*, *IRTF* equipped with *iSHELL*, & *VLT* equipped with *ESPRESSO* for Rossiter-McLaughlin (R-M) observations (Tables 4 & 5). The *TESS* transits and one of the *Spitzer* transits have been previously presented in Plavchan et al. (2020); Gilbert et al. (2021); Martioli et al. (2021), and the R-M observation in Martioli et al. (2020); Palle et al. (2020). The following subsections detail each telescope and the methodology employed upon its respective data sets.

*TESS*² is a space-based telescope designed to scan nearby bright F5–M5 stars for transiting exoplanets (Ricker et al. 2015). Since its launch on 2018 April 18 and the start of its primary mission on 2018 July 25, *TESS* has been probing the sky for ~ 3 years as of this writing and has made numerous groundbreaking contributions to planetary detection – e.g., DS Tuc A (Newton et al. 2019), TOI-700 (Gilbert et al. 2020), TOI-1338 (Kostov et al. 2020). Its two-year primary mission divided the sky into the Southern and the Northern Ecliptic Hemispheres, with each being divided further into 13 sectors. *TESS* began its search in the Southern Ecliptic Hemisphere and probed each sector for 28 days. Within each 28-day span, a subset of primary exoplanet transit search target stars in a given sector were monitored at 2-minute cadence, and Full Frame Images (FFIs) were collected at 30-minute cadence. The data collected by *TESS* are then processed by the Science Processing Operations Center (SPOC), which functions to generate the calibrated images, perform aperture photometry, remove systematic artifacts, and searches the light curves for transiting planet signatures (Jenkins et al. 2016). *TESS* successfully completed its two-year primary mission and is now in its extended mission by repeating its observation in each of 26 sectors, with some notable differences: *TESS* is probing or will probe new targets along with the old targets, the 2-minute cadence for 20 000 targets per sector is boosted with 20-second cadence for 1 000 targets per sector, and FFIs are retrieved at a shorter 10-minute cadence.

TESS observed AU Mic (Figure 1) at 2-minute cadence during Cycle 1 (Sector 1, 2018 July 25

² <https://tess.mit.edu>
<https://heasarc.gsfc.nasa.gov/docs/tess>

2.1. *TESS* Photometry

Table 3. List of AU Mic observation data incorporated for TTV analysis. All ground-based photometric observations listed here were organized via TESS Follow-up Observing Program (TFOP) Working Group (WG)^a.

Planet	Telescope	Date (UT)	Filter	Exposure Time (sec)	No. of Images	Obs. Dur. (min)	Transit Coverage	Ref
b	<i>Brierfield</i> 0.36 m	2020-08-13	I	16	398	379	full	...
b	<i>CFHT (SPIRou)</i>	2019-06-17	955-2 515 nm	122.6	116	302.8	egress	1
b	<i>IRTF (iSHELL)</i>	2019-06-17	2.18-2.47 nm	120	47	105.2	egress	1
b	<i>LCO SAAO</i> 1.0 m	2020-05-20	Pan-STARRS Y	35	99	262	egress	...
		2020-05-20	Pan-STARRS z _S	15	333	266	egress	
		2020-06-06	Pan-STARRS z _S	15	266	218	egress	
		2020-06-23	Pan-STARRS z _S	15	223	183	egress	
		2020-09-07	Pan-STARRS z _S	15	211	172	ingress	
		2020-10-11	Pan-STARRS z _S	15	311	266	ingress	
b	<i>LCO SSO</i> 1.0 m	2020-04-25	Pan-STARRS Y	35	40	104	egress	...
		2020-04-25	Pan-STARRS z _S	15	212	172	egress	
		2020-08-13	Pan-STARRS z _S	15	379	312	full	
		2020-09-16	Pan-STARRS z _S	15	408	340	full	
		2020-10-03	Pan-STARRS z _S	15	248	219	egress	
b	<i>PEST</i> 0.30 m	2020-07-10	V	15	1 143	556	full	...
b	<i>Spitzer (IRAC)</i>	2019-02-10	4.5 μm	0.08	3 020	475.7	full	...
		2019-02-27	4.5 μm	0.08	3 377	475.7	egress	
		2019-09-09	4.5 μm	0.08	6 002	990.9	full	
b	<i>TESS</i> ^b	2018-07-26	TESS	120	329	718.0	full	2
		2018-08-12	TESS	120	296	708.0	full	
		2020-07-10	TESS	20	2 132	719.7	full	
		2020-07-19	TESS	20	2 137	719.7	full	
		2020-07-27	TESS	20	2 120	719.7	full	
c	<i>TESS</i> ^b	2018-08-11	TESS	120	342	718.0	full	2
		2020-07-09	TESS	20	2 138	719.7	full	
		2020-07-28	TESS	20	2 133	719.7	full	
b	<i>VLT (ESPRESSO)</i>	2019-08-07	378.2-788.7 nm	200	88	359	full	3

^a<https://tess.mit.edu/followup>

^b ~12-hour snippets of the ~27-day duration *TESS* Cycle 1 and 3 light curves were extracted for our analysis, centered approximately on each transit.

References—(1) Martioli et al. (2020); (2) Gilbert et al. (2021); (3) Palle et al. (2020)

19:00:27 UT to 2018 August 22 16:14:51 UT)³ using Camera 1 CCD 4. This set has a 1.13-day gap due to data downlink. During its observation between 2018 August 16 16:00 UT and 2018 August 18 16:00 UT, the Fine Pointing

mode calibration was not configured optimally, culminating in poorer data quality due to excessive spacecraft pointing jitter. Gilbert et al. (2021) employed the data quality flags to filter out the problematic part of the data set, resulting in some additional gaps in data. *TESS* observed AU Mic again during Cycle 3 (Sector 27, 2020 July 05 18:31:16 UT to 2020 July 30

³ The following Guest Investigator (GI) proposals were awarded for AU Mic’s Cycle 1 observations: G011176/PI Czekala, G011185/PI Davenport, G011264/PI Davenport, G011180/PI Dressing, G011239/PI Kowalski, G011175/PI Mann, & G011266/PI Schlieder.

Table 4. List of facilities utilized for photometric and Rossiter-McLaughlin follow-up observations of AU Mic.

Telescope	Instrument	Location	Aperture (m)	Pixel Scale (arcsec)	Resolution (pixels)	FOV (arcmin)	Ref
<i>Brierfield</i>	<i>Moravian 16803</i>	Bowral, New South Wales	0.36	0.732	4 096×4 096	50×50	1
<i>CFHT</i>	<i>SPIRou</i>	Maunakea, Hawai‘i	3.58	2
<i>IRTF</i>	<i>iSHELL</i>	Maunakea, Hawai‘i	3.2	3
<i>LCO SAAO</i>	<i>Sinistro</i>	Sutherland, South Africa	1.0	0.389	4 096×4 096	26.5×26.5	4
<i>LCO SSO</i>	<i>Sinistro</i>	Mount Woorut, New South Wales	1.0	0.389	4 096×4 096	26.5×26.5	4
<i>PEST</i>	<i>SBIG ST-8XME</i>	Perth, Western Australia	0.3048	1.23	1 530×1 020	31×21	5
<i>Spitzer</i>	<i>IRAC</i>	...	0.85	1.22	256×256	5.2×5.2	6
<i>VLT</i>	<i>ESPRESSO</i>	Cerro Paranal, Chile	8.2	7

References—(1) <https://www.brierfieldobservatory.com>; (2) <https://www.cfht.hawaii.edu>; (3) <http://irtfweb.ifa.hawaii.edu>; (4) <https://lco.global/observatory>; (5) <http://pestobservatory.com>; (6) <https://www.spitzer.caltech.edu>; (7) <https://www.eso.org/public/teles-instr/paranal-observatory/vlt>

Table 5. Specifications of instruments used for ground-based Rossiter-McLaughlin follow-up observations of AU Mic.

Instrument	Telescope	Observing Mode	λ Range (nm)	Resolving Power	Aperture (arcsec)	Average SNR	Ref
<i>ESPRESSO</i>	<i>VLT</i>	HR (1-UT)	378.2-788.7	140 000	1.0	93.9	1
<i>iSHELL</i>	<i>IRTF</i>	K_{gas}	2.18-2.47	75 000	0.125	65	2, 4
<i>SPIRou</i>	<i>CFHT</i>	Stokes V Spectropolarimetric	955-2 515	70 000	1.29	242	3, 4

References—(1) Donati et al. (2020), Palle et al. (2020); (2) Rayner et al. (2016); (3) Pepe et al. (2021); (4) Martioli et al. (2020)

03:21:15 UT)⁴, this time at both 20-second and 2-minute cadences, with the latter constructed by co-added six 20-second exposures. The data downlink during this period led to a 1.02-day gap in the data.

We use the AU Mic *TESS* Cycle 1 and 3 transit light curves from Gilbert et al. (2021) for our primary TTV analysis (§4), and herein we summarize their analysis. In our independent photodynamical analysis (§5), we reanalyze the *TESS* light curves directly. The AU Mic

TESS Cycle 1 and 3 light curves were retrieved from the Mikulski Archive for Space Telescopes (MAST)⁵ archive using the `lightkurve` package (Lightkurve Collaboration et al. 2018) while setting its bitmask filter to “default”. The Presearch Data Conditioning (PDC SAP) light curves were chosen since they addressed crowding and instrumental systematics (Smith et al. 2012; Stumpe et al. 2012, 2014). After filtering the NaNs out of the data sets, 25.07 days of Cycle 1, 23.29 days of 2-minute Cycle 3, and 22.57 days of 20-second Cycle 3 are left. Next, the Savitzky-Golay filter is applied to the light curves to smooth out AU Mic’s spot modulation. Since the flares are abundant in *TESS*

⁴ The following GI proposals were awarded for AU Mic’s Cycle 3 observations: G03272/PI Burt, G03227/PI Davenport, G03063/PI Llama, G03228/PI Million, G03205/PI Monsue, G03141/PI Newton, G03202/PI Paudel, G03263/PI Plavchan, G03226/PI Silverstein, & G03273/PI Vega.

⁵ <https://archive.stsci.edu>

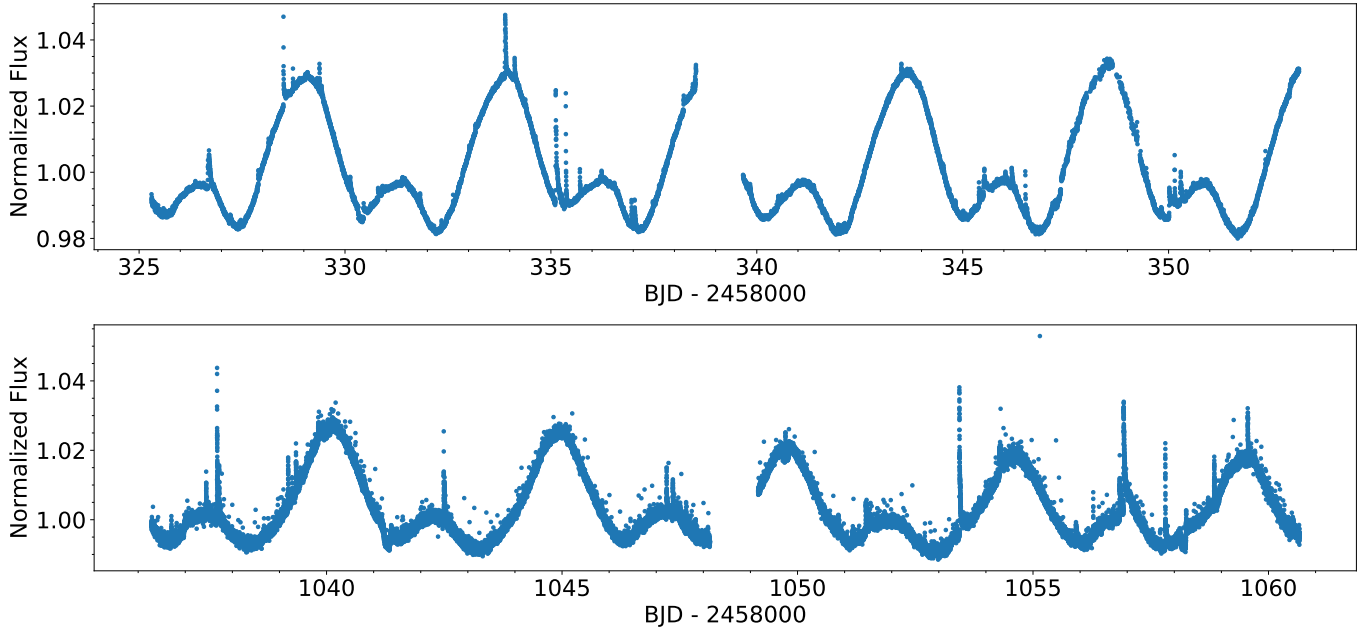


Figure 1. *TESS* photometry of AU Mic. The blue points are *TESS* measurements. The top plot is from Cycle 1 (Sector 1, 2018 July 25 19:00:27 UT – 2018 August 22 16:14:51 UT), 2-minute cadence. The bottom plot is from Cycle 3 (Sector 27, 2020 July 05 18:31:16 UT – 2020 July 30 03:21:15 UT), 20-second cadence.

light curves, especially during most of AU Mic b’s and c’s transits, the `bayesflare` (Pitkin et al. 2014) and `xoflares` packages were used to extract and model the flares instead of trimming the flares out as in Plavchan et al. (2020). Then, the `celerite2` package (Foreman-Mackey et al. 2017; Foreman-Mackey 2018) was applied to model the stellar variability of AU Mic, and the `exoplanet` package (Foreman-Mackey et al. 2021) was utilized to model the transits of AU Mic b and c.

2.2. *Spitzer* (IRAC) Photometry

The *Spitzer Space Telescope*⁶ was constructed as part of NASA’s Great Observatories Program’s final mission to probe various astrophysical objects at infrared wavelengths (Werner et al. 2004). Launched in 2003 August 25, *Spitzer* carried out its primary mission along with NASA’s Astronomical Search for Origins Program for 5.75 years until the liquid helium coolant was depleted on 2009 May 15; after-

ward, it continued under several extended missions – starting with the *Spitzer* Warm mission, then the *Spitzer* Beyond mission, and finally the *Spitzer* Final Voyage mission – for the next 10.5 years starting from 2009 July 27 until its decommission on 2020 January 30. *Spitzer* fulfilled an indispensable role in characterizing exoplanets (Deming & Knutson 2020) – e.g. including some benchmark systems observed, HD 189733 b (Grillmair et al. 2007; Todorov et al. 2014), HD 209458 b (Zellem et al. 2014), HD 219134 b & c (Gillon et al. 2017b), TRAPPIST-1 b through h (Morris et al. 2018; Zhang et al. 2018; Ducrot et al. 2018, 2020), WASP-26 b (Mahtani et al. 2013).

To collect more data on the planetary object detected by *TESS*, *Spitzer* Director’s Discretionary Time (DDT) observations were proposed and awarded (PID 14214 & 14241) in the final year of operations for observations of AU Mic with the *Infrared Array Camera* (IRAC, Fazio et al. 2004) due to possible calculated transits on 2019 February 10 & 27 and September 10, which are presented in this pa-

⁶ <https://www.spitzer.caltech.edu>

per. *Spitzer* observed AU Mic with *IRAC* on five occasions during the *Spitzer* Beyond and Final Voyage missions (2019 February 10 10:58:58 to 18:54:38 UT, 2019 February 27 09:46:23 to 17:42:02 UT, 2019 September 9 13:50:57 to 21:46:45 UT, 2019 September 9 23:26:02 UT to 2019 September 10 06:21:54 UT, & 2019 September 14 03:40:07 to 12:33:36 UT). The first two observations were originally considered to be eclipses from the initially assumed orbital period for AU Mic b from the *TESS* mission Cycle 1 observations. However, these observations detected additional transits of AU Mic b, establishing a true period to be half as long as originally thought (Plavchan et al. 2020). The third observation is of a transit search for an originally estimated but incorrect period for AU Mic c, and the fourth observation is of a third transit of AU Mic b; these two observations have been combined into one light curve set for this analysis. The final observation is a secondary eclipse search of AU Mic b which will be described and analyzed in a separate paper and is not included in this work.

All of the observations were taken using the 32×32 pixel sub-array mode with an exposure time of 0.08 seconds to avoid saturation on the star (measurement cadence is 0.1 seconds). After placing the star on the “sweet-spot” pixel, using the pointing calibration and reference sensor (PCRS) peak-up mode (Ingalls et al. 2012), we exposed with continuous staring (no dithers). The observations were all taken at 4.5 μm , as this channel has a lower systematics due to the intra-pixel sensitivity. The coordinates were adjusted for the high parallax and proper motion of AU Mic for the proposed observation dates. Each observation set consisted of a 30-minute pre-stare dither pattern, an 8-hour stare, and a 10-minute post-staring dither pattern. All data were calibrated by the *Spitzer*

pipeline S19.2 and can be accessed using the *Spitzer* Heritage Archive (SHA)⁷.

For each of the three transit observations discussed here, the following data reduction steps were performed on each AU Mic stellar image measured on 0.1-second intervals. We used the IDL routine `box_centroider`⁸ supplied by the *Spitzer* Science Center to measure the location of AU Mic on the pixel. We then performed aperture photometry on each image using the IDL Astronomy Users Library routine `aper`⁹ with a fixed aperture of 2.25 pixels and subtracting a sky annulus of 3-7 pixels about the centroid.

All *IRAC* photometry at 4.5 μm contain instrumental systematics caused by the coupling between spacecraft pointing fluctuations and drifts with intra-pixel sensitivity variations. For the three transit observations analyzed here, we take three approaches for detrending the instrument systematics and compare the results. First, as in Plavchan et al. (2020), we detrended this effect using an independent pixel mapping dataset measured for non-variable star BD+67 1044 (Ingalls et al. 2018). Because this calibration star doesn’t intrinsically vary, we take its photometric variations to reflect the pixel sensitivity map. We estimated the relative pixel sensitivity at the (x, y) centroid locations of each AU Mic observation using the K-Nearest Neighbors with Kernel Regression technique described by Ingalls et al. (2018) and divided all AU Mic measurements by the sensitivities. This approach was published for the first *Spitzer* transit in Plavchan et al. (2020). However, we noticed that additional high-frequency (shorter than the transit duration) photometric variability remained in the light curve that looked

⁷ <http://sha.ipac.caltech.edu>

⁸ https://irsa.ipac.caltech.edu/data/SPITZER/docs/irac/calibrationfiles/pixelphase/box_centroider.pro

⁹ <https://idlastro.gsfc.nasa.gov/ftp/pro/idlphot/aper.pro>

like astrophysical “hot spot” crossings. But we subsequently identified a strong correlation of these light curve features with the *Spitzer* PSF FWHM. Therefore, second, we detrend the light curve using both the trend time series for the pixel centroid motion and the PSF FWHM; this is the systematic-detrended time series that we adopt in this work for further analysis. Third, we also tested the noise-pixel technique detailed by Lewis et al. (2013) and achieve qualitatively similar results to our second approach.

We modeled the *IRAC* intra-pixel sensitivity (Ingalls et al. 2016) using a modified implementation of the BLISS (BiLinearly-Interpolated Sub-pixel Sensitivity) mapping algorithm (Stevenson et al. 2012). We used a modified version of the BLISS mapping (BM) approach to mitigate the correlated noise associated with intra-pixel sensitivity. In our photometric baseline model, we complement the BM correction with a linear function of the Point Response Function (PRF) Full Width at Half-Maximum (FWHM). In addition to the BM, our baseline model includes the PRF’s FWHM along the x and y axes, which significantly reduces the level of correlated noise as shown in previous studies (e.g., Lanotte et al. 2014, Demory et al. 2016a, Demory et al. 2016b, Gillon et al. 2017a, Mendonça et al. 2018). Our baseline model does not include time-dependent parameters. Our implementation of this baseline model is included in a Markov Chain Monte Carlo (MCMC) framework already presented in the literature (Gillon et al. 2012). We run two chains of 200 000 steps each and check for convergence and efficient mixing using the Gelman-Rubin statistic (Gelman & Rubin 1992); all of the chains have converged with their GR statistic < 1.01 .

We next construct a 2nd-order polynomial model fit to account for the rotational modulation of stellar activity present in the three *Spitzer* light curves. AU Mic is active with

its rotational modulation of stellar activity, and on the timescale of a transit duration can be described by a 2nd-order polynomial (Addison et al. 2020); longer timescales would necessitate a Gaussian Process or similar analysis as undertaken in Plavchan et al. (2020) and Gilbert et al. (2021) for the *TESS* transits. These polynomial coefficients are marginalized over in our TTV analysis to account for the timing uncertainties introduced from the rotational modulation of stellar activity. We cross-check our approach to that using a Gaussian Process model in Plavchan et al. (2020) and derive consistent TTVs and corresponding uncertainties.

The second *Spitzer* transit also has an unusual “jump” feature during the middle of the transit that was thought to be caused by either a flare or a transit egress of another planet; we do not identify any systematic indicator that this jump coincides with. We explored the timing of AU Mic c’s transits but found that none line up with the *Spitzer*’s transit of AU Mic b. So instead we constructed and fit a custom flare model for this feature, consisting of a linear rapid rise followed by an exponential decay. The amplitude of the flare model is marginalized over in our analysis of the TTVs to account for the impact it has on the transit times; however, the flare rise, peak, and decay times are fixed in our analysis. The adopted flare rise and decay times are informed by and consistent with the characterization of the flares in the *TESS* light curve analyzed in Gilbert et al. (2021). Here, the 2nd-order polynomial coefficients are degenerate with the flare times and are marginalized over to account for the impact the flare has in our derived transit time and uncertainty. Since the flare did not occur during ingress or egress, it has minimal impact on our derived transit midpoint time and corresponding uncertainty.

The third *Spitzer* light curve was additionally detrended with an ad hoc Gaussian model given the presence of a low-level Gaussian-like trend

coincident with the transit midpoint time (note, not a Gaussian Process, but a Gaussian change in brightness with time). Again, we do not identify a systematic indicator correlated with this brightness variation in the light curve and associate it with an astrophysical origin for AU Mic. The amplitude of the Gaussian model is marginalized over in our analysis to assess its impact on the TTVs, but the width and peak time were fixed; in this case, marginalizing over the 2nd-order polynomial coefficients in our model again compensates for and is degenerate with any error in the fixed Gaussian centroid time and width. The astrophysical origins of this brightness change and its coincidence with the transit midpoint time, as well as other remaining residuals present in the AU Mic *Spitzer* light curves as seen in Figure 2, are beyond the scope of this work and are the subject of a future publication.

For all but one detrending time series, the additive coefficients were set to zero and the multiplicative coefficients were set to one. The exception is the flare detrending from the second *Spitzer* set, with the additive coefficient set to one and the multiplicative coefficient set to zero. Afterward, we did a joint model of the *Spitzer* and ground-based photometric transits using the EXOFASTv2 package (Eastman et al. 2019). This process to extract the midpoint transit times from the *Spitzer* light curves is explained in more details in §3.

2.3. Rossiter-McLaughlin Spectroscopy

The Rossiter-McLaughlin (R-M) technique is an advantageous tool in detecting and characterizing transiting exoplanets, including determining their spin-orbit alignments (Ohta et al. 2005; Winn 2007; Triaud 2018). The R-M effect is observed when the planet crosses the host star during the RV observation, blocking a portion of the star’s rotational signal and generating a characteristic feature on the time series RV profile (Holt 1893; Rossiter 1924; McLaughlin 1924;

Ohta et al. 2005; Winn 2007). Many exoplanets have been characterized with R-M’s – e.g. including some benchmark systems, CoRoT-3 b & HD 189733 b (Triaud et al. 2009), KELT-20 b (Rainer et al. 2021), K2-232 b (Wang et al. 2021), TOI-1431 b (Stangret et al. 2021), WASP-17 b (Anderson et al. 2010).

R-M observation also offer an additional way in which to derive transit mid-point times independent of photometric observations, a method that has not previously been commonly used for TTV analysis because it is resource-intensive with its use of high-resolution spectrometers on large aperture telescopes. Today, however, *TESS* mission candidates are relatively brighter and nearby compared to *Kepler* systems, and more amenable to R-M observations. We include transit midpoint times derived from two R-M observations of AU Mic b’s transits that were obtained at relatively important epochs shortly after the *Spitzer* observations and between the two-year gap in the *TESS* observations. The first was collected using the *SPIRou* and *iSHELL* instruments, and the second the *ESPRESSO* instrument. We retrieved the two transit midpoint times from Martioli (2020, private communication) and Pallé (2020, private communication), respectively. The following sections summarize the work done by Martioli et al. (2020) and Pallé et al. (2020) on processing the respective *SPIRou* + *iSHELL* and *ESPRESSO* data.

2.3.1. CFHT (*SPIRou*) & IRTF (*iSHELL*) Spectroscopy

The *SpectroPolarimètre InfraRouge* (*SPIRou*)¹⁰, mounted on the 3.6 m *Canada-France-Hawai’i Telescope* (*CFHT*) located atop Maunakea, Hawai’i, is a high-resolution near-infrared (NIR) spectrometer that is capable of imaging in YJHK bands (0.95-2.5 μm) with

¹⁰ <https://www.cfht.hawaii.edu/Instruments/SPIRou>

a resolving power of $\sim 70\,000$ and is equipped with a fiber-fed cryogenic high-resolution échelle spectrograph that can perform high-precision velocimetry and spectropolarimetry, which allows it to simultaneously observe magnetic features and stellar activities of the host stars (Donati et al. 2020). The *iSHELL*¹¹, installed on the 3.2 m *NASA Infrared Telescope Facility* (*IRTF*) also located atop Maunakea, Hawai‘i, is a high-resolution 1.1-5.3 μm spectrometer with a resolving power of 75 000 and was designed to replace *CSHELL* as an instrument with enhanced spectroscopic capabilities (Rayner et al. 2016). These qualities make *SPIRou* and *iSHELL* useful tools to carry out follow-up observations on transiting exoplanets of young, active M dwarfs (Morin et al. 2010; Afram & Berdyugina 2019), such as AU Mic.

As part of the *SPIRou* Legacy Survey’s Work Package 2 (WP2) (Donati et al. 2020), Martioli et al. (2020) observed AU Mic on 2019 June 17 10:10:56 to 15:13:45 UT with *SPIRou* set in Stokes V spectropolarimetric mode and captured an egress of AU Mic b. 116 spectra were collected that night, each taken at 122.6 seconds exposure, with the average SNR of 242. Martioli et al. (2020) also used *iSHELL* set at K_{gas} mode for simultaneous but shorter observation of AU Mic (2019 June 17 11:08:19 to 12:53:32 UT); 47 120-second spectra were collected with that instrument, with SNR of ~ 60 -70. The typical seeing condition was $0.96 \pm 0.13''$, the initial and final airmass were 2.9 and 1.8, respectively, with its minimum being 1.59, and the Moon was 99% illuminated and 40.3° from the target.

Martioli et al. (2020) implemented the reduction pipeline APERO (A PipelinE to Reduce Observations, Cook et al. in prep.) to reduce and process the *SPIRou* data and to calculate the cross-correlation functions (CCFs). Next, the “M2_weighted_RV_-5.mas” line mask

was applied to the spectra, and the lines were masked if their telluric absorption is deeper than 40%. The line mask then underwent further refinement by removing lines not present in AU Mic’s Stokes-I spectrum using the technique from Moutou et al. (2020). The CCFs were calculated from each spectral order and summed to achieve greater precision, then the RVs were measured from the CCF by using the velocity shift’s least-square fit. The *iSHELL* RVs were extracted using the *pychell* pipeline, and yielded consistent RVs and precision with the *SPIRou* RVs (Cale et al. 2019).

Next, Martioli et al. (2020) constructed the R-M model using the *emcee* Markov chain Monte Carlo (MCMC) package (Foreman-Mackey et al. 2013) and the stellar activity model using the approach from Donati et al. (1997). The stellar activity model was then subtracted from the measured RVs, and the R-M model was then applied as a correction to the subtracted RVs. Finally, Martioli (2020, private communication) modeled AU Mic b’s mid-point time from *SPIRou* + *iSHELL*’s best-fit subtracted and corrected RV model using $T_{\text{C}} = \mathcal{N}(2458330.39153, 0.00070)$ as a prior.

2.3.2. VLT (*ESPRESSO*) Spectroscopy

Echelle Spectrograph for Rocky Exoplanet and Stable Spectroscopic Observations (*ESPRESSO*)¹² is a high-precision RV spectrometer situated in the Combined-Coudé Laboratory (CCL) at the focus of the *Very Large Telescope* (*VLT*) atop Cerro Paranal, Chile (Pepe et al. 2021). Its spectrograph probes the sky at 378.2-788.7 nm range, and it can use either four 8.2 m telescopes (4-UT) with lower resolution of $\sim 70\,000$ or only one of them (1-UT) with higher resolutions of $\sim 140\,000$ in the

¹¹ <http://irtfweb.ifa.hawaii.edu/~ishell>

¹² <https://www.eso.org/sci/facilities/paranal/instruments/espresso.html>

High-Resolution (HR) mode or $>190\,000$ in the Ultra-High-Resolution (UHR) mode.

Palle et al. (2020) observed AU Mic on 2019 August 7 3:24 to 9:23 UT with *ESPRESSO* set at the standard HR (1-UT) mode and captured a full transit of AU Mic b. 88 spectra were collected that night, each taken at 200 seconds exposure. The SNR averaged around 93.9, the initial and final airmass were 1.03 and 2.37, respectively, with its minimum being 1.007, and the sky was clear.

Palle et al. (2020) applied several separate approaches in reducing and modeling the *ESPRESSO* data; however, we only highlight one of those approaches that provided us the midpoint time for this paper. The *SERVAL* package (Zechmeister et al. 2018) was implemented to extract and calibrate the spectra and generate the RV profile of AU Mic b. Next, the R-M effect was modeled using the combination of the *celerite* (Foreman-Mackey et al. 2017) package’s Gaussian process (GP) and *PyAstronomy* package (Czesla et al. 2019), and the stellar activity was modeled with GP described by a Matérn 3/2 kernel implemented by *celerite*. These models are then applied as corrections to the *ESPRESSO* RV profile. Pallé (2020, private communication) extracted the midpoint time from the *SERVAL* GP + *PyAstronomy* best-fit RV profile using $T_C = \mathcal{N}(2458702.77277, 0.00189)$ as a prior.

2.4. Ground-Based Photometry

The TESS Follow-up Observing Program (TFOP) Working Group (WG)¹³ coordinated numerous ground-based follow-ups for various TOIs, including AU Mic. As a result, 13 AU Mic follow-up photometric transit observations were made using different observatories: one *Brierfield* 0.36 m, six *LCO SAAO* 1.0 m, five *LCO SSO* 1.0 m, and one *PEST* 0.30 m. The

light curves from these observations are available online through ExoFOP-TESS¹⁴ (Akeson et al. 2013). The follow-up observation schedules were conducted with the online version of the TAPIR package (Jensen 2013). We utilized the *AstroImageJ* (AIJ, Collins et al. 2017) to process the ground-based light curves (except *PEST*, which was processed through their own pipeline) and then create a subset table containing only BJD_TDB, normalized detrended flux, flux uncertainty, and detrending columns from the ground-based light curves to prepare them for EXOFASTv2 modeling and extraction of midpoint times (§3). The following sub-subsections describe the role each telescope played in collecting and processing the light curves.

2.4.1. LCOGT (*Sinistro*) Photometry

We made use of two 1.0 m *LCO* Ritchey-Chretien Cassegrain telescopes, both equipped with *Sinistro*, that are part of the *Las Cumbres Observatory Global Telescope* network (*LCOGT*, Brown et al. 2013)¹⁵. Two of *Sinistro*’s filters used for AU Mic observations were Pan-STARRS Y and Pan-STARRS z_s , with their central wavelength peaks at 1004.0 and 870.0 nm, respectively. The third filter B was used for simultaneous observation with Y; however, the data collected with B are omitted from this paper due to non-detection of AU Mic b’s transits and more pronounced stellar activity in the bluer band.

LCO SSO, located on Mount Woorut near Coonabarabran, New South Wales, Australia, observed AU Mic on four separate nights (2020 April 25 16:03:03 to 17:49:38 UT at 35 seconds exposure with Y and 2020 April 25 16:00:47 to 18:52:43 UT, 2020 August 13 12:41:53 to 17:50:19 UT, 2020 September 16 09:12:31 to 14:41:47 UT, & 2020 October 3 09:17:36 to

¹³ <https://tess.mit.edu/followup>

¹⁴ <https://exofop.ipac.caltech.edu/tess>

¹⁵ <https://lco.global/observatory>

12:36:33 UT at 15 seconds exposure with z_s). 40 images from the first night were collected with Y, and 212, 379, 408, & 248 images from the respective first, second, third, & fourth nights were collected with z_s . An egress was captured on the first and fourth nights while a full transit was captured on the second and third nights.

LCO SAAO, located in Sutherland, South Africa, observed AU Mic on five separate nights (2020 May 20 22:53:29 UT to 2020 May 21 03:15:29 UT at 35 seconds exposure with Y and 2020 May 20 22:51:11 UT to 2020 May 21 03:17:38 UT, 2020 June 6 21:44:20 UT to 2020 June 7 01:22:36 UT, 2020 June 23 20:37:29 to 23:36:35 UT, 2020 September 7 21:55:46 UT to 2020 September 8 00:43:57 UT, & 2020 October 11 18:08:39 to 22:29:54 UT at 15 seconds exposure with z_s). 99 images from the first night were collected with Y, and 333, 266, 223, 211, & 311 images from the respective first, second, third, fourth, & fifth nights were collected with z_s . The second night’s photometric quality was impacted by a combination of clouds and a full Moon. An egress was captured on the first through third nights while an ingress was captured on the fourth and fifth nights.

All light curves from *LCOGT* were reduced and detrended with AIJ. For each *LCOGT* night, the following detrending parameters were applied: AIRMASS for UT2020-04-25 (Y), UT2020-05-20 (Y & z_s), UT2020-06-06, & UT2020-06-23; Width_T1 for UT2020-04-25 (z_s), UT2020-09-16, UT2020-10-03, & UT2020-10-11; AIRMASS + Width_T1 for UT2020-08-13; and Width_T1 + Sky/Pixel_T1 for UT2020-09-07. We also used AIJ to generate a subset table for each light curve.

2.4.2. *PEST (SBIG ST-8XME) Photometry*

*Perth Exoplanet Survey Telescope (PEST)*¹⁶, based in Perth, Western Australia, is a 12”

(0.3048 m) Meade LX200 Schmidt-Cassegrain Telescope that was equipped with SBIG ST-8XME camera at the time of the AU Mic observation. *PEST* observed AU Mic on 2020 July 10 13:26:53 to 22:42:33 UT with V and captured a full transit. 1143 images were collected, each at 15 seconds exposure. The *PEST* light curve was reduced and processed through the *PEST* pipeline¹⁷. We then use AIJ to create a subset table that included *PEST*-generated detrending parameters comp_flux + x_coord + y_coord + dist_center + fwhm + airmass + sky.

2.4.3. *Brierfield (Moravian 16803) Photometry*

The *Brierfield Observatory*¹⁸, located in Bowral, New South Wales, Australia, houses the 14” (0.36 m) Planewave Corrected Dall-Kirkham Astrograph telescope mounted with the instrument *Moravian G4-16000 KAF-16803*. *Brierfield* observed AU Mic on 2020 August 13 11:35:21 to 17:54:35 UT with I and captured a full transit. 398 images were collected, each at 16 seconds exposure. The *Brierfield* light curve was reduced and detrended with AIJ; the detrending parameters were Meridian_Flip + X(FITS)_T1 + Y(FITS)_T1 + tot_C_cnts. Afterward, a subset table was generated from this light curve with AIJ.

3. *TESS, Spitzer, & GROUND-BASED PHOTOMETRIC JOINT MODELING*

We use the *EXOFASTv2* package (Eastman et al. 2019) to model the transits and characterize our light curves. *EXOFASTv2* estimates the posterior probabilities through the Markov chain Monte Carlo (MCMC) to both determine the statistical significance of our ground-based & *Spitzer* detections and the confidence in the time of conjunction measurements to assess for the presence of detectable TTVs. Five *TESS*

¹⁶ <http://pestobservatory.com>

¹⁷ <http://pestobservatory.com/the-pest-pipeline>

¹⁸ <https://www.brierfieldobservatory.com>

Table 6. Stellar, planetary, and transit priors for EXOFASTv2 modeling with AU Mic’s eight *TESS*, three *Spitzer*, & 13 ground transits.

Prior	Unit	Input	
		AU Mic b	AU Mic c
$\log_{10} \left(\frac{M_{\star}}{M_{\odot}} \right)$...	$\mathcal{N}(-0.301, 0.026)$	
R_{\star}	R_{\odot}	$\mathcal{N}(0.75, 0.03)$	
T_{eff}	K	$\mathcal{N}(3700, 100)$	
Age	Gyr	$\mathcal{N}(0.022, 0.003)$	
Parallax	mas	$\mathcal{N}(102.8295, 0.0486)$	
T_C	BJD-TDB	$\mathcal{N}(2458330.39051)$	$\mathcal{N}(2458342.2223)$
$\log_{10} \left(\frac{\text{Period}}{\text{days}} \right)$...	$\mathcal{N}(0.92752436)$	$\mathcal{N}(1.2755182)$
R_p/R_{\star}	...	$\mathcal{N}(0.0512, 0.0020)$	$\mathcal{N}(0.0340, 0.0034)$
e	...	$\mathcal{N}(0.12, 0.16)$	$\mathcal{N}(0.13, 0.16)$
TTV Offset	days	$\mathcal{U}(-0.02, 0.02)$	
Depth Offset	...	$\mathcal{U}(-0.01, 0.01)$	

NOTE— \mathcal{N} denotes the Gaussian priors, and \mathcal{U} denotes the uniform priors. The Gaussian priors were taken from Tables 1 & 2, while the logarithmic functions were calculated. TTV and depth offsets are arbitrary and applied as constraints to all transits.

transits, three *Spitzer* transits and 13 ground-based photometric transits of AU Mic b and three *TESS* transits of AU Mic c are included in the model. The following detrending parameters are treated as additive: flare (*Spitzer*), sky (*Spitzer & PEST*), & Sky/Pixel_T1 (*LCO SAAO*); the remaining detrending parameters are treated as multiplicative.

The Gaussian priors from Table 6 were taken from Tables 1 and 2, while the logarithmic functions were calculated; the logarithmic version of stellar mass and orbital period were used because they are the fitted priors in EXOFASTv2. The TTV and depth offset priors were implemented to place constraints on the variation of transit timing and depth of all light curves; any transit depth variability is not investigated further herein. Since both Pan-STARRS Y and Pan-STARRS z_s are not available among the filters in EXOFASTv2, y and z’ (Sloan z) were used as respective approximate substitutes.

Table 7. Apparent magnitude priors for EXOFASTv2’s spectral energy distribution (SED) fitting of AU Mic. This is intended to place constraints on AU Mic’s MIST evolutionary models (Choi et al. 2016; Dotter 2016) and is applied only to the first of the two EXOFASTv2 runs

Band	Apparent Magnitude	Ref
Gaia	7.84 ± 0.02	1
Gaia _{BP}	8.94 ± 0.02	1
Gaia _{RP}	6.81 ± 0.02	1
J _{2M}	5.44 ± 0.02	2
H _{2M}	4.83 ± 0.02	2
K _{2M}	4.53 ± 0.02	3
B	10.06 ± 0.02	...
V	8.89 ± 0.18	...
gSDSS	9.58 ± 0.05	4
rSDSS	8.64 ± 0.09	4
iSDSS	7.36 ± 0.14	4

References—(1) Gaia Collaboration (2018); (2) Cutri et al. (2003); (3) Stauffer et al. (2010); (4) Zacharias et al. (2012)

Given that AU Mic is a low-mass red dwarf, we configured EXOFASTv2 to use MIST for evolutionary models (Choi et al. 2016; Dotter 2016) and ignore the Claret & Bloemen limb darkening tables (Claret & Bloemen 2011). Additionally, we incorporate the spectral energy distribution (SED) to place constraint on MIST evolutionary models; the bands and their corresponding magnitude priors are presented in Table 7. We also assume the orbit of both AU Mic b & c to be non-circular. For the EXOFASTv2 modeling, each of the 16 observations are detrended as indicated in Table 8; §2 describes additional details on detrending parameters used for each data set. We split up the EXOFASTv2 modeling into two sequential MCMC runs. For the first run, we integrate up to 15000 steps while setting $N_{\text{THIN}} = 12$; the first run was

Table 8. Detrending parameters incorporated into EXOFASTv2 modeling of AU Mic b transits. The flare (*Spitzer*), sky (*Spitzer* & *PEST*), & Sky/Pixel.T1 (*LCO SAAO*) were implemented as additives; the remaining detrending parameters were implemented as multiplicative. See §2 for details on detrending parameters used for each observation. Since both Pan-STARRS Y and Pan-STARRS z_s are not available among the filters in EXOFASTv2, y and z' (Sloan z) were used as respective approximate substitutes.

Telescope	Date (UT)	Filter	Detrending Parameter(s)	Note
<i>Spitzer</i>	2019-02-10	4.5 μm	$x, y, \text{noise/pixel}, \text{FWHM}_x, \text{FWHM}_y, \text{sky}, \text{linear}, \text{quadratic}$	1
<i>Spitzer</i>	2019-02-27	4.5 μm	$x, y, \text{noise/pixel}, \text{FWHM}_x, \text{FWHM}_y, \text{sky}, \text{linear}, \text{quadratic}, \text{flare}$	1
<i>Spitzer</i>	2019-09-09	4.5 μm	$x, y, \text{noise/pixel}, \text{FWHM}_x, \text{FWHM}_y, \text{sky}, \text{linear}, \text{quadratic}, \text{Gaussian}$	1
<i>LCO SSO</i>	2020-04-25	z'	Width.T1	2
<i>LCO SSO</i>	2020-04-25	y	AIRMASS	2
<i>LCO SAAO</i>	2020-05-20	z'	AIRMASS	2
<i>LCO SAAO</i>	2020-05-20	y	AIRMASS	2
<i>LCO SAAO</i>	2020-06-06	z'	AIRMASS	2
<i>LCO SAAO</i>	2020-06-23	z'	AIRMASS	2
<i>PEST</i>	2020-07-10	V	$\text{comp_flux}, x_coord, y_coord, \text{dist_center}, \text{fwhm}, \text{airmass}, \text{sky}$	3
<i>Brierfield</i>	2020-08-13	I	$\text{Meridian_Flip}, \text{X(FITS)_T1}, \text{Y(FITS)_T1}, \text{tot_C.cnts}$	2
<i>LCO SSO</i>	2020-08-13	z'	AIRMASS, Width.T1	2
<i>LCO SAAO</i>	2020-09-07	z'	Width.T1, Sky/Pixel.T1	2
<i>LCO SSO</i>	2020-09-16	z'	Width.T1	2
<i>LCO SSO</i>	2020-10-03	z'	Width.T1	2
<i>LCO SAAO</i>	2020-10-11	z'	Width.T1	2

¹See §2.2 for details on the detrending parameters applied to *Spitzer* data.

²Detrending parameters generated from AIJ (Collins et al. 2017).

³Detrending parameters generated from PEST pipeline (<http://pestobservatory.com/the-pest-pipeline>).

also configured to integrate the priors from Tables 6 & 7 and to invoke the `rejectflatmodel` option for all light curves with `NTEMPS = 8` to aid in faster convergence. After the first run, EXOFASTv2 generates the new `prior.2` file, which we then implement while repeating the process to achieve better convergence. For the second run, we integrate up to 20 000 steps while setting `NTHIN = 5`, the `rejectflatmodel` option was turned off, and the MIST SED file was omitted. After these runs were completed, EXOFASTv2 generated the posteriors, including the transit models (Figure 2 and Tables 9, 10, 11, & 12) and midpoint times (see Table 13). Of particular note are our eccentricity posteriors of $0.079^{+0.160}_{-0.058}$ for AU Mic b and $0.114^{+0.120}_{-0.074}$ for AU Mic c, which exclude moderate to high eccentricities. Additional analyses of the tran-

sits individually indicates that this posterior is most constrained by the *Spitzer* transits presented herein.

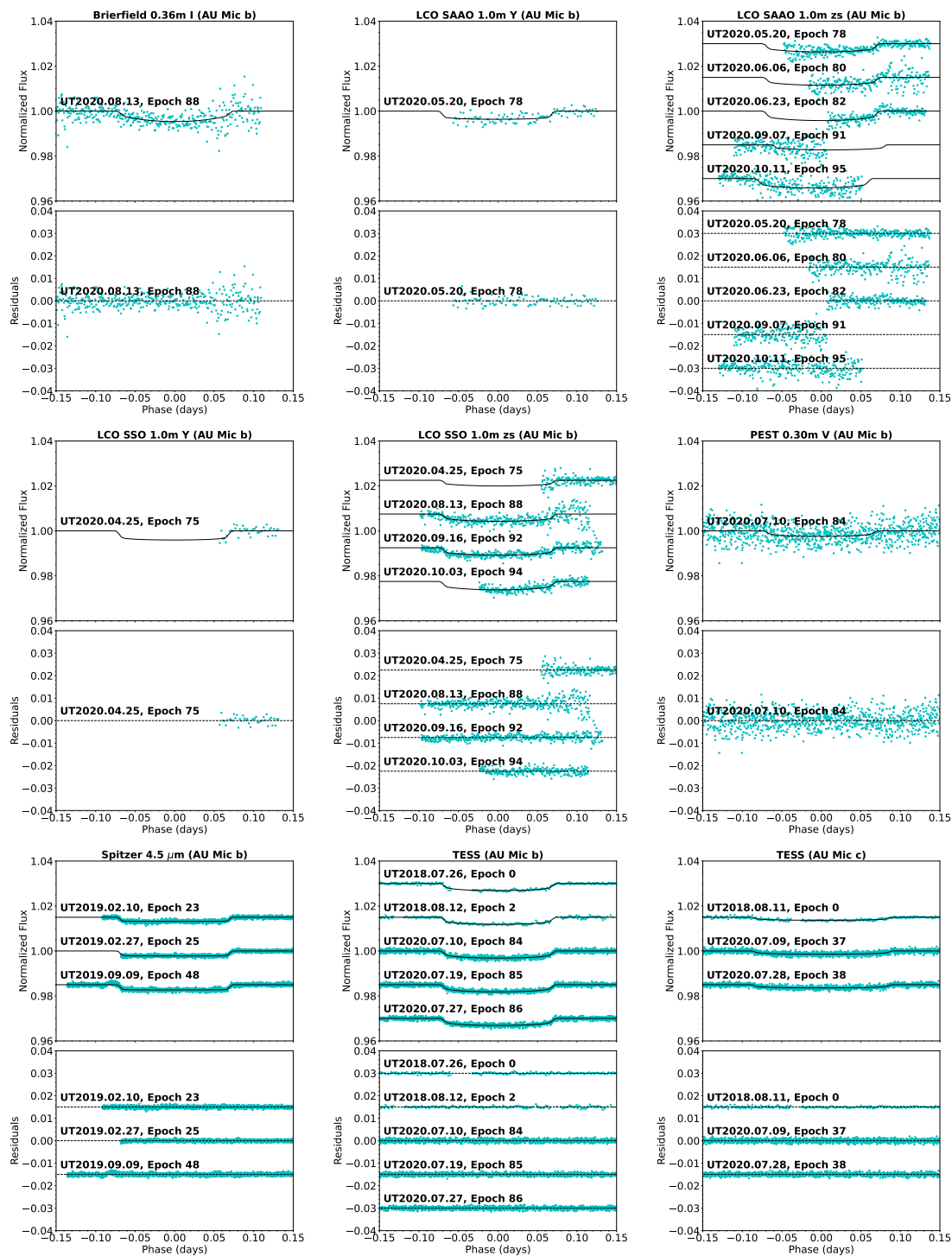


Figure 2. Two-panel plots of comparison between ground-based + *Spitzer* + *TESS* transits (cyan) and EXOFASTv2’s best-fit model (black) for AU Mic b & c. The modelings are in the upper panels, and the residuals are in the lower panels. Herein epoch refers to the number of transits since the first transit of either b or c. The *Brierfield* transit is obtained at epoch 88; *LCO SAAO* at 78, 80, 82, 91, & 95; *LCO SSO* at 75, 88, 92, & 94; *PEST* at 84; *Spitzer* at 23, 25, & 48; and *TESS* b at 0, 2, 84, 85, & 86, relative to the first *TESS* b transit. The *TESS* c transit is obtained at epoch 0, 37, & 38 relative to the first *TESS* c transit.

Table 9. EXOFASTv2-generated median values and 68% confidence interval for AU Mic system.

Posterior	Description	Unit	Quantity	
			AU Mic b	AU Mic c
M_*	Stellar Mass	M_\odot	$0.558^{+0.068}_{-0.090}$	
R_*	Stellar Radius	R_\odot	$0.749^{+0.030}_{-0.037}$	
L_*	Stellar Luminosity	L_\odot	$0.094^{+0.014}_{-0.015}$	
ρ_*	Stellar Density	g/cm^3	$1.89^{+0.24}_{-0.21}$	
$\log g$	Surface Gravity	...	$4.443^{+0.044}_{-0.048}$	
T_{eff}	Effective Temperature	K	3701^{+100}_{-98}	
[Fe/H]	Metallicity	...	$0.17^{+0.27}_{-0.37}$	
[Fe/H] ₀	Initial Metallicity ^a	...	$0.12^{+0.24}_{-0.36}$	
Age	...	Gyr	$0.0216^{+0.0034}_{-0.0031}$	
EEP	Equal Evolutionary Phase ^b	...	$164.9^{+5.4}_{-5.8}$	
P_{orb}	Orbital Period	days	$8.462993^{+0.000048}_{-0.000039}$	$18.859005^{+0.000084}_{-0.000072}$
M_{p}	Planetary Mass ^c	M_{J}	$0.058^{+0.021}_{-0.016}$	$0.0291^{+0.0110}_{-0.0080}$
R_{p}	Planetary Radius	R_{J}	$0.373^{+0.017}_{-0.021}$	$0.250^{+0.013}_{-0.015}$
T_{C}	Time of Conjunction ^d	BJD_TDB	$2458330.3916^{+0.0031}_{-0.0030}$	$2458342.2238^{+0.0026}_{-0.0023}$
T_{T}	Time of Minimum Projected Separation ^e	BJD_TDB	$2458330.3916^{+0.0031}_{-0.0030}$	$2458342.2238^{+0.0026}_{-0.0023}$
T_0	Optimal Conjunction Time ^f	BJD_TDB	$2458457.3365^{+0.0031}_{-0.0029}$	$2458455.3777^{+0.0027}_{-0.0022}$
a	Semi-Major Axis	au	$0.0669^{+0.0026}_{-0.0038}$	$0.1141^{+0.0044}_{-0.0065}$
e	Eccentricity	...	$0.079^{+0.160}_{-0.058}$	$0.114^{+0.120}_{-0.074}$
i	Inclination	deg	$89.72^{+0.22}_{-0.29}$	$89.39^{+0.47}_{-0.28}$
ω	Argument of Periastron	deg	-90 ± 100	-90 ± 100
T_{eq}	Equilibrium Temperature ^g	K	595^{+18}_{-21}	456^{+14}_{-16}
τ_{circ}	Tidal Circularization Timescale	Gyr	152^{+81}_{-55}	16400^{+9000}_{-7500}
K	RV Semi-Amplitude ^c	m/s	$8.6^{+3.2}_{-2.4}$	$3.33^{+1.30}_{-0.92}$
R_{p}/R_*	$0.05137^{+0.00099}_{-0.00120}$	$0.03429^{+0.00100}_{-0.00099}$
a/R_*	$19.28^{+0.79}_{-0.73}$	32.9 ± 1.3
δ	Transit Depth (R_{p}/R_*) ²	...	$0.00264^{+0.00010}_{-0.00012}$	$0.001176^{+0.000070}_{-0.000067}$
δ_{I}	Transit Depth in I	...	$0.00366^{+0.00130}_{-0.00072}$	$0.00152^{+0.00048}_{-0.00027}$
$\delta_{z'}$	Transit Depth in z'	...	$0.00409^{+0.00053}_{-0.00044}$	$0.00169^{+0.00020}_{-0.00018}$
$\delta_{4.5\mu\text{m}}$	Transit Depth in $4.5\mu\text{m}$...	$0.00265^{+0.00010}_{-0.00012}$	$0.001182^{+0.000069}_{-0.000068}$
δ_{TESS}	Transit Depth in TESS	...	$0.00339^{+0.00019}_{-0.00022}$	$0.001462^{+0.000077}_{-0.000093}$
δ_{V}	Transit Depth in V	...	$0.00341^{+0.00014}_{-0.00058}$	$0.00146^{+0.00051}_{-0.00024}$
δ_{y}	Transit Depth in y	...	$0.00357^{+0.00160}_{-0.00068}$	$0.00149^{+0.00057}_{-0.00025}$
τ	Ingress/Egress Transit Duration	days	$0.00721^{+0.00022}_{-0.00025}$	$0.00664^{+0.00180}_{-0.00084}$
T_{14}	Total Transit Duration	days	$0.14585^{+0.00031}_{-0.00036}$	$0.1773^{+0.0017}_{-0.0015}$
T_{FWHM}	FWHM Transit Duration	days	$0.13861^{+0.00020}_{-0.00023}$	$0.1703^{+0.0011}_{-0.0013}$
b	Transit Impact Parameter	...	$0.098^{+0.092}_{-0.065}$	$0.35^{+0.19}_{-0.26}$
b_{S}	Eclipse Impact Parameter	...	$0.093^{+0.091}_{-0.063}$	$0.346^{+0.095}_{-0.260}$
τ_{S}	Ingress/Egress Eclipse Duration	days	$0.00715^{+0.00059}_{-0.00070}$	$0.00647^{+0.00061}_{-0.00065}$
$T_{\text{S},14}$	Total Eclipse Duration	days	$0.145^{+0.011}_{-0.014}$	$0.173^{+0.020}_{-0.027}$
$T_{\text{S},\text{FWHM}}$	FWHM Eclipse Duration	days	$0.137^{+0.010}_{-0.014}$	$0.166^{+0.020}_{-0.026}$
$\delta_{\text{S},2.5\mu\text{m}}$	Blackbody Eclipse Depth at $2.5\mu\text{m}$	ppm	$0.63^{+0.18}_{-0.16}$	$0.0147^{+0.0060}_{-0.0051}$
$\delta_{\text{S},5.0\mu\text{m}}$	Blackbody Eclipse Depth at $5.0\mu\text{m}$	ppm	$24.9^{+3.3}_{-3.4}$	$2.55^{+0.48}_{-0.49}$
$\delta_{\text{S},7.5\mu\text{m}}$	Blackbody Eclipse Depth at $7.5\mu\text{m}$	ppm	$74.3^{+6.7}_{-7.4}$	$12.2^{+1.5}_{-1.7}$

Table 9 continued

Table 9 (continued)

Posterior	Description	Unit	Quantity	
			AU Mic b	AU Mic c
ρ_p	Planetary Density ^c	g/cm ³	1.42 ^{+0.60} _{-0.35}	2.28 ^{+0.94} _{-0.62}
$\log g_p$	Surface Gravity ^c	...	3.02 ^{+0.14} _{-0.12}	3.07 ^{+0.14} _{-0.11}
Θ	Safronov Number	...	0.0373 ^{+0.0140} _{-0.0097}	0.048 ^{+0.019} _{-0.013}
$\langle F \rangle$	Incident Flux	10 ⁹ $\frac{\text{erg}}{\text{s cm}^2}$	0.0282 ^{+0.0035} _{-0.0039}	0.0096 ± 0.0013
T_P	Time of Periastron	BJD-TDB	2458323.3 ^{+2.7} _{-3.0}	2458332.8 ^{+6.1} _{-6.2}
T_S	Time of Eclipse	BJD-TDB	2458334.62 ^{+0.54} _{-0.50}	2458332.8 ± 1.3
T_A	Time of Ascending Node	BJD-TDB	2458328.27 ^{+0.30} _{-0.48}	2458337.41 ^{+0.72} _{-1.20}
T_D	Time of Descending Node	BJD-TDB	2458332.51 ^{+0.50} _{-0.28}	2458347.03 ^{+1.20} _{-0.72}
V_c/V_e	h	...	1.000 ^{+0.045} _{-0.038}	1.009 ^{+0.140} _{-0.060}
$\sqrt{\left(1 - \frac{R_p}{R_\star}\right)^2 - b^2}$	Transit Chord	...	1.0466 ^{+0.0042} _{-0.0130}	0.974 ^{+0.050} _{-0.092}
sign	i	...	1.40 ^{+0.40} _{-0.33}	1.48 ^{+0.33} _{-0.34}
$\cos \omega$	-0.001 ^{+0.100} _{-0.093}	0.00 ^{+0.10} _{-0.11}
$\sin \omega$	-0.004 ^{+0.037} _{-0.054}	-0.015 ^{+0.060} _{-0.14}
$M_p \sin i$	Minimum Mass ^c	M _J	0.058 ^{+0.021} _{-0.016}	0.0291 ^{+0.0110} _{-0.0080}
M_p/M_\star	Mass Ratio ^c	...	0.000099 ^{+0.000039} _{-0.000028}	0.000050 ^{+0.000021} _{-0.000014}
d/R_\star	Separation at Mid Transit	...	19.2 ^{+1.6} _{-1.5}	33.1 ^{+4.2} _{-2.7}
P_T	A Priori Non-grazing Transit Probability	...	0.0495 ^{+0.0043} _{-0.0038}	0.0291 ^{+0.0026} _{-0.0033}
$P_{T,G}$	A Priori Transit Probability	...	0.0548 ^{+0.0047} _{-0.0041}	0.0312 ^{+0.0028} _{-0.0035}
P_S	A Priori Non-grazing Eclipse Probability	...	0.04958 ^{+0.00210} _{-0.00067}	0.0299 ^{+0.0038} _{-0.0020}
$P_{S,G}$	A Priori Eclipse Probability	...	0.05492 ^{+0.00240} _{-0.00073}	0.0320 ^{+0.0042} _{-0.0021}
$u_{1,I}$	Linear Limb-darkening Coefficient in I	0.57 ^{+0.39} _{-0.36}
$u_{1,z'}$	Linear Limb-darkening Coefficient in z'	0.72 ^{+0.13} _{-0.14}
$u_{1,4.5\mu\text{m}}$	Linear Limb-darkening Coefficient in 4.5 μm	0.0086 ^{+0.0130} _{-0.0065}
$u_{1,TESS}$	Linear Limb-darkening Coefficient in TESS	0.453 ^{+0.059} _{-0.064}
$u_{1,V}$	Linear Limb-darkening Coefficient in V	0.47 ^{+0.45} _{-0.33}
$u_{1,y}$	Linear Limb-darkening Coefficient in y	0.54 ^{+0.45} _{-0.36}
$u_{2,I}$	Quadratic Limb-darkening Coefficient in I	0.01 ^{+0.42} _{-0.33}
$u_{2,z'}$	Quadratic Limb-darkening Coefficient in z'	-0.28 ^{+0.17} _{-0.10}
$u_{2,4.5\mu\text{m}}$	Quadratic Limb-darkening Coefficient in 4.5 μm	0.140 ^{+0.037} _{-0.038}
$u_{2,TESS}$	Quadratic Limb-darkening Coefficient in TESS	0.207 ^{+0.100} _{-0.097}
$u_{2,V}$	Quadratic Limb-darkening Coefficient in V	0.09 ^{+0.45} _{-0.37}
$u_{2,y}$	Quadratic Limb-darkening Coefficient in y	0.02 ^{+0.40} _{-0.34}

Table 9 continued

Table 9 (*continued*)

Posterior	Description	Unit	Quantity	
			AU Mic b	AU Mic c

NOTE—See Table 3 in [Eastman et al. \(2019\)](#) for a detailed description of all parameters. Since both Pan-STARRS Y and Pan-STARRS z_s are not available among the filters in EXOFASTv2, y and z' (Sloan z) were used as respective approximate substitutes. Additionally, the Claret & Bloemen limb darkening tables ([Claret & Bloemen 2011](#)) default option has been disabled since AU Mic is a low-mass red dwarf.

^aThe metallicity of the star at birth.

^bCorresponds to static points in a star's evolutionary history. See §2 in [Dotter \(2016\)](#).

^cUses measured radius and estimated mass from [Chen & Kipping \(2017\)](#).

^dTime of Conjunction is commonly reported as the “transit time”.

^eTime of Minimum Projected Separation is a more correct “transit time”.

^fOptimal Time of Conjunction minimizes the covariance between T_C and Period.

^gAssumes no albedo and perfect redistribution.

^hThe velocity at T_C of an assumed circular orbit divided by the velocity of the modeled eccentric orbit.

ⁱThe sign of the solution to the quadratic mapping from V_c/V_e to e.

Table 10. EXOFASTv2-generated median values and 68% confidence interval for follow-up observations of AU Mic transits (Part I).

Planet	Telescope	Date (UT)	Filter	σ^2 (Added Variance)	TTV a (days)	T δ V b	F $_0$ C
b	TESS	2018-07-26	TESS	0.0000000019 ^{+0.0000000100} -0.0000000088	-0.0024 ^{+0.0028} -0.0031	-0.0006 ^{+0.0013} -0.0012	1.000002 ^{+0.000024} -0.000023
c	TESS	2018-08-11	TESS	0.0000000030 \pm 0.0000000097	-0.0005 ^{+0.0020} -0.0026	-0.0006 ^{+0.0080} -0.00074	0.999994 ^{+0.000026} -0.000027
b	TESS	2018-08-12	TESS	0.0000000055 ^{+0.0000000016} -0.0000000013	-0.0006 ^{+0.0029} -0.0030	-0.0006 ^{+0.0014} -0.0012	0.999999 \pm 0.000030
b	Spitzer	2019-02-10	4.5 μ m	0.0000000600 ^{+0.0000000050} -0.0000000047	0.0039 \pm 0.0030	-0.0053 ^{+0.00130} -0.00100	1.000075 \pm 0.000022
b	Spitzer	2019-02-27	4.5 μ m	0.0000000374 ^{+0.0000000040} -0.0000000036	0.0049 ^{+0.0029} -0.0031	-0.0055 ^{+0.0015} -0.0012	1.000220 ^{+0.000019} -0.000017
b	Spitzer	2019-09-09	4.5 μ m	0.0000000933 ^{+0.0000000042} -0.0000000037	0.0020 ^{+0.0032} -0.0035	-0.0039 ^{+0.0014} -0.0011	0.999893 ^{+0.000013} -0.000014
b	LCO SSO	2020-04-25	z'	0.000000234 ^{+0.0000000029} -0.0000000028	-0.0028 ^{+0.0040} -0.0048	-0.0054 ^{+0.0047} -0.0014	1.000000 ^{+0.000013} -0.000014
b	LCO SSO	2020-04-25	y	0.000000104 ^{+0.000000100} -0.0000000067	-0.0037 ^{+0.0048} -0.0059	0.0037 ^{+0.0046} -0.0076	0.99964 ^{+0.00031} -0.00038
b	LCO SAAO	2020-05-20	z'	0.000000188 \pm 0.000000018	-0.0019 ^{+0.0044} -0.0049	0.0005 ^{+0.0025} -0.0027	1.000034 \pm 0.00018
b	LCO SAAO	2020-05-20	y	0.00000140 ^{+0.0000000060} -0.0000000047	0.0084 ^{+0.0057} -0.0066	0.0000 ^{+0.0047} -0.0052	0.99993 ^{+0.00044} -0.00039
b	LCO SAAO	2020-06-06	z'	0.00000677 ^{+0.0000000081} -0.0000000066	-0.0053 ^{+0.0050} -0.0056	-0.0018 ^{+0.0053} -0.0050	1.00005 ^{+0.00041} -0.00034
b	LCO SAAO	2020-06-23	z'	0.00000185 ^{+0.0000000025} -0.0000000021	0.0003 ^{+0.0040} -0.0049	0.0079 ^{+0.0016} -0.0031	0.99987 ^{+0.00018} -0.00021
c	TESS	2020-07-09	TESS	0.0000000001 \pm 0.0000000015	-0.0024 ^{+0.0031} -0.0047	0.0023 ^{+0.00100} -0.0063	1.000001 ^{+0.000020} -0.000021
b	TESS	2020-07-10	TESS	0.0000000002 ^{+0.0000000012} -0.0000000011	-0.0018 ^{+0.0038} -0.0047	-0.0006 ^{+0.0013} -0.0011	0.999999 ^{+0.000015} -0.000018
b	PEST	2020-07-10	V	0.00000600 ^{+0.0000000074} -0.0000000076	-0.0038 \pm 0.0061	-0.0081 ^{+0.0029} -0.0014	0.99817 ^{+0.00018} -0.00015
b	TESS	2020-07-19	TESS	0.0000000015 ^{+0.00000000100} -0.0000000099	-0.0009 ^{+0.0036} -0.0050	-0.0006 ^{+0.0013} -0.0011	1.000000 \pm 0.000015
b	TESS	2020-07-27	TESS	0.0000000011 \pm 0.0000000097	0.0002 ^{+0.0037} -0.0050	-0.0007 ^{+0.0013} -0.0011	0.999999 \pm 0.000015
c	TESS	2020-07-28	TESS	0.0000000001 ^{+0.0000000013} -0.0000000012	0.0001 ^{+0.0032} -0.0039	0.0022 ^{+0.00097} -0.0058	1.000001 ^{+0.000017} -0.000019
b	Brierfield	2020-08-13	I	0.0000117 ^{+0.00000010} -0.00000010	0.0085 ^{+0.0047} -0.0055	0.0070 ^{+0.0022} -0.0036	0.99935 ^{+0.00025} -0.00028
b	LCO SSO	2020-08-13	z'	0.00000406 ^{+0.0000000039} -0.0000000037	-0.0018 ^{+0.0044} -0.0062	-0.0013 ^{+0.0034} -0.0036	1.00009 ^{+0.00030} -0.00026
b	LCO SAAO	2020-09-07	z'	0.00000688 ^{+0.0000000083} -0.0000000070	0.0064 ^{+0.0092} -0.0068	-0.0057 ^{+0.0042} -0.0030	0.99988 ^{+0.00045} -0.00035
b	LCO SSO	2020-09-16	z'	0.00000131 ^{+0.0000000013} -0.0000000011	-0.0020 ^{+0.0041} -0.0054	0.0000 ^{+0.0021} -0.0023	0.99996 \pm 0.00013
b	LCO SSO	2020-10-03	z'	0.00000125 ^{+0.0000000017} -0.0000000014	0.0011 ^{+0.0041} -0.0056	0.0020 ^{+0.0022} -0.0024	1.00216 ^{+0.00017} -0.00016
b	LCO SAAO	2020-10-11	z'	0.00000651 ^{+0.0000000069} -0.0000000058	0.0100 ^{+0.0070} -0.0074	0.0039 ^{+0.0030} -0.0033	1.000099 ^{+0.00048} -0.00049

NOTE—See Table 3 in Eastman et al. (2019) for a detailed description of all parameters. Since both Pan-STARRS Y and Pan-STARRS z_s are not available among the filters in EXOFASTv2, y and z' (Sloan z) were used as respective approximate substitutes.

^a Transit Timing Variation

^b Transit Depth Variation

^c Baseline Flux

Table 11. EXOFASTv2-generated median values and 68% confidence interval for follow-up observations of AU Mic b (Part II).

Planet	Telescope	Date (UT)	Filter	C_0^a	C_1^a	M_0^b	M_1^b	M_2^b
b	TESS	2018-07-26	TESS
c	TESS	2018-08-11	TESS
b	TESS	2018-08-12	TESS
b	Spitzer	2019-02-10	4.5 μm	$-0.000165^{+0.000043}_{-0.000041}$...	$-0.00110^{+0.00034}_{-0.00033}$	-0.0112 ± 0.0010	0.0108 ± 0.0010
b	Spitzer	2019-02-27	4.5 μm	$-0.000247^{+0.000044}_{-0.000042}$	$0.000048^{+0.000041}_{-0.000032}$	$0.00070^{+0.00033}_{-0.00037}$	$0.00037^{+0.00037}_{-0.00041}$	$-0.00303^{+0.00081}_{-0.00076}$
b	Spitzer	2019-09-09	4.5 μm	$-0.000576^{+0.000093}_{-0.000110}$...	-0.00030 ± 0.00016	$0.00194^{+0.00020}_{-0.00021}$	$-0.00022^{+0.00061}_{-0.00063}$
b	LCO SSO	2020-04-25	z'	$0.00000^{+0.00024}_{-0.00026}$
b	LCO SSO	2020-04-25	y	$-0.00111^{+0.00074}_{-0.00079}$
b	LCO SAAO	2020-05-20	z'	0.00102 ± 0.00035
b	LCO SAAO	2020-05-20	y	$-0.00007^{+0.00071}_{-0.00070}$
b	LCO SAAO	2020-06-06	z'	$0.00025^{+0.00081}_{-0.00074}$
b	LCO SAAO	2020-06-23	z'	$-0.00021^{+0.00038}_{-0.00049}$
c	TESS	2020-07-09	TESS
b	TESS	2020-07-10	TESS
b	PEST	2020-07-10	V	$-0.0037^{+0.00050}_{-0.00049}$...	0.1038 ± 0.0040	-0.1074 ± 0.0043	$-0.0002^{+0.00017}_{-0.00016}$
b	TESS	2020-07-19	TESS
b	TESS	2020-07-27	TESS
c	TESS	2020-07-28	TESS
b	Brierfield	2020-08-13	I	-0.0038 ± 0.0052	$-0.0026^{+0.0045}_{-0.0047}$	$-0.0009^{+0.00022}_{-0.00023}$
b	LCO SSO	2020-08-13	z'	$-0.00002^{+0.00043}_{-0.00052}$	$0.00028^{+0.00029}_{-0.00033}$...
b	LCO SAAO	2020-09-07	z'	$-0.000020^{+0.00063}_{-0.00066}$...	-0.00035 ± 0.00096
b	LCO SSO	2020-09-16	z'	$0.00014^{+0.00033}_{-0.00029}$
b	LCO SSO	2020-10-03	z'	-0.00179 ± 0.00028
b	LCO SAAO	2020-10-11	z'	-0.0014 ± 0.0016

NOTE—See Table 3 in Eastman et al. (2019) for a detailed description of all parameters. Since both Pan-STARRS Y and Pan-STARRS z_s are not available among the filters in EXOFASTv2, y and z' (Sloan z) were used as respective approximate substitutes. Also see §2 of this paper for details on detrending parameters used for each observation; the flare (Spitzer), sky (Spitzer & PEST), sky/Pixel_T1 (LCO SAAO) were set as additive while the remaining detrending parameters were set as multiplicative.

^a Additive Detrending Coefficient

^b Multiplicative Detrending Coefficient

Table 12. EXOFASTv2-generated median values and 68% confidence interval for follow-up observations of AU Mic b (Part III).

Planet	Telescope	Date (UT)	Filter	$M_3 \hat{a}$	$M_4 \hat{a}$	$M_5 \hat{a}$	$M_6 \hat{a}$	$M_7 \hat{a}$
b	TESS	2018-07-26	TESS
c	TESS	2018-08-11	TESS
b	TESS	2018-08-12	TESS
b	Spitzer	2019-02-10	4.5 μm	$-0.00623^{+0.00075}_{-0.00074}$	0.00496 ± 0.00048	$-0.000407^{+0.000041}_{-0.000042}$	$-0.000270^{+0.000057}_{-0.000053}$...
b	Spitzer	2019-02-27	4.5 μm	$0.00326^{+0.00073}_{-0.00080}$	$0.00118^{+0.00065}_{-0.00060}$	$0.000873^{+0.000095}_{-0.000110}$	$-0.00088^{+0.00015}_{-0.00013}$...
b	Spitzer	2019-09-09	4.5 μm	0.00049 ± 0.00056	$-0.00174^{+0.00046}_{-0.00045}$	$-0.000003^{+0.000044}_{-0.000046}$	$-0.000403^{+0.000061}_{-0.000057}$	$-0.0000519^{+0.000059}_{-0.000058}$
b	LCO SSO	2020-04-25	z'
b	LCO SSO	2020-04-25	y
b	LCO SAAO	2020-05-20	z'
b	LCO SAAO	2020-05-20	y
b	LCO SAAO	2020-06-06	z'
b	LCO SAAO	2020-06-23	z'
c	TESS	2020-07-09	TESS
b	TESS	2020-07-10	TESS
b	PEST	2020-07-10	V	$0.00004^{+0.0012}_{-0.0014}$	$-0.0023^{+0.0028}_{-0.0026}$	0.0013 ± 0.0011	$-0.00284^{+0.00088}_{-0.00087}$...
b	TESS	2020-07-19	TESS
b	TESS	2020-07-27	TESS
c	TESS	2020-07-28	TESS
b	Brierfield	2020-08-13	I	$-0.0009^{+0.0015}_{-0.0014}$
b	LCO SSO	2020-08-13	z'
b	LCO SAAO	2020-09-07	z'
b	LCO SSO	2020-09-16	z'
b	LCO SSO	2020-10-03	z'
b	LCO SAAO	2020-10-11	z'

NOTE—See Table 3 in Eastman et al. (2019) for a detailed description of all parameters. Since both Pan-STARRS Y and Pan-STARRS z_s are not available among the filters in EXOFASTv2, y and z' (Sloan z) were used as respective approximate substitutes. Also see §2 of this paper for details on detrending parameters used for each observation; the flare (Spitzer) & PEST, sky (Spitzer & PEST), sky/Pixel_T1 (LCO SAAO) were set as additive while the remaining detrending parameters were set as multiplicative.

^aMultiplicative Detrending Coefficient

4. TTV ANALYSIS

In this section, we present our O–C diagram and TTV dynamical modeling with *Exo-Striker*, considering both a two-planet model and an example three-planet model to account for the observed TTVs.

4.1. O–C Diagram

We calculate the expected midpoint times using AU Mic b’s period and T_C from [Gilbert et al. \(2021\)](#); the period and T_C from [Martoli et al. \(2021\)](#) yield similar results. Using the measured and expected midpoint times, we construct the O–C diagram in [Figure 3](#). We make use of the combined transit midpoint times ([Table 13](#)), now extracted from all light curves and R-M observations through the processes described in the previous §2 for data from [Gilbert et al. \(2021\)](#) and the R-M observations, and from our own analysis in §3. With a $\chi^2 \gg 1$, it is readily apparent by eye that the precise *Spitzer* transit times are significantly deviant from those expected from a linear ephemeris from the *TESS* transit times alone. Note, the *Spitzer* transit times are in BJD and corrected for the relative light-time travel delay between *Spitzer* and the Solar System barycenter. Additionally, the ground-based R-M transit midpoints are similarly late and consistent with the *Spitzer* transit times. The ground-based photometric transits show large scatter and correspondingly larger timing uncertainties relative to the space-based transit midpoint times.

4.2. TTV *Exo-Striker* Dynamical Modeling

Motivated by the apparent TTV variability deviating from a linear ephemeris in §4.1, we utilize the *Exo-Striker* package ([Trifonov 2019](#)) to model the variation in transit timings of AU Mic b and c. Like *EXOFASTv2*, *Exo-Striker* utilizes a Markov chain Monte

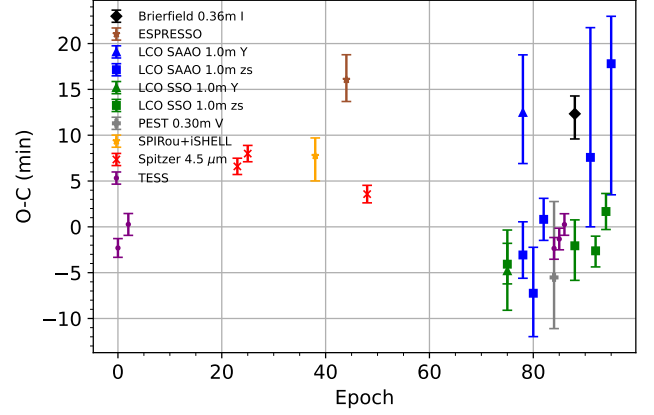


Figure 3. O–C Diagram of AU Mic b, using the *EXOFASTv2*-generated measured midpoint times and the calculated expected midpoint times for all 23 AU Mic b transit data sets from [Table 3](#). AU Mic b’s period and T_C from [Gilbert et al. \(2021\)](#) were used for the calculation of expected midpoint times.

Carlo (MCMC) to assess the statistical significance of the measured TTVs and the confidence in the dynamical model posteriors that can be inferred from the TTVs. Additionally, we incorporate the stellar priors from [Table 14](#) and the planet priors from [Table 15](#).

We configured *Exo-Striker* to use the *Simplex* and *Dynamical* algorithms during both the model fitting and MCMC runs; the justification for using *Dynamical* instead of *Keplerian* is that the *Keplerian* algorithm does not work as well in a compact system with orbital resonances ([Fabrycky 2010](#)) like AU Mic. The dynamical model time steps has been set to the lowest possible 0.01 day given the short orbital periods of both planets. To find the best-fit TTV model, we employ *Exo-Striker*’s built-in *scipy* minimizer algorithms; we use truncated Newton algorithm (TNC)¹⁹ as a primary min-

¹⁹ <https://docs.scipy.org/doc/scipy/reference/optimize.minimize-tnc.html>

Table 13. AU Mic planets’ midpoint time priors for **Exo-Striker** models.

Planet	Telescope	Transit N	Date (UT)	Band	T_0 (BJD)
b	<i>TESS</i>	1	2018-07-26	TESS	$2458330.38920 \pm 0.00041$
	<i>TESS</i>	3	2018-08-12	TESS	$2458347.31699 \pm 0.00060$
	<i>Spitzer</i>	24	2019-02-10	$4.5 \mu\text{m}$	$2458525.04439 \pm 0.00017$
	<i>Spitzer</i>	26	2019-02-27	$4.5 \mu\text{m}$	$2458541.97136 \pm 0.00016$
	<i>SPIRou + iSHELL</i>	39	2019-06-17	(a)	$2458651.99020 \pm 0.00180$
	<i>ESPRESSO</i>	45	2019-08-07	378.2-788.7 nm	$2458702.77397 \pm 0.00178$
	<i>Spitzer</i>	49	2019-09-09	$4.5 \mu\text{m}$	$2458736.61730 \pm 0.00015$
	<i>LCO SSO</i>	76	2020-04-25	Pan-STARRS Y	$2458965.11250 \pm 0.00300$
	<i>LCO SSO</i>	76	2020-04-25	Pan-STARRS z_s	$2458965.11300 \pm 0.00140$
	<i>LCO SAAO</i>	79	2020-05-20	Pan-STARRS z_s	$2458990.50270 \pm 0.00240$
	<i>LCO SAAO</i>	79	2020-05-20	Pan-STARRS Y	$2458990.51350 \pm 0.00430$
	<i>LCO SAAO</i>	81	2020-06-06	Pan-STARRS z_s	$2459007.42580 \pm 0.00340$
	<i>LCO SAAO</i>	83	2020-06-23	Pan-STARRS z_s	$2459024.35740 \pm 0.00140$
	<i>PEST</i>	85	2020-07-10	V	$2459041.27900 \pm 0.00570$
	<i>TESS</i>	85	2020-07-10	TESS	$2459041.28120 \pm 0.00030$
	<i>TESS</i>	86	2020-07-19	TESS	$2459049.74491 \pm 0.00028$
	<i>TESS</i>	87	2020-07-27	TESS	$2459058.20901 \pm 0.00026$
	<i>LCO SSO</i>	89	2020-08-13	Pan-STARRS z_s	$2459075.13340 \pm 0.00250$
	<i>Brierfield</i>	89	2020-08-13	I	$2459075.14340 \pm 0.00240$
	<i>LCO SAAO</i>	92	2020-09-07	Pan-STARRS z_s	$2459100.52910 \pm 0.00980$
<i>LCO SSO</i>	93	2020-09-16	Pan-STARRS z_s	$2459108.98502 \pm 0.00092$	
<i>LCO SSO</i>	95	2020-10-03	Pan-STARRS z_s	$2459125.91400 \pm 0.00110$	
<i>LCO SAAO</i>	96	2020-10-11	Pan-STARRS z_s	$2459134.38820 \pm 0.00990$	
c	<i>TESS</i>	1	2018-08-11	TESS	$2458342.22330 \pm 0.00110$
	<i>TESS</i>	38	2020-07-09	TESS	$2459040.00432 \pm 0.00082$
	<i>TESS</i>	39	2020-07-28	TESS	$2459058.86603 \pm 0.00072$

NOTE—(a) 955-2515 nm (*SPIRou*) and 2.18-2.47 nm (*iSHELL*)

Table 14. AU Mic’s stellar priors for **Exo-Striker** best-fit and MCMC modeling.

Prior	Unit	AU Mic
Mass	M_\odot	$\mathcal{N}(0.50, 0.03)$
Radius	R_\odot	$\mathcal{N}(0.75, 0.03)$
Luminosity	L_\odot	$\mathcal{N}(0.0900, 0.0001)$
T_{eff}	K	$\mathcal{N}(3700, 100)$
$v \sin i$	km/s	$\mathcal{N}(8.7, 0.2)$

NOTE—These priors are taken from [Plavchan et al. \(2020\)](#).

imizer and Nelder-Mead algorithm²⁰ as a secondary minimizer, with both set at one con-

secutive integration and 5 000 integration steps; the rest of the configurations for those minimizers were left to default settings. After we find a best-fit model, we compute an MCMC with 50 000 burn-ins, 200 000 integration steps, and 4 walkers; the other settings for MCMC were left to defaults, including adopting 68.300% confidence intervals for estimating one- σ posterior uncertainties. These best-fit and MCMC configurations apply to both the 2-planet and 3-planet dynamical models presented herein.

We first explore the 2-planet scenario (AU Mic b and c). Then, we explore a representative 3-planet scenario. The following sub-subsections detail the process in exploring these cases.

4.2.1. 2-Planet Dynamical Modeling

²⁰ <https://docs.scipy.org/doc/scipy/reference/optimize.minimize-neldermead.html>

Table 15. AU Mic’s planetary priors for **Exo-Striker** best-fit and MCMC modeling.

Prior	Unit	AU Mic b	AU Mic c	AU Mic d ^a
K	m/s	$\mathcal{N}(8.5, 2.3)$	$\mathcal{U}(0.8, 9.5)$	$\mathcal{U}(0.0, 10000.0)$
P _{orb}	day	$\mathcal{N}(8.463, 0.001)$	$\mathcal{N}(18.859, 0.001)$	$\mathcal{N}(12.742, 0.020)$
e	...	$\mathcal{U}(0.00000, 0.58038)$	$\mathcal{U}(0.00000, 0.37308)$	$\mathcal{U}(0.000, 0.999)$
ω	deg	$\mathcal{U}(0.0, 360.0)$	$\mathcal{U}(0.0, 360.0)$	$\mathcal{U}(0.0, 360.0)$
M ₀	deg	$\mathcal{U}(0.0, 360.0)$	$\mathcal{U}(0.0, 360.0)$	$\mathcal{U}(0.0, 360.0)$
i	deg	$\mathcal{N}(89.5, 0.3)$	$\mathcal{N}(89.0, 0.5)$	$\mathcal{U}(0.0, 180.0)$
Ω	deg	$\mathcal{U}(0.0, 360.0)$	$\mathcal{U}(0.0, 360.0)$	$\mathcal{U}(0.0, 360.0)$

NOTE—M₀ ≡ mean anomaly, and Ω ≡ longitude of ascending node.

(a) For 3-planet model only.

We explored a best-fit scenario for a 2-planet model with **Exo-Striker**. The eccentricity posteriors from the EXOFASTv2 analysis (Table 9) provided us $\sim 4.056\sigma$ upper limits on both planets’ eccentricity. Analysis of the transit light curves themselves exclude such high eccentricities as in Gilbert et al. (2021) and Plavchan et al. (2020), but we are only modeling the transit midpoint times herein. We also explored a best-fit scenario for a “mass-less” no-TTV 2-planet model with **Exo-Striker**, as a control on testing for the presence and statistical significance of TTVs.

4.2.2. 3-Planet Dynamical Modeling

Cale et al. (2021) explores the analysis of RVs of AU Mic, and searches for additional candidate non-transiting planet signals. In particular, Cale et al. (2021) identifies a candidate RV signal in-between the orbits of AU Mic b and c with an orbital period of 12.742 days, which to date is unconfirmed, which we call a hypothetical “d” planet. This “middle-d” non-transiting planet scenario, if confirmed, would establish the AU Mic planetary system in a 4:6:9 orbital resonant chain. This would not be the first known non-transiting planet to exist between two transiting planets; Christiansen et al. (2017), Buchhave et al. (2016), Sun et al. (2019), and Osborn et al. (2021) identified similar exoplanet configurations for the HD 3167,

Kepler-20, Kepler-411, and TOI-431 planetary systems respectively. Similarly to the 2-planet model, we imposed 4σ upper limits on planets b’s and c’s eccentricity for this paper.

4.3. TTV Results

Here we present the results of both the no-TTV, 2-planet and 3-planet TTV modeling using the **Exo-Striker** package. We also calculate the mass of AU Mic c using the generated posteriors from **Exo-Striker**.

4.3.1. Results on Exo-Striker 2-Planet Modeling

The best-fit O–C diagram (Figure 4), posteriors (Table 16), and MCMC corner plot (Figure A1) showcase the best possible 2-planet model. The **Exo-Striker**’s Angular Momentum Deficit (AMD, Laskar 1997, 2000; Laskar & Petit 2017) criteria indicated that the 2-planet model is stable. However, it is clear from Figure 4 that the model does not converge very well with the data points, especially with *TESS* and *Spitzer*. This implies that we potentially need a third planet to account for the observed TTV variability. This interpretation is one of several hypotheses that are being explored and which are discussed in greater details in §6. For our control no-TTV scenario of “mass-less” planets b and c, we present the best fit O–C diagram (Figure 5),

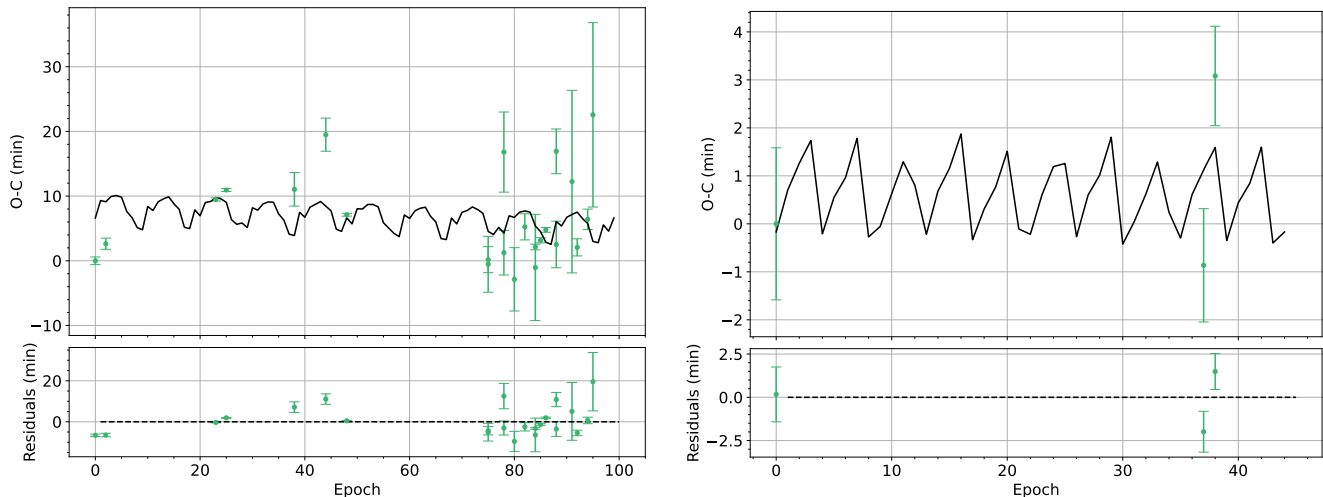


Figure 4. 2-planet O–C diagram of AU Mic b (left) and AU Mic c (right), with comparison between TTVs (green) and *Exo-Striker*-generated best-fit models (black).

Table 16. *Exo-Striker*-generated parameters for AU Mic 2-planet best-fit and MCMC modeling.

Parameter	Unit	Best-fit		MCMC	
		AU Mic b	AU Mic c	AU Mic b	AU Mic c
K	m/s	4.03906	9.49903	4.10830 ± 1.47951	9.31429 ± 0.27661
P_{orb}	day	8.46255	18.86109	8.46257 ± 0.00003	18.86112 ± 0.00076
e	...	0.00000	0.08329	0.00089 ± 0.00065	0.08220 ± 0.00473
ω	deg	89.79621	216.71379	61.89388 ± 36.98216	215.56678 ± 1.90214
M_0	deg	0.00000	0.00032	27.96061 ± 20.80132	1.12536 ± 0.80464
i	deg	89.50262	88.99146	89.51412 ± 0.31257	88.95986 ± 0.51613
Ω	deg	0.00000	0.00006	185.70005 ± 116.59810	184.90569 ± 116.58777
$-\ln \mathcal{L}$...	-61.93923		-74.96317	
χ^2	...	428		455	
χ_{red}^2	...	36		38	
$\Delta AICc$...	-57.69664		-83.74452	

posteriors (Table 17), and corner plot (Figure A2).

4.3.2. Results on *Exo-Striker* 3-Planet Modeling

Since the 2-planet circular orbit model does not adequately reproduce the observed TTVs as evidenced in Figure 4, we explored a *representative* and non-exhaustive hypothetical 3-planet scenario. We find a best-fit and MCMC model for this representative 3-planet scenario that adequately accounts for the *TESS* and *Spitzer*

TTVs and is also consistent with the RV candidate signal in [Cale et al. \(2021\)](#), presented in Table 18 and Figures 6 & A3. Moreover, the 3-planet case’s log likelihood, χ^2 , and reduced- χ^2 are better than those of the 2-planet case, the latter of which are better than the no-TTV “mass-less” scenario. The delta log-likelihoods and corresponding $\Delta AICc$ indicate that the 3-planet scenario is strongly favored and the two planet scenario and the no-TTV scenario are statistically excluded. *Exo-Striker* indicates that this three-planet solution fails the AMD

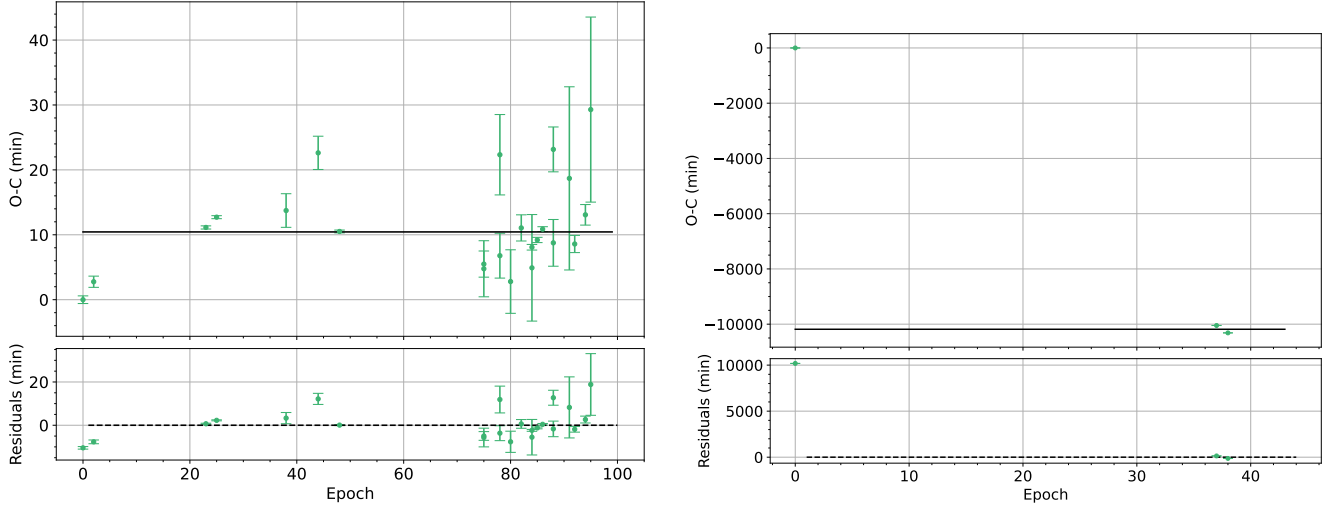


Figure 5. Mass-less planets O–C diagram of AU Mic b (left) and AU Mic c (right), with comparison between TTVs (green) and Exo-Striker-generated best-fit models (black).

Table 17. Exo-Striker-generated parameters for AU Mic mass-less planets best-fit and MCMC modeling.

Parameter	Unit	Best-fit		MCMC	
		AU Mic b	AU Mic c	AU Mic b	AU Mic c
K	m/s	0.00000	0.00000	0.00000 ± 0.00000	0.00000 ± 0.00000
P_{orb}	day	8.46293	19.04753	8.46293 ± 0.00000	18.98613 ± 0.00002
e	...	0.00004	0.00001	0.47442 ± 0.09381	0.37308 ± 0.00000
ω	deg	223.78788	0.00007	230.38681 ± 18.24298	0.00000 ± 0.00000
M_0	deg	225.89190	0.00010	193.13783 ± 7.76425	0.00000 ± 0.00000
i	deg	90.73560	88.59738	89.47176 ± 0.29016	69.69803 ± 0.00001
Ω	deg	0.00002	0.00000	189.38073 ± 126.18823	180.59530 ± 125.12807
$-\ln \mathcal{L}$...	-20683716.47978		-6083619013.93697	
χ^2	...	41367738		12167264028	
χ_{red}^2	...	2954838		869090288	
ΔAIC_c	...	-41367384.95956		-12167237979.87394	

criterion. However, given the 4:6:9 orbital period commensurability for b, d, and c, respectively, we investigate the dynamical stability of this system configuration with two N-body codes, the latter of which is used for a consistency check. We generate simulations with `rebound` (Rein & Liu 2012; Rein & Spiegel 2015) and `mercury6` (Chambers 1999) to test the stability of this representative 3-planet system; both indicate that this 3-planet configuration is stable (see §6 for more detailed discussions).

4.3.3. The Mass of AU Mic c

We use equation (1) from Cumming et al. (1999) and the best-fit parameters & MCMC uncertainties from Tables 16 and 18 to calculate the mass of AU Mic c. To simplify the equation, we made an assumption that $M_{\star} \gg M_p$. For the best-fit 2-planet scenario, our calculation yields the mass of c to be 0.0781 ± 0.0039

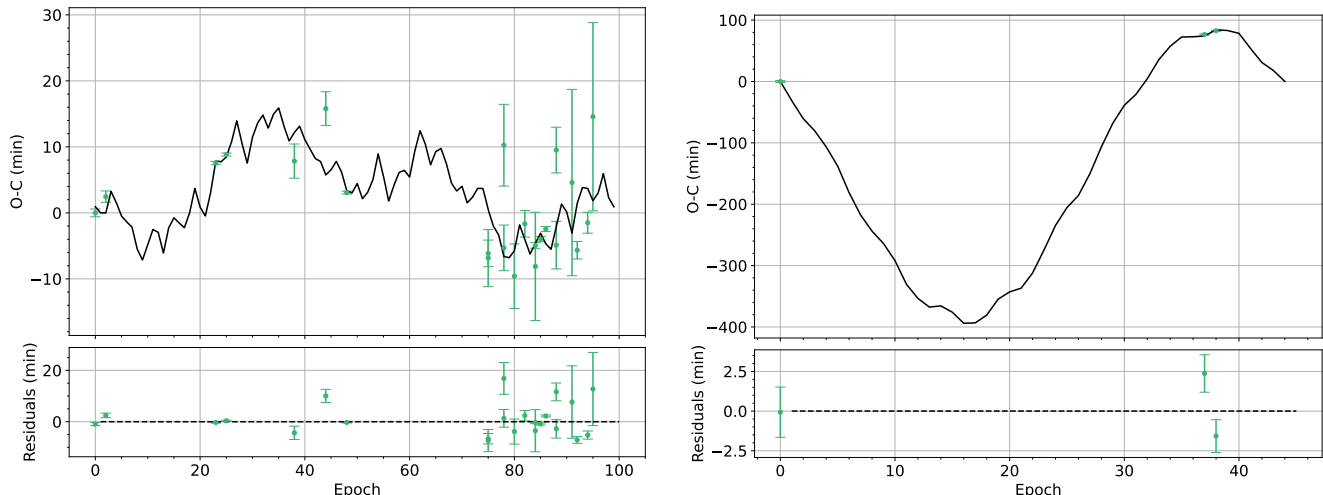


Figure 6. 3-planet O-C diagram of AU Mic b (left) and AU Mic c (right), with comparison between TTVs (green) and Exo-Striker-generated best-fit models (black).

Table 18. Exo-Striker-generated parameters for AU Mic 3-planet best-fit and MCMC modeling.

Parameter	Unit	Best-fit			MCMC		
		AU Mic b	AU Mic c	AU Mic d	AU Mic b	AU Mic c	AU Mic d
K	m/s	17.40198	7.65369	5.07363	1.91815 ± 1.27252	9.21910 ± 0.50712	1.06232 ± 0.30432
P_{orb}	day	8.46340	18.85872	13.48517	8.46329 ± 0.00027	18.86224 ± 0.00126	13.46591 ± 0.01022
e	...	0.02348	0.00000	0.00000	0.07436 ± 0.00994	0.02508 ± 0.01531	0.00998 ± 0.00752
ω	deg	89.96574	223.91754	70.01180	85.48567 ± 6.11803	210.12425 ± 16.99204	43.40723 ± 31.78809
M_0	deg	0.00000	0.00000	0.00000	5.18482 ± 3.84571	11.58305 ± 8.87570	42.36104 ± 29.98678
i	deg	89.47231	89.10159	115.68159	89.43632 ± 0.30223	88.99503 ± 0.54176	103.58128 ± 4.14661
Ω	deg	0.00000	0.17063	0.00000	123.30784 ± 87.12008	162.09943 ± 91.36624	139.42421 ± 90.81975
$-\ln \mathcal{L}$...		73.34798			-848.73127	
χ^2	...		158			1991	
χ_{red}^2	...		32			398	
$\Delta AICc$...		419.69596			-1424.46254	

Table 19. Comparisons of best-fit model fitting parameters among the mass-less planets, 2-planet, and 3-planet cases.

Best-fit Model	χ^2	χ_{red}^2	$-\ln \mathcal{L}$	$\Delta AICc$
No TTVs	41367738	2954838	-20683716.480	-41367384.960
2-planet	428	36	-61.939	-57.697
3-planet	158	32	73.348	419.696

M_J (or $24.8 \pm 1.2 M_{\oplus}$) at $20.7\text{-}\sigma$ significance, which makes it roughly a Neptune-sized planet. In the case of our representative 3-planet scenario, our calculation yields the mass of c to

be $0.0631 \pm 0.0049 M_J$ (or $20.1 \pm 1.6 M_{\oplus}$) at $12.6\text{-}\sigma$ significance, implying that it again has roughly the mass of Neptune.

5. PHOTODYNAMICAL ANALYSIS

In a second independent analysis to validate our methods, we used a photodynamical code to simultaneously fit the transit light curves and TTVs. The core of this code is based on **rebound** (Rein & Liu 2012; Rein & Spiegel 2015) with which the N-body problem is integrated using the high accuracy non-symplectic integra-

Table 20. Parameters for the photodynamical models, with model a the simultaneous fit of stellar activity variation & flares and model b the pre-cleaned data.

Parameter	Unit	Model a		Model b	
		AU Mic b	AU Mic c	AU Mic b	AU Mic c
M_p	M_\oplus	16_{-9}^{+12}	$10.8_{-2.2}^{+2.3}$	13_{-2}^{+8}	13_{-2}^{+5}
P_{orb}	day	$8.4626_{-0.0001}^{+0.0001}$	$18.8624_{-0.0011}^{+0.0015}$	$8.4626_{-0.0002}^{+0.0001}$	$18.860_{-0.002}^{+0.002}$
e	...	$0.022_{-0.006}^{+0.005}$	$0.097_{-0.013}^{+0.010}$	$0.012_{-0.003}^{+0.003}$	$0.069_{-0.014}^{+0.025}$
ω	deg	84_{-9}^{+7}	$99.1_{-3.5}^{+3.7}$	103_{-7}^{+6}	112_{-9}^{+5}
t_{peri}	day	$4.87_{-0.21}^{+0.16}$	$4.89_{-0.16}^{+0.15}$	$5.3_{-0.2}^{+0.2}$	$5.5_{-0.4}^{+0.2}$
R_p/R_\star	...	$0.0529_{-0.0002}^{+0.0002}$	$0.032_{-0.001}^{+0.002}$	$0.0511_{-0.0001}^{+0.0002}$	$0.034_{-0.001}^{+0.006}$
i	deg	$89.20_{-0.06}^{+0.06}$	$90.8_{-0.1}^{+0.1}$	$89.11_{-0.03}^{+0.03}$	$89.4_{-0.07}^{+0.08}$

NOTE—Orbital elements are given for BJD 2458300.

tor with adaptive time-stepping IAS15. At the times of the measured mid-transit times, the current orbital elements are used to calculate the corresponding transit light curve using the python implementation of the model from [Mandel & Agol \(2002\)](#) from Ian Crossfield²¹. Using the Markov chain Monte Carlo sample `emcee` ([Foreman-Mackey et al. 2013](#)), we sample the parameter space maximizing the log likelihood. In addition to the transit light curves, the code also fits the radial velocity (RV) data of AU Mic taken with *SPIRou* ([Cale et al. 2021](#); [Klein et al. 2021](#)), which at near-infrared wavelengths is least impacted by the stellar activity of this young system. The RV model is calculated from the same `rebound` N-body integration of the planetary system. As free parameters we have the planetary masses, orbital periods, eccentricities, longitudes of periastron, inclination, and the R_p/R_\star ratio. The stellar mass and radius, hence the stellar density, is fixed. The limb darkening for the various bands are taken from ([Claret et al. 2012](#); [Claret 2017](#)) and are kept at the literature values. Since the *Spitzer* transits show depth variations, we account for this effect by a third light contribution as free pa-

rameter (to be explored further in future work). All data sets have their individual offsets, while the *SPIRou* data are modeled by adding a “jitter” white noise term.

The stellar activity is modeled using `celerite` ([Foreman-Mackey et al. 2017](#)), which has the advantage to offer a fast and scalable implementation of Gaussian Process (GP) regression, especially important for large data sets. The `celerite` package provides several built-in covariance kernels, one is representing damped oscillations driven by white noise called SH0. It has three parameters: the undamped oscillator frequency or period $\omega_0 = 2\pi/P$, the quality factor Q of the oscillator (which is reversely proportional to the damping time scale τ), and the variance S_0 . For more details, see equations (19)-(24) in [Foreman-Mackey et al. \(2017\)](#). Star spots typically manifest in variations at the rotation period as well as on its first harmonic. In order to represent this in a *rotational* kernel, we follow the idea presented in `celerite2` ([Foreman-Mackey et al. 2017](#); [Foreman-Mackey 2018](#))²² and use the sum of two SH0 kernels, where only one of the frequencies is a free hyperparameter and the other is fixed to its first harmonic. Both oscillators are forced by a lower

²¹ https://www.lpl.arizona.edu/~ianc/python/_modules/transit.html

²² <https://celerite2.readthedocs.io/en/latest/api/python>

boundary of the quality factor to be in the underdamped regime (i.e., $Q > 1/2$). For the RV data and the *TESS* light curves, the same rotation period and quality factors are enforced; however, the variance can differ.

We performed the photodynamical modeling in two versions. In the first (model a, using 45 000 steps after 10 000 burn-in steps and 400 walkers), we simultaneously fit the flares in the *TESS* light curves using the flare model `aflare` (Davenport et al. 2014). In the second version (model b, using 10 000 steps after 10 000 burn-in steps and 100 walkers, will be increased), we use the cleaned *TESS* light curve from Gilbert et al. (2021), where also the variation due to stellar activity has been corrected, i.e. no GP modeling is required here for the transit light curves. The parameters of the photodynamical fits are listed in Table 20 and are displayed in Figures B1 & B2.

5.1. Photodynamical Modeling Results

In this subsection, we present a summary of the key results of our photodynamical modeling. Model a has the advantage to provide a simultaneous fit of the transits, stellar activity modulation, and flares. Since the timescales of ingress and egress are similar to those of the flares, a simultaneous fit should provide a more robust result. The flexibility of the GP kernels, however, may compensate for small deviations in time between observed and modelled transits. Comparing the calculated transit midpoints of a best fit to the *a priori* measured mid-transit times indeed show deviations on the order of 10 minutes. Either the transit midpoint measurements are affected by systematic errors due to the stellar activity and flaring, or the GP model is too flexible and hides these discrepancies. In model b, this is prevented due to a pre-cleaning of the light curve, however, with the caveat that the measured mid-transit times may be affected by activity modulation and flaring. A comparison between the two approaches shows that we

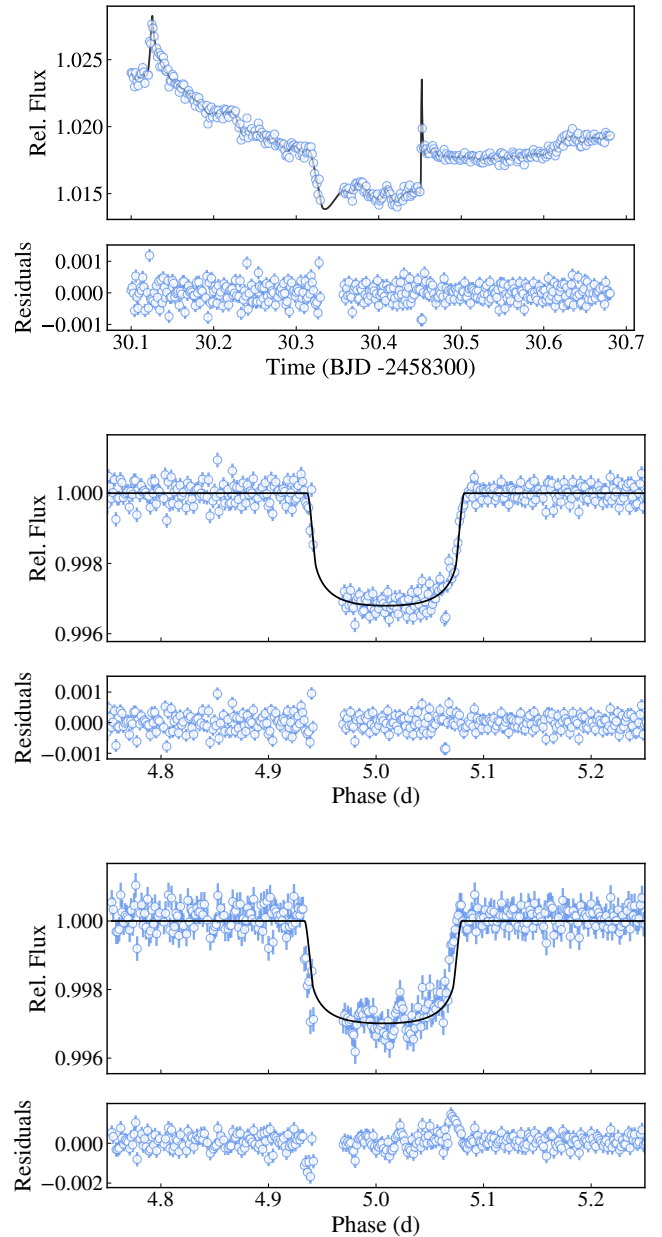


Figure 7. The first *TESS* transit of AU Mic b in Sector 1. From top to bottom: *TESS* light curve with stellar activity variation and flares overlaid with the best-fit model a from the photodynamical analysis, best-fit model a with contribution of stellar activity variation and flares removed, best-fit model b.

can obtain a 2-planet model which fits all transits (*TESS*, *Spitzer*, and ground-based) if the stellar variability and flares are fitted simultaneously, while all models compared to the pre-

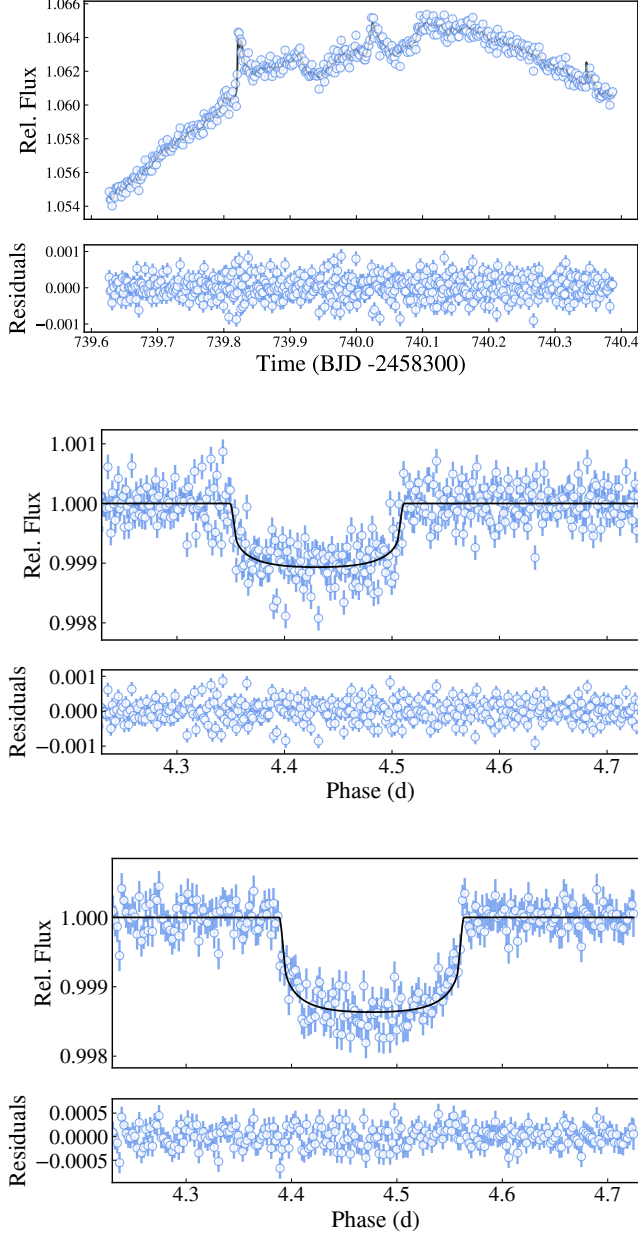


Figure 8. The first *TESS* transit of AU Mic c in Sector 27. From top to bottom: *TESS* light curve with stellar activity variation and flares overlaid with the best-fit model a from the photodynamical analysis, best-fit model a with contribution of stellar activity variation and flares removed, best-fit model b, which shows by eye a clear timing offset when the activity is modeled separately from the photodynamical modeling.

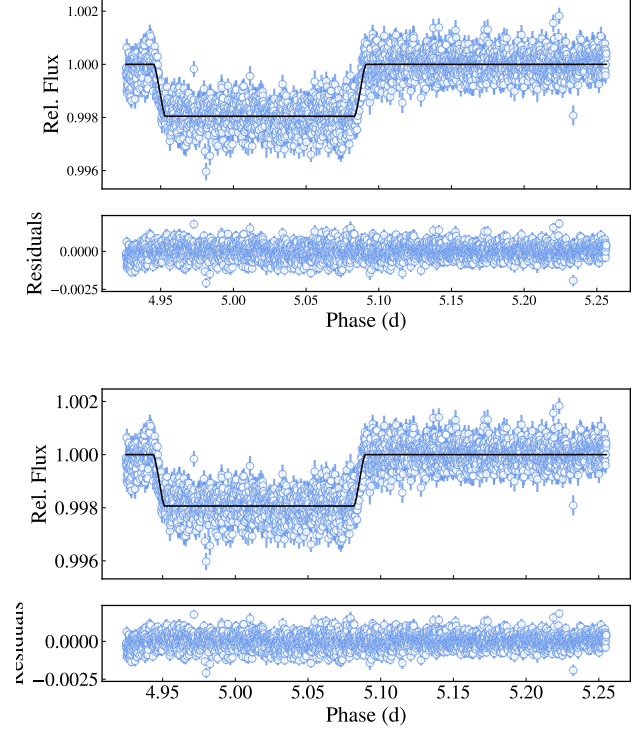


Figure 9. The first *Spitzer* transit of AU Mic b, with the best-fit model a (top) and best-fit model b (bottom) from the photodynamical analysis.

cleaned data show noticeable discrepancies. As an example, we show the first transit of AU Mic b in Sector 1 of *TESS* in Figure 7, on the top two panels from the simultaneous stellar variability and flare fit and on the bottom panel from the pre-cleaned data. We also show the best-fit for one of the *Spitzer* light curves in Figures 8 & 9.

While the best fit of the photodynamical model including stellar variability and flares is promising, we note the above mentioned compensation of deviations between models and observation due to the flexibility of the GP model. Further transits will be required to check this model. The timing discrepancies in the second version of the photodynamical fit corroborate the conclusion from our TTV fitting (i.e., a 2-planet model is not able to reproduce the small but detectable TTVs).

6. DISCUSSION

In this section we present the key results of our analyses in §6.1, followed by the impact of the rotational modulation of stellar spots and plagues in §6.2 and flares in §6.3. In §6.4, we assess the likelihood of an additional middle non-transiting planet candidate to explain in the observed TTVs, and in §6.5 we compare our analyses’ constraints on the mass of AU Mic c. Lastly, in §6.6, we discuss the limitation of our joint modeling.

6.1. Key Results of Analyses

In the preceding sections, we modeled the transit observations of AU Mic b and c to ascertain whether or not transit timing variations were present, and whether or not they can be accounted for by our existing knowledge of this planetary system and be used to constrain the dynamical orbits and masses of the two transiting planets. Given the inherent stellar activity in this young system, we explored two different and independent analyses: in §4 a dynamical model of the transit midpoint times, and in §5 a full photodynamical model. We found in both scenarios indications of transit timing variations deviating from a linear ephemeris on the order of ten minutes, particularly when comparing the *TESS* and *Spitzer* transit times, and generally consistent results, albeit with larger timing uncertainties, from the ground-based transits and R-M observations (Figure 3).

We next explored whether the two transiting planets could account for the observed TTVs. We first attempted a 2-planet dynamical model for the TTVs with only the high precision *TESS* transits, which we were able to find a fit akin to that derived in Martioli et al. (2021). These transit times were derived with the joint stellar activity model in Gilbert et al. (2021) who find evidence for TTVs on the order of a few minutes. However, when including the *Spitzer* transits, which are less susceptible to stellar activity at $4.5 \mu\text{m}$, we find that the *Spitzer* transits are incompatible with this model within the mea-

sured timing uncertainties, showing a significant departure from a circular two-planet model on the order of ~ 10 minutes. We next considered whether orbital eccentricity could account for the observed TTVs, but derive high eccentricities that are incompatible with the light curves themselves which exclude high eccentricity scenarios (Plavchan et al. 2020; Gilbert et al. 2021).

With the full photodynamical analysis in §5, we were able to jointly model the activity and transits to reproduce the observed transit midpoint times. However, this left open the possibility that the flexibility of the GP for the rotational modulation of the starspots could also absorb any of the TTVs present. In fact, with a second photodynamical model using Gilbert et al. (2021) activity model detrended transit light curves (e.g. the stellar activity in corrected serially rather than jointly with the photodynamical analysis), we found excess TTVs not explained by the 2-planet model alone.

In order to explain the observed excess of TTVs than accounted for by our two-planet modeling, we next investigate in turn the following possibilities. First, that our modeling of the rotational modulation of star spots is underestimating the impact on the TTVs. Second, we consider the impact the flares have on our TTVs. Third, we consider the possibility of a third planet in the AU Mic system not yet detected to transit nor through RVs. Finally, we consider the limitations of our analysis and statistical methods.

6.2. Stellar Spots

Stellar spots can significantly impact the recovered stellar and planetary model parameters (Pont et al. 2007; Czesla et al. 2009; Berta et al. 2011; Désert et al. 2011; Ballerini et al. 2012) and can produce TTV-like signals that potentially lead to false-positive detection of non-transiting planets (Alonso et al. 2009; Sanchis-Ojeda et al. 2011; Sanchis-Ojeda & Winn 2011; Oshagh et al. 2012). For $R_p/R_\star \approx 0.05$ (as is the

case for AU Mic b), the expected maximum amplitude of the spot-induced TTV in seconds at visible wavelengths is $AMP = 139 \times f$, where f is the stellar spot filling factor in percent (Oshagh et al. 2013). If $f = 0.25\%$, 1% , or 3% , the maximum amplitude would be 34.75, 139, or 417 seconds (0.6, 2.3, or 7.0 minutes), respectively. Given the long-lived spot lifetimes for AU Mic, it is not unreasonable to assume that the spot-filling fraction is $>3\%$ and thus the impact of the rotational modulation of starspots could be on the order of >7 minutes. Oshagh et al. (2013) added that if the transit duration and depth priors were fixed (and not modeled), the TTV amplitude would be smaller than if they were floating.

First, we consider the wavelength dependence of the TTVs. The *Spitzer* transit times have greater photometric precision due its larger aperture, a much higher cadence, and consequently more precise transit midpoint times (to within 13 seconds). Further, the *Spitzer* observations are less impacted by the rotational modulation of stellar activity at $4.5 \mu\text{m}$ due to the decreased flux contrast of any spots; the rotational modulation of stellar activity should be significantly decreased in amplitude. This decreased amplitude of the impacts of stellar activity with increasing wavelength is also observed for AU Mic in photometry (Hebb et al. 2007) and in radial velocities (Cale et al. 2021). However, the *Spitzer* transits show the most significant deviations from a linear ephemeris than those derived by the *TESS* data alone, running counter-intuitive to the expected impact the rotational modulation of starspots would have on the derived transit times.

Second, Szabó et al. (2021) measured AU Mic’s rotation period with *TESS* data and AU Mic b’s orbital period with both *TESS* and *CHEOPS* light curves and found that the ratio between these two periods implies the 7:4 spin-orbit commensurability. Due to this reso-

Table 21. Weighted averages of the respective initial, 2-planet-model-subtracted, & 3-planet-model-subtracted TTVs as a function of transit number modulo 4.

Phase	TTV ₁ (min)	TTV ₂ (min)	TTV ₃ (min)
1	0.52 ± 1.17	-0.90 ± 0.59	-0.40 ± 0.59
2	4.61 ± 1.00	1.11 ± 0.52	0.06 ± 0.52
3	0.99 ± 1.28	0.61 ± 0.79	1.88 ± 0.79
4	4.89 ± 1.13	-0.36 ± 0.54	-0.40 ± 0.54

nance, for every fourth transit of AU Mic b, the transit takes place over the same range of stellar longitudes of AU Mic. In other words, the same stellar “side” is transited every fourth transit. Thus the impact of the stellar rotational modulation of spots should produce the same systematic impact on the TTVs every fourth transit. For example, if the 1st transit of AU Mic b is 4 minutes “late” from the apparent effects of starspots, then this will also be true for the 5th, 9th, 13th, 17th, ..., Nth transits. Given AU Mic’s long spot lifetime, relatively unchanged between *TESS* sectors 1 and 27 two years later, this pattern will have persisted over the duration of our observations.

To explore the impact of spot modulations on TTVs, we calculated the weighted average of the initial, 2-planet model, and 3-planet model TTVs for each of the four phases (Table 21); from there we can see correlations between phases 1 & 3 and phases 2 & 4. However, after subtracting the 2-planet and 3-planet models from the respective TTVs, these correlations disappeared. Thus, no such “modulo 4” pattern is observed in the AU Mic b transit times (Figure 10), with transits being neither systematically late nor early in phase with the stellar longitude crossings. The three *Spitzer* transits are from three different sets of stellar longitude crossings, and one of the R-M observation midpoint times is from the fourth set of stellar lon-

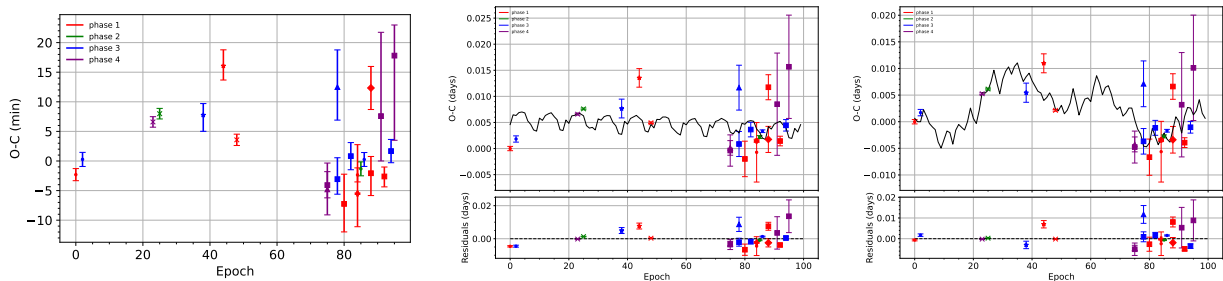


Figure 10. O–C Diagram of AU Mic b from initial model (left), Exo-Striker 2-planet model (center) and Exo-Striker 3-planet model (right)

, color-coded as a function of transit number modulo 4, using the `EXOFASTv2`-generated measured midpoint times and the calculated midpoint times for all 23 AU Mic b transit data sets from Table 3. Here, we explore the impact the rotational modulation of starspots, given the 7:4 spin-orbit commensurability, may have on the observed TTVs. The weighted averages of the distribution of TTVs for each of the four stellar longitude crossing phases are in Table 21; they show correlations between phases 1 & 3 and phases 2 & 4. However, after subtracting the 2 and 3 planet models from the TTV data, the weighted averages show no clear correlation of more than ~ 2 minutes, indicating that stellar spots of AU Mic are not a significant factor in accounting for the timing of transits for AU Mic b. The epochs are relative to the first *TESS* transit of AU Mic b.

gitude crossings; all four transit-midpoint times are systematically late w/r/t to the *TESS* transit times by ~ 5 -10 minutes. The *TESS* transits themselves also encompass three of the four stellar longitude crossing sets, and the variation in transit times between them is less than a couple of minutes.

Third, Gilbert et al. (2021), in deriving the *TESS* transit midpoint times, includes the joint modeling of the rotational modulation of the starspots in deriving the transit midpoint times. This analysis approach thus mitigates any impact the spot modulation has on the values of the derived transit midpoint times as estimated in Oshagh et al. (2013). Additionally, because of the joint modeling of the *TESS* transits, the impact of the rotational modulation is reflected in the posterior uncertainties and thus precision in the derived transit times. Our photodynamical analysis has shown that when modeling the rotational modulation of starspots with a GP in parallel with deriving transit midpoint times, as opposed to in series, the GP can absorb rather than introduce additional TTVs on the order of a few minutes for AU Mic.

Thus, in light of the modeling presented herein and Gilbert et al. (2021) the rotational modulation of starspots can likely be ruled out as an explanation for our observed TTVs between *TESS* and *Spitzer*. More detailed synthetic simulations will be needed in the future to further quantify the impact of the rotational modulation of AU Mic starspots on the derived transit times, but that is beyond the scope of this work. We next turn to assess the impact of flares on the derived transit times.

6.3. Stellar Flares

Like stellar spots, stellar flares can impact the midpoint timing of the transits, particularly when they occur during ingress or egress, which happened several times during the *TESS* transits. For the ground-based transit data, it is difficult to resolve the flares due to the relatively lower photometric precision, and additionally AIJ and `EXOFASTv2` do not include joint modeling of flares during transits. The ground-based transit times also possess larger timing uncertainties, which may mask the impact of flares.

Several flares occurred during the *TESS* observations, but Gilbert et al. (2021) jointly mod-

eled them with the `bayesflare` (Pitkin et al. 2014) and `xoflares` packages, some of which do occur during egress and thus could impact the derived transit midpoint times were they not modeled jointly. Additionally, the O–C diagram from our photodynamical analysis demonstrates that the derived transit times are sensitive to the methods employed for accounting for the stellar flares. However, the analysis done by Gilbert et al. (2021) shows no dependence of transit timing on activity after marginalizing over models for the flares and spot modulation, and the *TESS* transit times of AU Mic b are fairly constant to within ~ 4 minutes.

The second partial *Spitzer* transit of AU Mic b contains an obvious flare during transit, which we marginalize over in our modeling, thus impacting our derived timing uncertainties. Additionally, the first and third *Spitzer* transits may show some small flares pre-ingress which we do not account for in our modeling. As with spots, however, flares are smaller in amplitude at $4.5 \mu\text{m}$ than at visible wavelengths and thus should have a relatively smaller impact on the derived transit times. However, we find that the first two *Spitzer* transit times are consistent with one another, and the third *Spitzer* transit is most contemporaneous with the R-M transit observations.

For the *SPIRou* + *iSHELL* R-M transit observation, the analysis took into account the impact of magnetic activity and flares by constructing a model using a similar approach from Donati et al. (2020), which is then subtracted from the RV observations. Similarly, for the *ESPRESSO* data, the stellar activity was modeled using the `celerite` package’s GP that is described by a Matérn 3/2 kernel and then subtracted from the RV data.

All five R-M and *Spitzer* transits show significantly deviant and late transit times; it would be difficult and randomly unlucky to have randomly timed flares during the different transits

all impact the derived transit midpoint times in the same way – late, as opposed to early. While these results are based on a relatively small number of transits, it seems unlikely that flares can account for the observed TTV excesses. More detailed simulations in the future will be needed to assess the impact of flares on the transit times of AU Mic, but that is beyond the scope of this work. We next turn to consider the possibility of additional planets in the AU Mic system.

6.4. *Existence of a planet d candidate?*

In the previous subsections, we explored the stellar activity of AU Mic and the significance of its impact on the TTVs, both through the rotational modulation of starspots and flares. It is possible that there is some unaccounted-for effect in the derived TTV uncertainties, but we deem this scenario unlikely given the above marginalization over our activity models in the derived transit time posteriors. Thus, we turn to another possibility: the presence of a third planet.

Cale et al. (2021) explored additional candidate RV planet signals when modeling the RVs of the AU Mic system. One candidate period that was explored in particular was the presence of a planet in-between b and c, a “middle-d” non-transiting planet with a period of 12.742 days. Such a planet would establish that the AU Mic system is in a 4:6:9 orbital commensurability and result in significant TTVs. In §4.2.2, we modeled this 3-planet configuration with `Exo-Striker` based on this candidate RV signal from Cale et al. (2021). Since the AMD criterion indicated that this configuration is unstable, we tested its stability with N-body packages, including `rebound` (Rein & Liu 2012; Rein & Spiegel 2015) and `mercury6` (Chambers 1999), the latter of which was used as a consistency check. The `mercury6` simulation ran for 10 Myrs while the `rebound` simulation ran for 2 Myrs; both indicated that the 3-planet con-

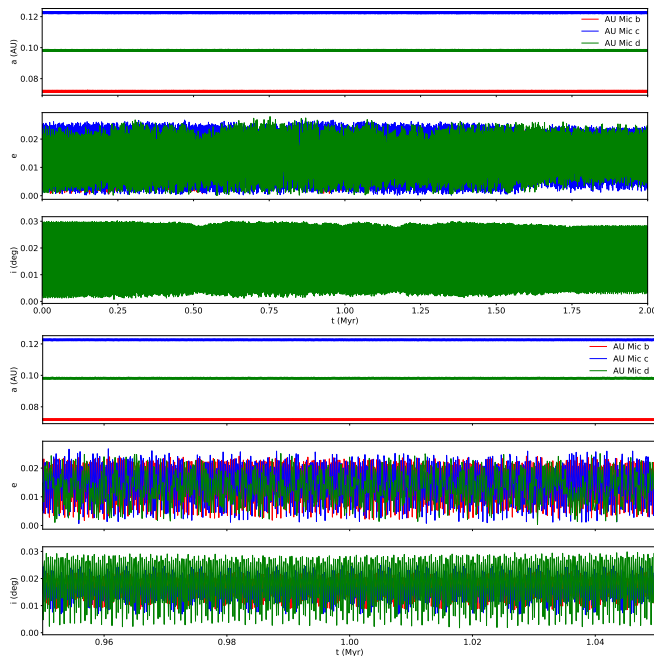


Figure 11. rebound model of the stability of 3-planet system for AU Mic. The top three plots span 2 Myrs while the bottom three plots are zoomed in between 0.95 and 1.05 Myrs.

figuration from §4.2.2 is stable (see Figure 11 for outputs from **rebound**). Additional possible configurations, including having a planet beyond c, is beyond the scope of this work. While we find that our TTVs are consistent with a possible third “middle d” transiting planet, we neither confirm nor rule out its existence. If this third planet does exist, our dynamical modeling implies the impact on the observed TTVs will be more readily apparent with additional TTV measurements in 2021 and the next several years, as the TTVs for AU Mic b would deviate further from a linear ephemerides, and given the “curvature” in the TTVs from the first three years of TTVs presented herein.

6.5. Implication on the Mass of AU Mic c

With only three transits of AU Mic c, all with relatively larger transit timing uncertainties, we do not derive a TTV mass constraint for AU Mic b. However, from the perturbations of the transit times of AU Mic b, we are able to place

Table 22. Characteristics of AU Mic c.

Property	Unit	Quantity	Ref
Mass	M_{\oplus}	$9.60^{+2.07}_{-2.31}$	K_{J1} (Cale et al. 2021)
		$14.12^{+2.48}_{-2.71}$	K_{J2} (Cale et al. 2021)
		24.8 ± 1.2	Exo-Striker 2-planet Model
		20.1 ± 1.6	Exo-Striker 3-planet Model
		$10.8^{+2.3}_{-2.2}$	Photodynamical Model a
		13^{+5}_{-2}	Photodynamical Model b
Radius	R_{\oplus}	$2.79^{+0.31}_{-0.30}$	Gilbert et al. (2021)
Density	g/cm^3	$2.44^{+0.97}_{-0.98}$	K_{J1} (Cale et al. 2021)
		3.58 ± 1.35	K_{J2} (Cale et al. 2021)
		$6.28^{+2.12}_{-2.05}$	Exo-Striker 2-planet Model
		$5.08^{+1.74}_{-1.69}$	Exo-Striker 3-planet Model
		$2.75^{+1.09}_{-1.05}$	Photodynamical Model a
		$3.3^{+1.7}_{-1.2}$	Photodynamical Model b

constraints on the mass of AU Mic c. Table 22 summarizes our **Exo-Striker** and photodynamical TTV masses with the RV masses from Cale et al. (2021). In both our 2-planet and 3-planet **Exo-Striker** models, the mass of AU Mic c is approximately that of Neptune. Both photodynamical models determine the mass of AU Mic c to be more comparable to that of Uranus instead of the more massive Neptune. The densities of AU Mic c using the masses from **Exo-Striker** analyses are quite high. We instead adopt as our final mass estimate for AU Mic c of $10.8^{+2.3}_{-2.2} M_{\oplus}$, the value from our “a” photodynamical model which jointly models the stellar activity with the transit dynamics with no third planet. This value is consistent with the mass for AU Mic c as determined from RVs (as are all the masses we derive). Note that we only list the masses of AU Mic c; we currently do not have enough transits nor enough precision on the timing of transits for AU Mic c to place a meaningful constraint on the mass of AU Mic b.

6.6. Limitation of Our Joint Modeling & Future Work

In this subsection, we discuss some of the limitations of our analysis. First, we do not perform joint RV + TTV modeling because the RVs require a custom treatment of stellar activity that is an order of magnitude larger in effective amplitude relative to the Keplerian orbital reflex motion of the star (Cale et al. 2021). We also sought to conduct an independent TTV modeling to compare with the RV analysis, given the complexity of the RV model. Additionally, to our knowledge, no prior work exists in performing a joint RV + TTV modeling in the presence of such stellar activity as exhibited by AU Mic.

Second, in RVs it is common to adopt a “jitter” term representing the white-noise measurement error that is not captured by the formal measurement uncertainties and added in quadrature, without which Keplerian orbital fits can yield reduced- $\chi^2 \gg 1$. A similar approach may be employed for AU Mic in a future study for the TTV modeling – including a “jitter” term that accounts for timing uncertainties not captured by our modeling of spots, flares and orbital dynamics. We do not undertake such an analysis herein for several reasons. First, *Exo-Striker* does not include a “jitter” TTV error term, and thus we cannot marginalize over this parameter; e.g., we would need to assume a “jitter” timing term and inflate our timing measurement uncertainties. Second, our timing data is fairly in-homogeneous, spanning a range of precision and wavelength from ground and space facilities; we would need multiple independent jitter terms that are not well constrained; our *Spitzer* data that most deviates from a two-planet TTV model is least impacted by stellar activity. Third, as shown in Szabó et al. (2021), due to the 7:4 period commensurability of the stellar rotation to the orbital period of AU Mic b, the TTV “jitter” from spots will not be a white noise term; given the known stellar rotation period, the timing impact is not simply random and fairly deterministic, as we

have undertaken our “mod-4” transit analysis to identify whether or not the transit times correlation with the stellar longitude crossings. That being said, the flares are random in time and will randomly impact the measured transit times. Therefore, a “jitter” term would be appropriate for accounting for the impact of flares on measured the TTVs that are not captured by our flare modeling of the light curves.

Third, the uncertainties in the midpoint times from the R-M observations are likely to be underestimated. As allowing certain parameters, such as the orbital period and eccentricity, to remain free will result in degeneracy in the R-M model, setting such parameters fixed would avoid this issue but would cause the uncertainties to be underestimated.

As a consequence of these limitations in our analysis, we do not perform any statistically robust model comparisons between the 2- and 3-planet TTV models. Future observations and analyses will be necessary to reach a definitive conclusion for the hypothetical third planet candidate.

7. CONCLUSION

AU Mic hosts a young nearby exoplanet system that serves as a useful laboratory for probing and characterizing young exoplanetary systems. We have collected 23 transits from AU Mic b and 3 transits from AU Mic c over the course of three years. We model the observed transits and derive new transit model posteriors. We have run two independent methods (*Exo-Striker* and photodynamical) in modeling the transits and the timing of those transits. Our observations and analyses of the transits of AU Mic b and c show that AU Mic b is exhibiting TTVs, consistent with Szabó et al. (2021), Martioli et al. (2021), and Gilbert et al. (2021). Our photodynamical model yields the mass for AU Mic c of $10.8_{-2.2}^{+2.3} M_{\oplus}$, consistent with the RV-determined mass in Cale et al. (2021). However, going beyond the work of Szabó et al.

(2021) and Martioli et al. (2021), our TTVs show timing excess of >5 minutes that appear to discrepant with a 2-planet model alone, particularly when comparing the *Spitzer* and *TESS* derived transit times, the former of which is presented for the first time herein. Further, we marginalize our TTV models over our models for the rotational modulation of stellar activity and flares. Consequently, stellar activity, while not excluded through statistically robust model comparison, does not appear likely to be able to account for the observed TTV excess. We mapped the O–C diagram taking into account AU Mic’s stellar spin 7:4 commensurability with the orbital period of AU Mic b from Szabó et al. (2021), and we did not identify that the spot modulation results in a significant effect on the observed TTVs as a function of stellar longitude crossings. We explore a possible, representative, and non-exhaustive 3-planet configuration scenario that is: consistent with the identified non-transiting “middle-d” RV candidate signal in Cale et al. (2021), is dynamically stable, would establish the AU Mic system of planets in a 4:6:9 orbital period commensurability, and can account for the observed TTV excess of our data.

Nonetheless, given the high level of stellar activity for AU Mic, we cannot ignore the possibility that our modeling and marginalization over our stellar activity models does not fully account for some effects that significantly impact the observed TTVs. Thus, additional ground- and space-based TTVs in the next few years are needed to further vet the impact of stellar activity on the observed TTVs, or to confirm the possibility that the excess TTVs are due to the RV candidate highlighted in Cale et al. (2021), and to enable a more thorough search of the possible orbital periods for possible additional planets in the AU Mic system. Such observations will be possible from the ground, with *CHEOPS* now,

or with upcoming missions such as the *Pandora* and *Twinkle* missions, *Ariel*, and/or *JWST*.

PPP acknowledges support from NASA (Exoplanet Research Program Award #80NSSC20K0251, TESS Cycle 3 Guest Investigator Program Award #80NSSC21K0349, JPL Research and Technology Development, and Keck Observatory Data Analysis) and the NSF (Astronomy and Astrophysics Grants #1716202 and 2006517), and the Mt Cuba Astronomical Foundation. DD acknowledges support from the TESS Guest Investigator Program grant #80NSSC21K0108 and NASA Exoplanet Research Program grant #18-2XRP18-2-0136. EG acknowledges support from the NASA Exoplanets Research Program Award #80NSSC20K0251. The material is based upon work supported by NASA under award #80GSFC21M0002. LDV acknowledges funding support from the Heising-Simons Astrophysics Postdoctoral Launch Program, through a grant to Vanderbilt University.

This paper includes data collected by the TESS mission, which are publicly available from the Mikulski Archive for Space Telescopes (MAST). Funding for the TESS mission is provided by NASA’s Science Mission directorate. Resources supporting this work were provided by the NASA High-End Computing (HEC) Program through the NASA Advanced Supercomputing (NAS) Division at Ames Research Center for the production of the SPOC data products.

This work is based [in part] on observations made with the Spitzer Space Telescope, which was operated by the Jet Propulsion Laboratory, California Institute of Technology under a contract with NASA. Support for this work was provided by NASA through an award issued by JPL/Caltech. This research has made use of the NASA/IPAC Infrared Science Archive, which is funded by the National Aeronautics and Space

Administration and operated by the California Institute of Technology.

This work makes use of observations from the Las Cumbres Observatory global telescope network. Part of the LCOGT telescope time was granted by NOIRLab through the Mid-Scale Innovations Program (MSIP). MSIP is funded by NSF.

This research made use of the PEST photometry pipeline²³ by Thiam-Guan Tan. This research has made use of the NASA Exoplanet Archive and the Exoplanet Follow-up Observation Program website, both of which are operated by the California Institute of Technology, under contract with the National Aeronautics and Space Administration under the Exoplanet Exploration Program. This research has made use of the SIMBAD database, operated at CDS, Strasbourg, France. This research has made use of NASA’s Astrophysics Data System Bibliographic Services. This research has made use of an online calculator that converts a list of Barycentric Julian Dates in Barycentric Dynamical Time (BJD_TDB) to JD in UT (Eastman et al. 2010)²⁴.

We also give thanks to Trifon Trifonov for his assistance in the use of the *Exo-Striker* package and analysis of the AU Mic system.

Facilities: Brierfield:0.36 m (Moravian G4-16000 KAF-16803), CFHT (SPIRou), ExoFOP, Exoplanet Archive, IRSA, LCOGT (SAAO:1 m & SSO:1 m; *Sinistro*), MAST, PEST:0.30 m (*SBIG ST-8XME*), Spitzer (*IRAC*), TESS, VLT:Antu (*ESPRESSO*)

Software: AstroImageJ (Collins et al. 2017), astropy (Astropy Collaboration et al. 2013, 2018), batman (Kreidberg 2015), bayesflare (Pitkin et al. 2014), celerite (Foreman-Mackey et al. 2017), celerite2 (Foreman-Mackey et al. 2017; Foreman-Mackey 2018), emcee (Foreman-Mackey et al. 2013), EXOFASTv2 (Eastman et al. 2019), exoplanet (Foreman-Mackey et al. 2021), Exo-Striker (Trifonov 2019), fleck (Morris 2020), ipython (Pérez & Granger 2007), lightkurve (Lightkurve Collaboration et al. 2018), matplotlib (Hunter 2007), mercury6 (Chambers 1999), numpy (Harris et al. 2020), rebound (Rein & Liu 2012; Rein & Spiegel 2015), scipy (Virtanen et al. 2020), TAPIR (Jensen 2013), xoflares (Gilbert et al. 2021)

REFERENCES

- Addison, B. C., Horner, J., Wittenmyer, R. A., et al. 2020, arXiv e-prints, arXiv:2006.13675, <https://arxiv.org/abs/2006.13675>
- Afram, N., & Berdyugina, S. V. 2019, *A&A*, 629, A83, doi: [10.1051/0004-6361/201935793](https://doi.org/10.1051/0004-6361/201935793)
- Agol, E., Steffen, J., Sari, R., & Clarkson, W. 2005, *MNRAS*, 359, 567, doi: [10.1111/j.1365-2966.2005.08922.x](https://doi.org/10.1111/j.1365-2966.2005.08922.x)
- Akeson, R. L., Chen, X., Ciardi, D., et al. 2013, *PASP*, 125, 989, doi: [10.1086/672273](https://doi.org/10.1086/672273)
- Alonso, R., Aigrain, S., Pont, F., Mazeh, T., & CoRoT Exoplanet Science Team. 2009, in *Transiting Planets*, ed. F. Pont, D. Sasselov, & M. J. Holman, Vol. 253, 91–96, doi: [10.1017/S1743921308026276](https://doi.org/10.1017/S1743921308026276)
- Anderson, D. R., Hellier, C., Gillon, M., et al. 2010, *ApJ*, 709, 159, doi: [10.1088/0004-637X/709/1/159](https://doi.org/10.1088/0004-637X/709/1/159)
- Astropy Collaboration, Robitaille, T. P., Tollerud, E. J., et al. 2013, *A&A*, 558, A33, doi: [10.1051/0004-6361/201322068](https://doi.org/10.1051/0004-6361/201322068)
- Astropy Collaboration, Price-Whelan, A. M., Sipőcz, B. M., et al. 2018, *AJ*, 156, 123, doi: [10.3847/1538-3881/aabc4f](https://doi.org/10.3847/1538-3881/aabc4f)

²³ <http://pestobservatory.com>

²⁴ <https://astroutils.astronomy.osu.edu/time/bjd2utc.html>

- Bailer-Jones, C. A. L., Rybizki, J., Fouesneau, M., Mantelet, G., & Andrae, R. 2018, *AJ*, 156, 58, doi: [10.3847/1538-3881/aacb21](https://doi.org/10.3847/1538-3881/aacb21)
- Ballerini, P., Micela, G., Lanza, A. F., & Pagano, I. 2012, *A&A*, 539, A140, doi: [10.1051/0004-6361/201117102](https://doi.org/10.1051/0004-6361/201117102)
- Becker, J. C., Vanderburg, A., Adams, F. C., Rappaport, S. A., & Schwengeler, H. M. 2015, *ApJL*, 812, L18, doi: [10.1088/2041-8205/812/2/L18](https://doi.org/10.1088/2041-8205/812/2/L18)
- Benisty, M., Bae, J., Facchini, S., et al. 2021, *ApJL*, 916, L2, doi: [10.3847/2041-8213/ac0f83](https://doi.org/10.3847/2041-8213/ac0f83)
- Berta, Z. K., Charbonneau, D., Bean, J., et al. 2011, *ApJ*, 736, 12, doi: [10.1088/0004-637X/736/1/12](https://doi.org/10.1088/0004-637X/736/1/12)
- Bonfanti, A., Delrez, L., Hooton, M. J., et al. 2021, *A&A*, 646, A157, doi: [10.1051/0004-6361/202039608](https://doi.org/10.1051/0004-6361/202039608)
- Borucki, W. J., Koch, D., Basri, G., et al. 2010, *Science*, 327, 977, doi: [10.1126/science.1185402](https://doi.org/10.1126/science.1185402)
- Brown, T. M., Baliber, N., Bianco, F. B., et al. 2013, *PASP*, 125, 1031, doi: [10.1086/673168](https://doi.org/10.1086/673168)
- Bryant, E. M., Bayliss, D., Santerne, A., et al. 2021, *MNRAS*, 504, L45, doi: [10.1093/mnras/504/1/45](https://doi.org/10.1093/mnras/504/1/45)
- Buchhave, L. A., Dressing, C. D., Dumusque, X., et al. 2016, *AJ*, 152, 160, doi: [10.3847/0004-6256/152/6/160](https://doi.org/10.3847/0004-6256/152/6/160)
- Butler, C. J., Byrne, P. B., Andrews, A. D., & Doyle, J. G. 1981, *MNRAS*, 197, 815, doi: [10.1093/mnras/197.3.815](https://doi.org/10.1093/mnras/197.3.815)
- Cale, B., Plavchan, P., LeBrun, D., et al. 2019, *AJ*, 158, 170, doi: [10.3847/1538-3881/ab3b0f](https://doi.org/10.3847/1538-3881/ab3b0f)
- Cale, B., Reefe, M., Plavchan, P., et al. 2021, arXiv e-prints, arXiv:2109.13996, <https://arxiv.org/abs/2109.13996>
- Chambers, J. E. 1999, *MNRAS*, 304, 793, doi: [10.1046/j.1365-8711.1999.02379.x](https://doi.org/10.1046/j.1365-8711.1999.02379.x)
- Chen, J., & Kipping, D. 2017, *ApJ*, 834, 17, doi: [10.3847/1538-4357/834/1/17](https://doi.org/10.3847/1538-4357/834/1/17)
- Choi, J., Dotter, A., Conroy, C., et al. 2016, *ApJ*, 823, 102, doi: [10.3847/0004-637X/823/2/102](https://doi.org/10.3847/0004-637X/823/2/102)
- Christiansen, J. L., Vanderburg, A., Burt, J., et al. 2017, *AJ*, 154, 122, doi: [10.3847/1538-3881/aa832d](https://doi.org/10.3847/1538-3881/aa832d)
- Claret, A. 2017, *A&A*, 600, A30, doi: [10.1051/0004-6361/201629705](https://doi.org/10.1051/0004-6361/201629705)
- Claret, A., & Bloemen, S. 2011, *A&A*, 529, A75, doi: [10.1051/0004-6361/201116451](https://doi.org/10.1051/0004-6361/201116451)
- Claret, A., Hauschildt, P. H., & Witte, S. 2012, *A&A*, 546, A14, doi: [10.1051/0004-6361/201219849](https://doi.org/10.1051/0004-6361/201219849)
- Cochran, W. D., Hatzes, A. P., Butler, R. P., & Marcy, G. W. 1997, *ApJ*, 483, 457, doi: [10.1086/304245](https://doi.org/10.1086/304245)
- Collins, K. A., Kielkopf, J. F., Stassun, K. G., & Hessman, F. V. 2017, *AJ*, 153, 77, doi: [10.3847/1538-3881/153/2/77](https://doi.org/10.3847/1538-3881/153/2/77)
- Cully, S. L., Siegmund, O. H. W., Vedder, P. W., & Vallergera, J. V. 1993, *ApJL*, 414, L49, doi: [10.1086/186993](https://doi.org/10.1086/186993)
- Cumming, A., Marcy, G. W., & Butler, R. P. 1999, *ApJ*, 526, 890, doi: [10.1086/308020](https://doi.org/10.1086/308020)
- Cutri, R. M., Skrutskie, M. F., van Dyk, S., et al. 2003, *VizieR Online Data Catalog*, II/246
- Czesla, S., Huber, K. F., Wolter, U., Schröter, S., & Schmitt, J. H. M. M. 2009, *A&A*, 505, 1277, doi: [10.1051/0004-6361/200912454](https://doi.org/10.1051/0004-6361/200912454)
- Czesla, S., Schröter, S., Schneider, C. P., et al. 2019, *PyA: Python astronomy-related packages*. <http://ascl.net/1906.010>
- Dalal, S., Kiefer, F., Hébrard, G., et al. 2021, *A&A*, 651, A11, doi: [10.1051/0004-6361/202140712](https://doi.org/10.1051/0004-6361/202140712)
- Davenport, J. R. A., Hawley, S. L., Hebb, L., et al. 2014, *ApJ*, 797, 122, doi: [10.1088/0004-637X/797/2/122](https://doi.org/10.1088/0004-637X/797/2/122)
- David, T. J., Petigura, E. A., Luger, R., et al. 2019, *ApJL*, 885, L12, doi: [10.3847/2041-8213/ab4c99](https://doi.org/10.3847/2041-8213/ab4c99)
- David, T. J., Hillenbrand, L. A., Petigura, E. A., et al. 2016, *Nature*, 534, 658, doi: [10.1038/nature18293](https://doi.org/10.1038/nature18293)
- Dawson, R. I., Huang, C. X., Brahm, R., et al. 2021, *AJ*, 161, 161, doi: [10.3847/1538-3881/abd8d0](https://doi.org/10.3847/1538-3881/abd8d0)
- Daylan, T., Pínglé, K., Wright, J., et al. 2021, *AJ*, 161, 85, doi: [10.3847/1538-3881/abd73e](https://doi.org/10.3847/1538-3881/abd73e)
- Deming, D., & Knutson, H. A. 2020, *Nature Astronomy*, 4, 453, doi: [10.1038/s41550-020-1100-9](https://doi.org/10.1038/s41550-020-1100-9)
- Demory, B.-O., Gillon, M., Madhusudhan, N., & Queloz, D. 2016a, *MNRAS*, 455, 2018, doi: [10.1093/mnras/stv2239](https://doi.org/10.1093/mnras/stv2239)
- Demory, B.-O., Gillon, M., de Wit, J., et al. 2016b, *Nature*, 532, 207, doi: [10.1038/nature17169](https://doi.org/10.1038/nature17169)

- Demory, B. O., Pozuelos, F. J., Gómez Maqueo Chew, Y., et al. 2020, *A&A*, 642, A49, doi: [10.1051/0004-6361/202038616](https://doi.org/10.1051/0004-6361/202038616)
- Désert, J.-M., Charbonneau, D., Demory, B.-O., et al. 2011, *ApJS*, 197, 14, doi: [10.1088/0067-0049/197/1/14](https://doi.org/10.1088/0067-0049/197/1/14)
- Donati, J. F., Semel, M., Carter, B. D., Rees, D. E., & Collier Cameron, A. 1997, *MNRAS*, 291, 658, doi: [10.1093/mnras/291.4.658](https://doi.org/10.1093/mnras/291.4.658)
- Donati, J. F., Kouach, D., Moutou, C., et al. 2020, *MNRAS*, 498, 5684, doi: [10.1093/mnras/staa2569](https://doi.org/10.1093/mnras/staa2569)
- Dotter, A. 2016, *ApJS*, 222, 8, doi: [10.3847/0067-0049/222/1/8](https://doi.org/10.3847/0067-0049/222/1/8)
- Ducrot, E., Sestovic, M., Morris, B. M., et al. 2018, *AJ*, 156, 218, doi: [10.3847/1538-3881/aade94](https://doi.org/10.3847/1538-3881/aade94)
- Ducrot, E., Gillon, M., Delrez, L., et al. 2020, *A&A*, 640, A112, doi: [10.1051/0004-6361/201937392](https://doi.org/10.1051/0004-6361/201937392)
- Eastman, J., Siverd, R., & Gaudi, B. S. 2010, *PASP*, 122, 935, doi: [10.1086/655938](https://doi.org/10.1086/655938)
- Eastman, J. D., Rodriguez, J. E., Agol, E., et al. 2019, arXiv e-prints, arXiv:1907.09480. <https://arxiv.org/abs/1907.09480>
- Fabrycky, D. C. 2010, arXiv e-prints, arXiv:1006.3834. <https://arxiv.org/abs/1006.3834>
- Fajardo-Acosta, S. B., Beichman, C. A., & Cutri, R. M. 2000, *ApJL*, 538, L155, doi: [10.1086/312815](https://doi.org/10.1086/312815)
- Fazio, G. G., Hora, J. L., Allen, L. E., et al. 2004, *ApJS*, 154, 10, doi: [10.1086/422843](https://doi.org/10.1086/422843)
- Foreman-Mackey, D. 2018, *Research Notes of the American Astronomical Society*, 2, 31, doi: [10.3847/2515-5172/aaaf6c](https://doi.org/10.3847/2515-5172/aaaf6c)
- Foreman-Mackey, D., Agol, E., Ambikasaran, S., & Angus, R. 2017, *AJ*, 154, 220, doi: [10.3847/1538-3881/aa9332](https://doi.org/10.3847/1538-3881/aa9332)
- Foreman-Mackey, D., Hogg, D. W., Lang, D., & Goodman, J. 2013, *PASP*, 125, 306, doi: [10.1086/670067](https://doi.org/10.1086/670067)
- Foreman-Mackey, D., Luger, R., Agol, E., et al. 2021, *The Journal of Open Source Software*, 6, 3285, doi: [10.21105/joss.03285](https://doi.org/10.21105/joss.03285)
- Gaia Collaboration. 2018, *VizieR Online Data Catalog*, I/345
- Gelman, A., & Rubin, D. B. 1992, *Statistical Science*, 7, 457, doi: [10.1214/ss/1177011136](https://doi.org/10.1214/ss/1177011136)
- Gilbert, E. A., Barclay, T., Schlieder, J. E., et al. 2020, *AJ*, 160, 116, doi: [10.3847/1538-3881/aba4b2](https://doi.org/10.3847/1538-3881/aba4b2)
- Gilbert, E. A., Barclay, T., Quintana, E. V., et al. 2021, arXiv e-prints, arXiv:2109.03924. <https://arxiv.org/abs/2109.03924>
- Gillon, M., Demory, B. O., Benneke, B., et al. 2012, *A&A*, 539, A28, doi: [10.1051/0004-6361/201118309](https://doi.org/10.1051/0004-6361/201118309)
- Gillon, M., Jehin, E., Lederer, S. M., et al. 2016, *Nature*, 533, 221, doi: [10.1038/nature17448](https://doi.org/10.1038/nature17448)
- Gillon, M., Triaud, A. H. M. J., Demory, B.-O., et al. 2017a, *Nature*, 542, 456, doi: [10.1038/nature21360](https://doi.org/10.1038/nature21360)
- Gillon, M., Demory, B.-O., Van Grootel, V., et al. 2017b, *Nature Astronomy*, 1, 0056, doi: [10.1038/s41550-017-0056](https://doi.org/10.1038/s41550-017-0056)
- Grillmair, C. J., Charbonneau, D., Burrows, A., et al. 2007, *ApJL*, 658, L115, doi: [10.1086/513741](https://doi.org/10.1086/513741)
- Grimm, S. L., Demory, B.-O., Gillon, M., et al. 2018, *A&A*, 613, A68, doi: [10.1051/0004-6361/201732233](https://doi.org/10.1051/0004-6361/201732233)
- Hadden, S., & Lithwick, Y. 2014, *ApJ*, 787, 80, doi: [10.1088/0004-637X/787/1/80](https://doi.org/10.1088/0004-637X/787/1/80)
- Haffert, S. Y., Bohn, A. J., de Boer, J., et al. 2019, *Nature Astronomy*, 3, 749, doi: [10.1038/s41550-019-0780-5](https://doi.org/10.1038/s41550-019-0780-5)
- Harris, C. R., Millman, K. J., van der Walt, S. J., et al. 2020, *Nature*, 585, 357, doi: [10.1038/s41586-020-2649-2](https://doi.org/10.1038/s41586-020-2649-2)
- Hebb, L., Petro, L., Ford, H. C., et al. 2007, *MNRAS*, 379, 63, doi: [10.1111/j.1365-2966.2007.11904.x](https://doi.org/10.1111/j.1365-2966.2007.11904.x)
- Henry, G. W., Marcy, G. W., Butler, R. P., & Vogt, S. S. 2000, *ApJL*, 529, L41, doi: [10.1086/312458](https://doi.org/10.1086/312458)
- Holman, M. J., & Murray, N. W. 2005, *Science*, 307, 1288, doi: [10.1126/science.1107822](https://doi.org/10.1126/science.1107822)
- Holt, J. R. 1893, *Astronomy and Astro-Physics (formerly The Sidereal Messenger)*, 12, 646
- Howell, S. B., Sobeck, C., Haas, M., et al. 2014, *PASP*, 126, 398, doi: [10.1086/676406](https://doi.org/10.1086/676406)
- Hunter, J. D. 2007, *Computing in Science and Engineering*, 9, 90, doi: [10.1109/MCSE.2007.55](https://doi.org/10.1109/MCSE.2007.55)

- Ingalls, J. G., Krick, J. E., Carey, S. J., et al. 2012, in Society of Photo-Optical Instrumentation Engineers (SPIE) Conference Series, Vol. 8442, Space Telescopes and Instrumentation 2012: Optical, Infrared, and Millimeter Wave, ed. M. C. Clampin, G. G. Fazio, H. A. MacEwen, & J. Oschmann, Jacobus M., 84421Y, doi: [10.1117/12.926947](https://doi.org/10.1117/12.926947)
- Ingalls, J. G., Krick, J. E., Carey, S. J., et al. 2018, in Society of Photo-Optical Instrumentation Engineers (SPIE) Conference Series, Vol. 10698, Space Telescopes and Instrumentation 2018: Optical, Infrared, and Millimeter Wave, ed. M. Lystrup, H. A. MacEwen, G. G. Fazio, N. Batalha, N. Siegler, & E. C. Tong, 106985E, doi: [10.1117/12.2313640](https://doi.org/10.1117/12.2313640)
- Ingalls, J. G., Krick, J. E., Carey, S. J., et al. 2016, *AJ*, 152, 44, doi: [10.3847/0004-6256/152/2/44](https://doi.org/10.3847/0004-6256/152/2/44)
- Jenkins, J. M., Twicken, J. D., McCauliff, S., et al. 2016, in Society of Photo-Optical Instrumentation Engineers (SPIE) Conference Series, Vol. 9913, Software and Cyberinfrastructure for Astronomy IV, ed. G. Chiozzi & J. C. Guzman, 99133E, doi: [10.1117/12.2233418](https://doi.org/10.1117/12.2233418)
- Jensen, E. 2013, Tapir: A web interface for transit/eclipse observability. <http://ascl.net/1306.007>
- Kalas, P., Liu, M. C., & Matthews, B. C. 2004, *Science*, 303, 1990, doi: [10.1126/science.1093420](https://doi.org/10.1126/science.1093420)
- Keppler, M., Benisty, M., Müller, A., et al. 2018, *A&A*, 617, A44, doi: [10.1051/0004-6361/201832957](https://doi.org/10.1051/0004-6361/201832957)
- Klein, B., Donati, J.-F., Moutou, C., et al. 2021, *MNRAS*, 502, 188, doi: [10.1093/mnras/staa3702](https://doi.org/10.1093/mnras/staa3702)
- Kostov, V. B., Orosz, J. A., Feinstein, A. D., et al. 2020, *AJ*, 159, 253, doi: [10.3847/1538-3881/ab8a48](https://doi.org/10.3847/1538-3881/ab8a48)
- Kreidberg, L. 2015, *PASP*, 127, 1161, doi: [10.1086/683602](https://doi.org/10.1086/683602)
- Kundu, M. R., Jackson, P. D., White, S. M., & Melozzi, M. 1987, *ApJ*, 312, 822, doi: [10.1086/164928](https://doi.org/10.1086/164928)
- Lagrange, A. M., Gratadour, D., Chauvin, G., et al. 2009, *A&A*, 493, L21, doi: [10.1051/0004-6361:200811325](https://doi.org/10.1051/0004-6361:200811325)
- Lagrange, A. M., Meunier, N., Rubini, P., et al. 2019, *Nature Astronomy*, 3, 1135, doi: [10.1038/s41550-019-0857-1](https://doi.org/10.1038/s41550-019-0857-1)
- Lam, K. W. F., Korth, J., Masuda, K., et al. 2020, *AJ*, 159, 120, doi: [10.3847/1538-3881/ab66c9](https://doi.org/10.3847/1538-3881/ab66c9)
- Lannier, J., Lagrange, A. M., Bonavita, M., et al. 2017, *A&A*, 603, A54, doi: [10.1051/0004-6361/201628677](https://doi.org/10.1051/0004-6361/201628677)
- Lanotte, A. A., Gillon, M., Demory, B. O., et al. 2014, *A&A*, 572, A73, doi: [10.1051/0004-6361/201424373](https://doi.org/10.1051/0004-6361/201424373)
- Laskar, J. 1997, *A&A*, 317, L75
- . 2000, *PhRvL*, 84, 3240, doi: [10.1103/PhysRevLett.84.3240](https://doi.org/10.1103/PhysRevLett.84.3240)
- Laskar, J., & Petit, A. C. 2017, *A&A*, 605, A72, doi: [10.1051/0004-6361/201630022](https://doi.org/10.1051/0004-6361/201630022)
- Leleu, A., Alibert, Y., Hara, N. C., et al. 2021, *A&A*, 649, A26, doi: [10.1051/0004-6361/202039767](https://doi.org/10.1051/0004-6361/202039767)
- Lewis, N. K., Knutson, H. A., Showman, A. P., et al. 2013, *ApJ*, 766, 95, doi: [10.1088/0004-637X/766/2/95](https://doi.org/10.1088/0004-637X/766/2/95)
- Lightkurve Collaboration, Cardoso, J. V. d. M., Hedges, C., et al. 2018, Lightkurve: Kepler and TESS time series analysis in Python. <http://ascl.net/1812.013>
- Lithwick, Y., Xie, J., & Wu, Y. 2012, *ApJ*, 761, 122, doi: [10.1088/0004-637X/761/2/122](https://doi.org/10.1088/0004-637X/761/2/122)
- Liu, M. C., Matthews, B. C., Williams, J. P., & Kalas, P. G. 2004, *ApJ*, 608, 526, doi: [10.1086/392531](https://doi.org/10.1086/392531)
- Mahtani, D. P., Maxted, P. F. L., Anderson, D. R., et al. 2013, *MNRAS*, 432, 693, doi: [10.1093/mnras/stt505](https://doi.org/10.1093/mnras/stt505)
- Mamajek, E. E., & Bell, C. P. M. 2014, *MNRAS*, 445, 2169, doi: [10.1093/mnras/stu1894](https://doi.org/10.1093/mnras/stu1894)
- Mandel, K., & Agol, E. 2002, *ApJL*, 580, L171, doi: [10.1086/345520](https://doi.org/10.1086/345520)
- Mann, A. W., Gaidos, E., Mace, G. N., et al. 2016, *ApJ*, 818, 46, doi: [10.3847/0004-637X/818/1/46](https://doi.org/10.3847/0004-637X/818/1/46)
- Mannaday, V. K., Thakur, P., Jiang, I.-G., et al. 2020, *AJ*, 160, 47, doi: [10.3847/1538-3881/ab9818](https://doi.org/10.3847/1538-3881/ab9818)
- Marois, C., Macintosh, B., Barman, T., et al. 2008, *Science*, 322, 1348, doi: [10.1126/science.1166585](https://doi.org/10.1126/science.1166585)
- Marois, C., Zuckerman, B., Konopacky, Q. M., Macintosh, B., & Barman, T. 2010, *Nature*, 468, 1080, doi: [10.1038/nature09684](https://doi.org/10.1038/nature09684)
- Martioli, E. 2020, private communication

- Martioli, E., Hébrard, G., Correia, A. C. M., Laskar, J., & Lecavelier des Etangs, A. 2021, *A&A*, 649, A177, doi: [10.1051/0004-6361/202040235](https://doi.org/10.1051/0004-6361/202040235)
- Martioli, E., Hébrard, G., Moutou, C., et al. 2020, *A&A*, 641, L1, doi: [10.1051/0004-6361/202038695](https://doi.org/10.1051/0004-6361/202038695)
- Mayor, M., & Queloz, D. 1995, *Nature*, 378, 355, doi: [10.1038/378355a0](https://doi.org/10.1038/378355a0)
- Mazeh, T., Nachmani, G., Holczer, T., et al. 2013, *ApJS*, 208, 16, doi: [10.1088/0067-0049/208/2/16](https://doi.org/10.1088/0067-0049/208/2/16)
- McLaughlin, D. B. 1924, *ApJ*, 60, 22, doi: [10.1086/142826](https://doi.org/10.1086/142826)
- Mendonça, J. M., Malik, M., Demory, B.-O., & Heng, K. 2018, *AJ*, 155, 150, doi: [10.3847/1538-3881/aaaebc](https://doi.org/10.3847/1538-3881/aaaebc)
- Morin, J., Donati, J. F., Petit, P., et al. 2010, *MNRAS*, 407, 2269, doi: [10.1111/j.1365-2966.2010.17101.x](https://doi.org/10.1111/j.1365-2966.2010.17101.x)
- Morris, B. 2020, *The Journal of Open Source Software*, 5, 2103, doi: [10.21105/joss.02103](https://doi.org/10.21105/joss.02103)
- Morris, B. M., Agol, E., Hebb, L., et al. 2018, *ApJL*, 863, L32, doi: [10.3847/2041-8213/aad8aa](https://doi.org/10.3847/2041-8213/aad8aa)
- Moutou, C., Dalal, S., Donati, J. F., et al. 2020, *A&A*, 642, A72, doi: [10.1051/0004-6361/202038108](https://doi.org/10.1051/0004-6361/202038108)
- Newton, E. R., Mann, A. W., Tofflemire, B. M., et al. 2019, *ApJL*, 880, L17, doi: [10.3847/2041-8213/ab2988](https://doi.org/10.3847/2041-8213/ab2988)
- Ohta, Y., Taruya, A., & Suto, Y. 2005, *ApJ*, 622, 1118, doi: [10.1086/428344](https://doi.org/10.1086/428344)
- Osborn, A., Armstrong, D. J., Cale, B., et al. 2021, *MNRAS*, 507, 2782, doi: [10.1093/mnras/stab2313](https://doi.org/10.1093/mnras/stab2313)
- Oshagh, M., Boué, G., Haghighipour, N., et al. 2012, *A&A*, 540, A62, doi: [10.1051/0004-6361/201118102](https://doi.org/10.1051/0004-6361/201118102)
- Oshagh, M., Santos, N. C., Boisse, I., et al. 2013, *A&A*, 556, A19, doi: [10.1051/0004-6361/201321309](https://doi.org/10.1051/0004-6361/201321309)
- Pallé, E. 2020, private communication
- Palle, E., Oshagh, M., Casasayas-Barris, N., et al. 2020, *A&A*, 643, A25, doi: [10.1051/0004-6361/202038583](https://doi.org/10.1051/0004-6361/202038583)
- Pepe, F., Cristiani, S., Rebolo, R., et al. 2021, *A&A*, 645, A96, doi: [10.1051/0004-6361/202038306](https://doi.org/10.1051/0004-6361/202038306)
- Pérez, F., & Granger, B. E. 2007, *Computing in Science and Engineering*, 9, 21, doi: [10.1109/MCSE.2007.53](https://doi.org/10.1109/MCSE.2007.53)
- Pitkin, M., Williams, D., Fletcher, L., & Grant, S. D. T. 2014, *MNRAS*, 445, 2268, doi: [10.1093/mnras/stu1889](https://doi.org/10.1093/mnras/stu1889)
- Plavchan, P., Jura, M., & Lipsky, S. J. 2005, *ApJ*, 631, 1161, doi: [10.1086/432568](https://doi.org/10.1086/432568)
- Plavchan, P., Werner, M. W., Chen, C. H., et al. 2009, *ApJ*, 698, 1068, doi: [10.1088/0004-637X/698/2/1068](https://doi.org/10.1088/0004-637X/698/2/1068)
- Plavchan, P., Barclay, T., Gagné, J., et al. 2020, *Nature*, 582, 497, doi: [10.1038/s41586-020-2400-z](https://doi.org/10.1038/s41586-020-2400-z)
- Pont, F., Gilliland, R. L., Moutou, C., et al. 2007, *A&A*, 476, 1347, doi: [10.1051/0004-6361:20078269](https://doi.org/10.1051/0004-6361:20078269)
- Rainer, M., Borsa, F., Pino, L., et al. 2021, *A&A*, 649, A29, doi: [10.1051/0004-6361/202039247](https://doi.org/10.1051/0004-6361/202039247)
- Rayner, J., Tokunaga, A., Jaffe, D., et al. 2016, in *Society of Photo-Optical Instrumentation Engineers (SPIE) Conference Series*, Vol. 9908, *Ground-based and Airborne Instrumentation for Astronomy VI*, ed. C. J. Evans, L. Simard, & H. Takami, 990884, doi: [10.1117/12.2232064](https://doi.org/10.1117/12.2232064)
- Rein, H., & Liu, S. F. 2012, *A&A*, 537, A128, doi: [10.1051/0004-6361/201118085](https://doi.org/10.1051/0004-6361/201118085)
- Rein, H., & Spiegel, D. S. 2015, *MNRAS*, 446, 1424, doi: [10.1093/mnras/stu2164](https://doi.org/10.1093/mnras/stu2164)
- Ricker, G. R., Winn, J. N., Vanderspek, R., et al. 2015, *Journal of Astronomical Telescopes, Instruments, and Systems*, 1, 014003, doi: [10.1117/1.JATIS.1.1.014003](https://doi.org/10.1117/1.JATIS.1.1.014003)
- Rodriguez, J. E., Quinn, S. N., Zhou, G., et al. 2021, *AJ*, 161, 194, doi: [10.3847/1538-3881/abe38a](https://doi.org/10.3847/1538-3881/abe38a)
- Rosenthal, L. J., Fulton, B. J., Hirsch, L. A., et al. 2021, *ApJS*, 255, 8, doi: [10.3847/1538-4365/abe23c](https://doi.org/10.3847/1538-4365/abe23c)
- Rossiter, R. A. 1924, *ApJ*, 60, 15, doi: [10.1086/142825](https://doi.org/10.1086/142825)
- Sanchis-Ojeda, R., & Winn, J. N. 2011, *ApJ*, 743, 61, doi: [10.1088/0004-637X/743/1/61](https://doi.org/10.1088/0004-637X/743/1/61)
- Sanchis-Ojeda, R., Winn, J. N., Holman, M. J., et al. 2011, *ApJ*, 733, 127, doi: [10.1088/0004-637X/733/2/127](https://doi.org/10.1088/0004-637X/733/2/127)
- Sato, B., Wang, L., Liu, Y.-J., et al. 2016, *ApJ*, 819, 59, doi: [10.3847/0004-637X/819/1/59](https://doi.org/10.3847/0004-637X/819/1/59)

- Smith, J. C., Stumpe, M. C., Van Cleve, J. E., et al. 2012, *PASP*, 124, 1000, doi: [10.1086/667697](https://doi.org/10.1086/667697)
- Song, I., Weinberger, A. J., Becklin, E. E., Zuckerman, B., & Chen, C. 2002, *AJ*, 124, 514, doi: [10.1086/341164](https://doi.org/10.1086/341164)
- Stangret, M., Pallé, E., Casasayas-Barris, N., et al. 2021, arXiv e-prints, arXiv:2104.12414. <https://arxiv.org/abs/2104.12414>
- Stauffer, J., Tanner, A. M., Bryden, G., et al. 2010, *PASP*, 122, 885, doi: [10.1086/655773](https://doi.org/10.1086/655773)
- Stevenson, K. B., Harrington, J., Fortney, J. J., et al. 2012, *ApJ*, 754, 136, doi: [10.1088/0004-637X/754/2/136](https://doi.org/10.1088/0004-637X/754/2/136)
- Stumpe, M. C., Smith, J. C., Catanzarite, J. H., et al. 2014, *PASP*, 126, 100, doi: [10.1086/674989](https://doi.org/10.1086/674989)
- Stumpe, M. C., Smith, J. C., Van Cleve, J. E., et al. 2012, *PASP*, 124, 985, doi: [10.1086/667698](https://doi.org/10.1086/667698)
- Sun, L., Ioannidis, P., Gu, S., et al. 2019, *A&A*, 624, A15, doi: [10.1051/0004-6361/201834275](https://doi.org/10.1051/0004-6361/201834275)
- Szabó, G. M., Gandolfi, D., Brandeker, A., et al. 2021, arXiv e-prints, arXiv:2108.02149. <https://arxiv.org/abs/2108.02149>
- Todorov, K. O., Deming, D., Burrows, A., & Grillmair, C. J. 2014, *ApJ*, 796, 100, doi: [10.1088/0004-637X/796/2/100](https://doi.org/10.1088/0004-637X/796/2/100)
- Triaud, A. H. M. J. 2018, *The Rossiter-McLaughlin Effect in Exoplanet Research* (Springer International Publishing AG), 2, doi: [10.1007/978-3-319-55333-7_2](https://doi.org/10.1007/978-3-319-55333-7_2)
- Triaud, A. H. M. J., Queloz, D., Bouchy, F., et al. 2009, *A&A*, 506, 377, doi: [10.1051/0004-6361/200911897](https://doi.org/10.1051/0004-6361/200911897)
- Trifonov, T. 2019, *The Exo-Striker: Transit and radial velocity interactive fitting tool for orbital analysis and N-body simulations*. <http://ascl.net/1906.004>
- Tsikoudi, V., & Kellett, B. J. 2000, *MNRAS*, 319, 1147, doi: [10.1046/j.1365-8711.2000.03905.x](https://doi.org/10.1046/j.1365-8711.2000.03905.x)
- Virtanen, P., Gommers, R., Oliphant, T. E., et al. 2020, *Nature Methods*, 17, 261, doi: [10.1038/s41592-019-0686-2](https://doi.org/10.1038/s41592-019-0686-2)
- Wang, S., Winn, J. N., Addison, B. C., et al. 2021, *AJ*, 162, 50, doi: [10.3847/1538-3881/ac0626](https://doi.org/10.3847/1538-3881/ac0626)
- Werner, M. W., Roellig, T. L., Low, F. J., et al. 2004, *ApJS*, 154, 1, doi: [10.1086/422992](https://doi.org/10.1086/422992)
- White, R., Schaefer, G., Boyajian, T., et al. 2019, in *American Astronomical Society Meeting Abstracts*, Vol. 233, American Astronomical Society Meeting Abstracts #233, 259.41
- Winn, J. N. 2007, in *Astronomical Society of the Pacific Conference Series*, Vol. 366, *Transiting Extrapolar Planets Workshop*, ed. C. Afonso, D. Wel Drake, & T. Henning, 170. <https://arxiv.org/abs/astro-ph/0612744>
- Zacharias, N., Finch, C. T., Girard, T. M., et al. 2012, *VizieR Online Data Catalog*, I/322A
- Zechmeister, M., Reiners, A., Amado, P. J., et al. 2018, *A&A*, 609, A12, doi: [10.1051/0004-6361/201731483](https://doi.org/10.1051/0004-6361/201731483)
- Zellem, R. T., Lewis, N. K., Knutson, H. A., et al. 2014, *ApJ*, 790, 53, doi: [10.1088/0004-637X/790/1/53](https://doi.org/10.1088/0004-637X/790/1/53)
- Zhang, Z., Zhou, Y., Rackham, B. V., & Apai, D. 2018, *AJ*, 156, 178, doi: [10.3847/1538-3881/aade4f](https://doi.org/10.3847/1538-3881/aade4f)
- Zuckerman, B. 2001, *ARA&A*, 39, 549, doi: [10.1146/annurev.astro.39.1.549](https://doi.org/10.1146/annurev.astro.39.1.549)

APPENDIX

A. CORNER PLOTS FROM MAIN EXOSTRIKER ANALYSIS

This section highlights the corner plots that were generated by Exo-Striker. All Exo-Striker corner plots are included here.

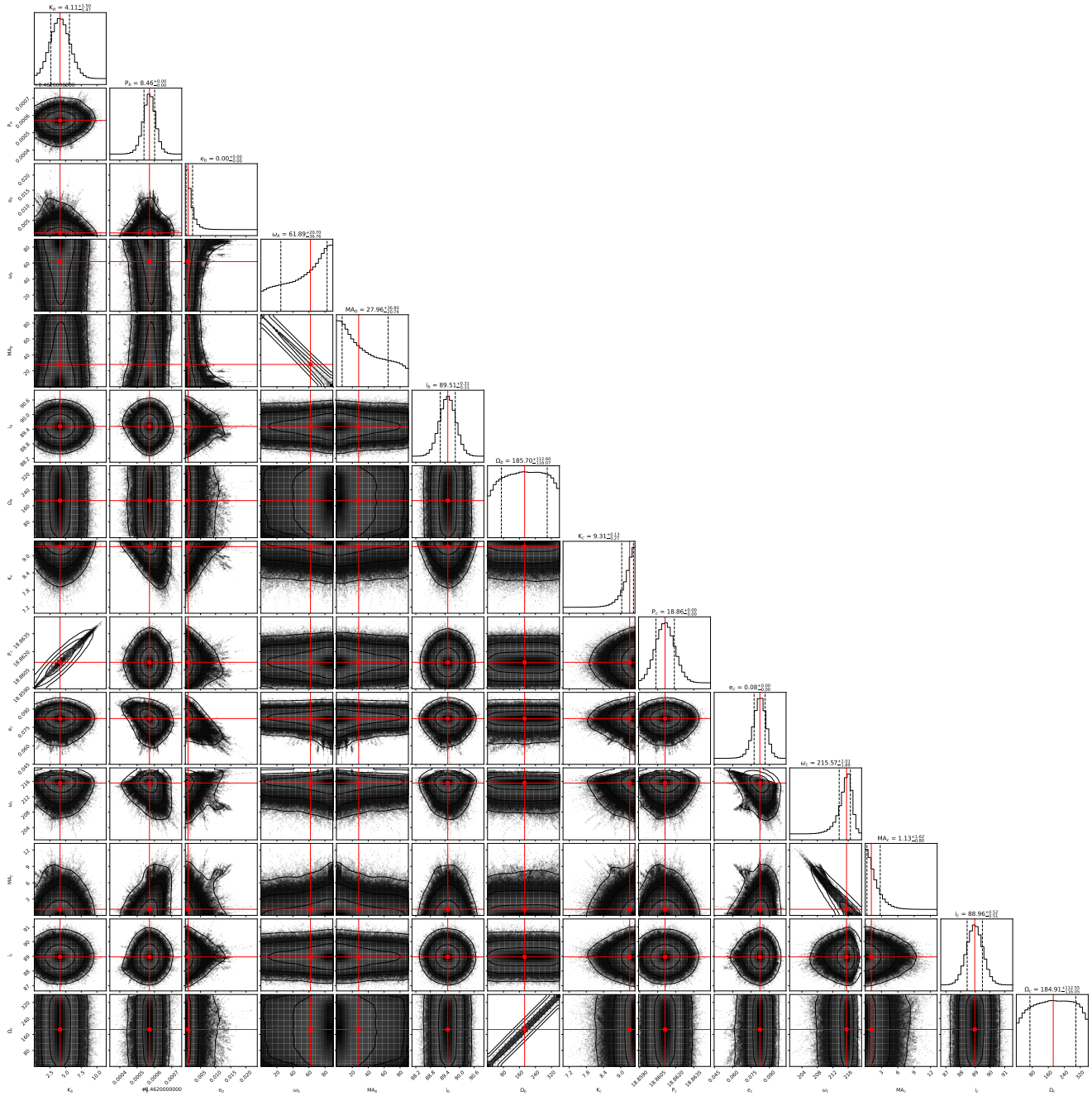


Figure A1. Exo-Striker-generated MCMC corner plot for AU Mic 2-planet case. All TTVs are incorporated into this model.

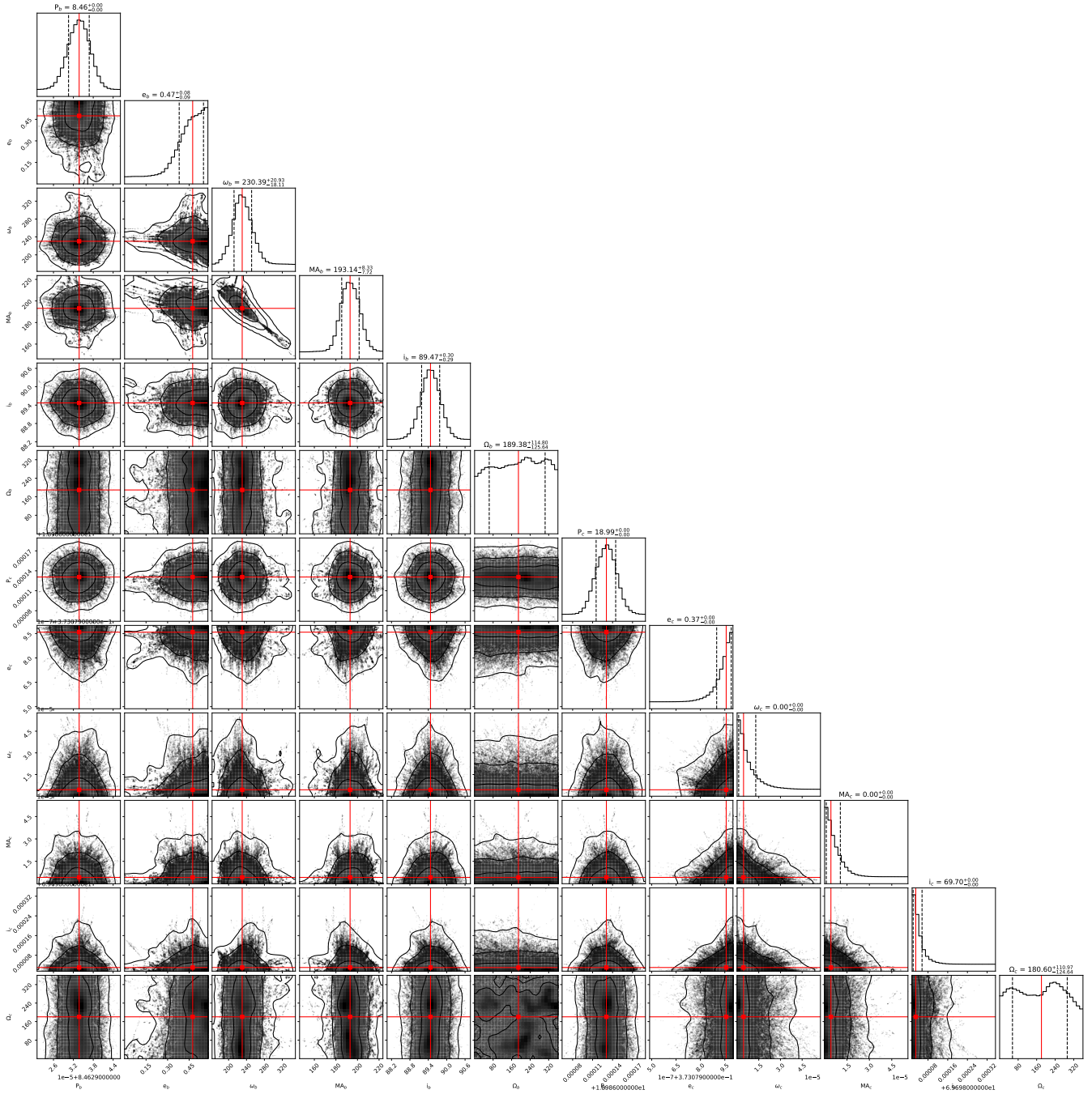


Figure A2. Exo-Striker-generated MCMC corner plot for AU Mic mass-less planets case. All TTVs are incorporated into this model.

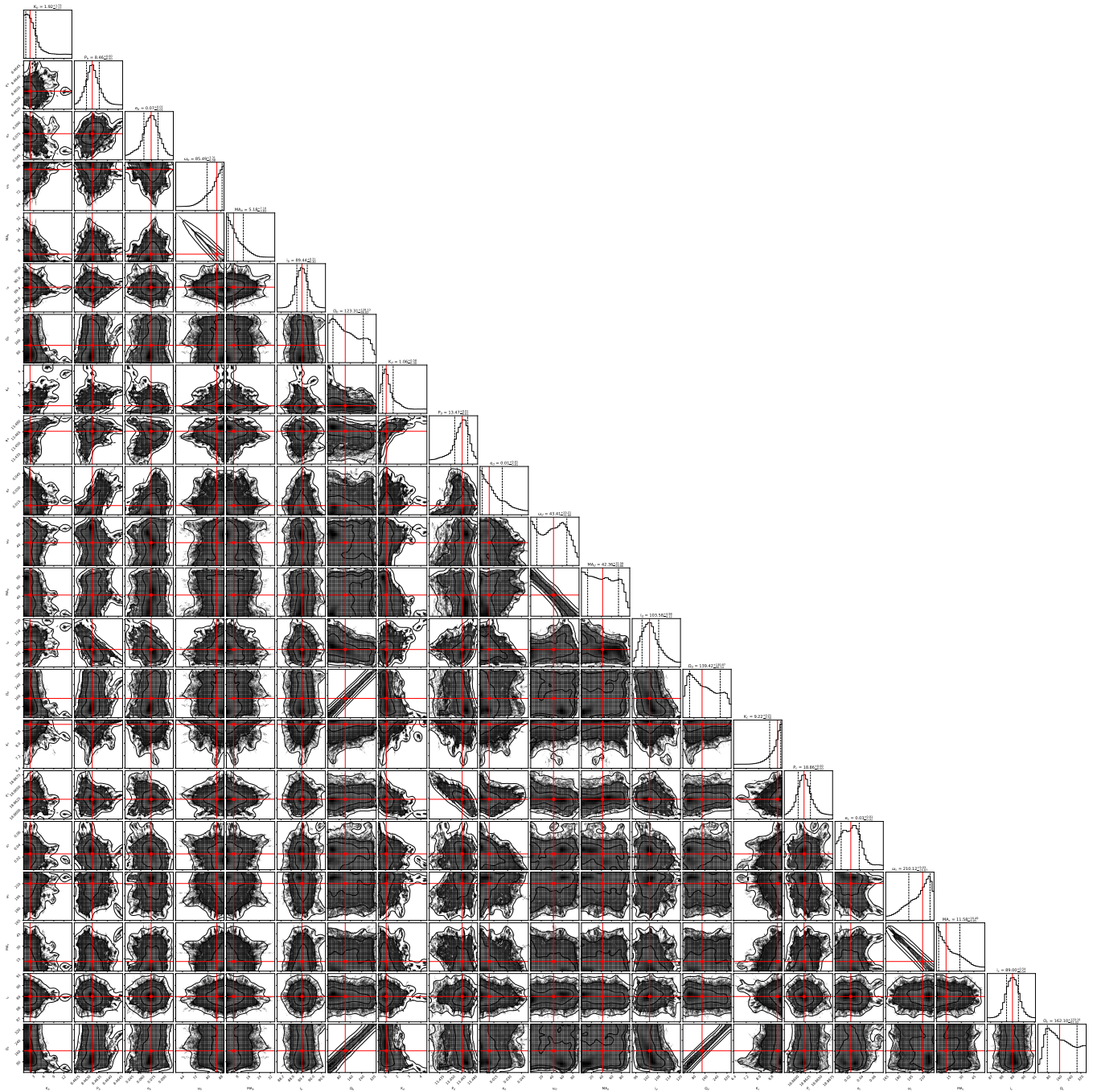


Figure A3. Exo-Striker-generated MCMC corner plot for AU Mic 3-planet case. All TTVs are incorporated into this model.

B. CORNER PLOTS FROM PHOTODYNAMICAL ANALYSIS

This section highlights the corner plots that were generated by photodynamical analysis. The corner plots for both models a and b are included here.

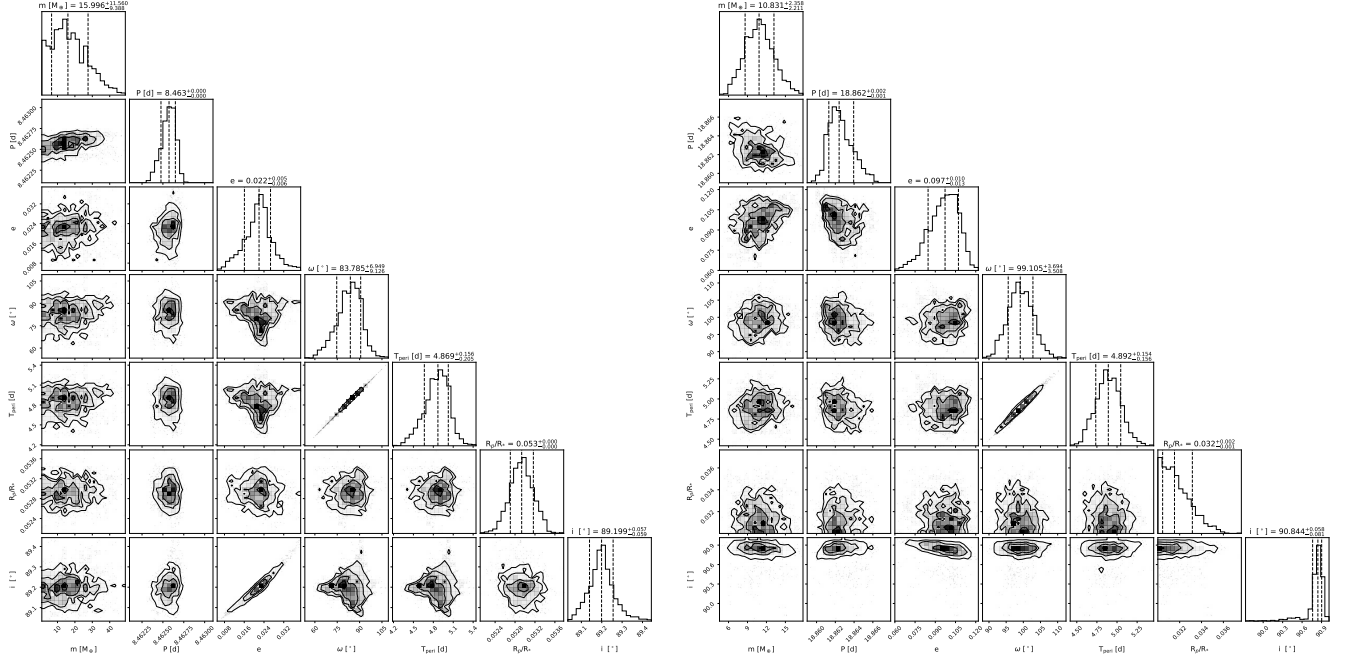


Figure B1. Corner plot for posterior distributions of orbital parameters from the photodynamical model a for AU Mic b (left) and AU Mic c (right).

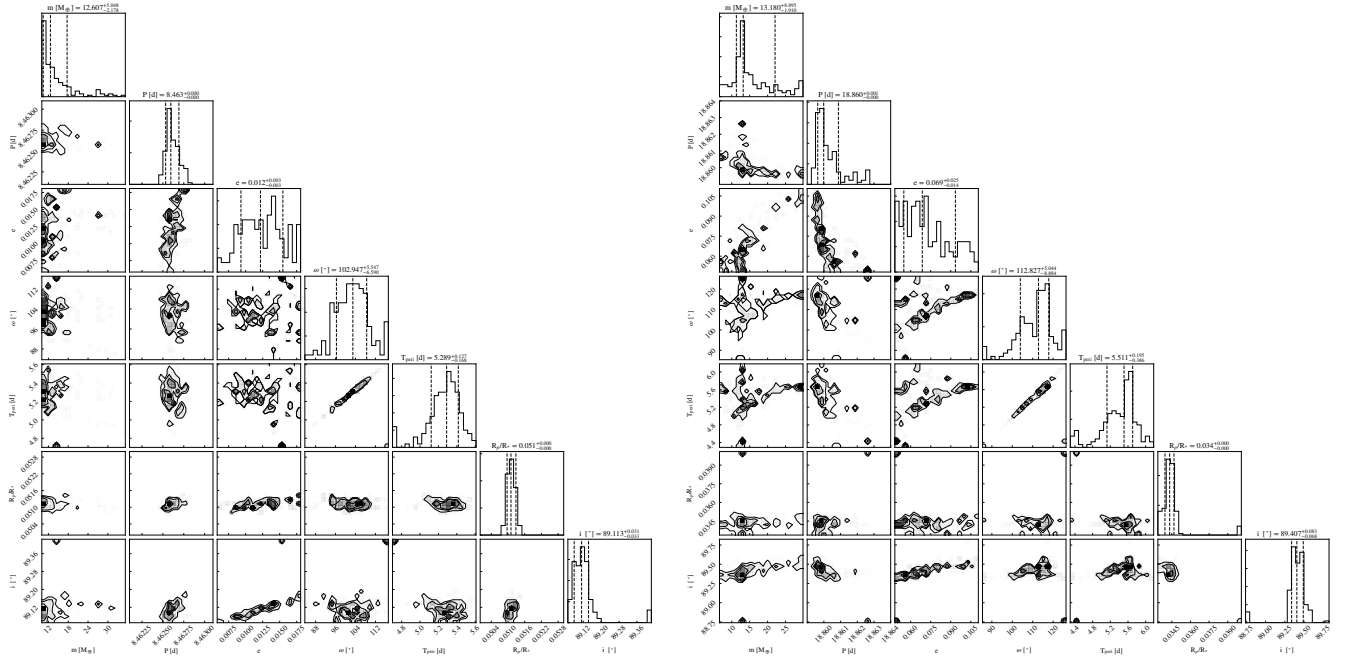


Figure B2. Corner plot for posterior distributions of orbital parameters from the photodynamical model b for AU Mic b (left) and AU Mic c (right).